DYNAMICAL MEAN FIELD MODELLING AND ESTIMATION OF NEURONAL OSCILLATIONS

Marco Filipe Pinto Leite

Department of Clinical and Experimental Epilepsy

Institute of Neurology

University College London

This dissertation is submitted for the degree of Doctor of Philosophy

March 2017

Para os meus avós

ACKNOWLEDGEMENTS

I would like to thank the *Fundação para a Ciência e Tecnologia* who have financially supported the work for this PhD thesis through the grant SFRH/BD/79501/2011.

I would like to thank all the time, dedication and friendship I received from my supervisors Louis and Patricia, and also Karl, throughout all the period of my PhD studies.

I would like to thank Dimitri Kullmann for the support in the latter stages of this work regarding data, ideas and funds.

I would also like to acknowledge Fernando Lopes da Silva, Will Penny, Biswa Sengupta and Elizabeth Nicholson for providing valuable ideas relevant to the works presented here.

Finally I thank all the family and friends that accompanied me through this journey and certainly will continue do so in the future.

DECLARATION

This dissertation is the result of my own work and includes nothing, which is the outcome of work done in collaboration except where specifically indicated in the text. It has not been previously submitted, in part or whole, to any university of institution for any degree, diploma, or other qualification.

Signed:_____

Date:_____

Marco Filipe Pinto Leite, MSc

London

ABSTRACT

Oscillations in neural activity are a ubiquitous phenomenon in the brain. They span multiple timescales and correlate with a myriad of physiological and pathological conditions. Given their intrinsic dynamical nature, mathematical and computational modelling tools have proven to be indispensible in order to interpret and formalize the mechanisms through which these oscillations arise. In this Thesis, I developed a new methodological framework that allows the assimilation of experimental data into biophysically plausible models of neural oscillations.

Motivated by the fast oscillatory activity (30 ~ 130 Hz) at the onset of focal epileptic seizures, I started by investigating, via means of bifurcation analyses, whether such fast oscillations can be plausibly described by conductance-based neural mass models. Neural mass models have enjoyed success in describing several forms of epileptiform activity (e.g. spike-and-wave seizures and interictal spikes), but I found that, in order to generate such fast oscillations, the parameters of this family of models would have to depart significantly from biophysical plausibility. These results motivated the exploration of full mean-field models of spiking neurons to characterise this type of dynamics.

I hence proposed a variant of a mean-field neural population model based on the Fokker-Planck equation of conductance-based, stochastic, leaky integrate-and-fire neurons. This modelling approach was chosen for its capacity to describe arbitrary network configurations and predict firing rates, trans-membrane currents and local field potentials. I introduced a new numerical scheme that makes the computational cost of integrating the ensuing partial differential equations scale linearly with the number of nodes of the networks. These advances are crucial for the practical implementation of model inversion schemes.

I then built upon the literature of Dynamic Causal Modelling to develop a Bayesian model inversion algorithm applicable to dynamical systems in limit cycle regimes. I applied the scheme to the mean-field models described above, using experimental data recordings of carbachol-induced gamma oscillations, in the CA1 region of mice hippocampal slice preparations. The estimated model was able to make accurate

predictions about independent data features; namely inter-spike-interval distributions. Also, the inverted models were qualitatively compatible with the observation that excitatory pyramidal cells and inhibitory interneurons play equally important roles in the dynamics of these oscillations (as opposed to interneuron-dominated gamma oscillations). I also explored the applicability of this inversion scheme to neural mass models of electroencephalographically recorded spike-and-wave seizures in humans.

In conclusion, the work presented in this thesis provides significant new contributions to model based analyses of neuronal oscillatory data, and helps to bridge single-neuron measurements to network-level interactions.

CONTENTS

LIST OF TABLES

LIST OF FIGURES

List of Abbreviations and Acronyms

AMPA	α-amino-3-hydroxy-5-methyl-4-isoxazolepropionic acid
DCM	Dynamic Causal Modelling
EEG	Electroencephalography
ERP	Event Related Potential
FixPt	Fixed-point
fMRI	Functional Magnetic Resonance
FP	Fokker-Planck
GABA	γ-Aminobutyric acid
JR	Jansen and Rit
KL	Kullback-Leibler
LC	Limit Cycle
LFP	Local Field Potential
LIF	Leaky Integrate-and-Fire
MCMC	Markov Chain Monte Carlo
MEG	Magnetoencephalography
ODE	Ordinary Differential Equation
PDE	Partial Differential Equation
PV+	Parvalbumin positive
SNR	Signal to Noise Ratio
SWS	Spike and Wave Seizure
VB	Variational Bayes
WC	Wilson and Cowan

LIST OF APPENDICES

1 INTRODUCTION

1.1 Aims and outline of this thesis

1.1.1 General aims

The general aim of the work presented in this thesis is to establish techniques devoted to the biophysical modelling of oscillations in the brain and their estimation from experimental data. This aim was originally motivated by the possibility of clinical applications to focal epilepsies; namely, to the identification of patient-specific brain models conductive to a better understanding of their particular condition. However, this focused goal unveiled more fundamental problems that need to be resolved before it can be tackled. Specifically, how to appropriately model focal seizures with fast oscillatory onsets, and how to properly estimate models in the limit cycle regimes associated with epileptic brain activities.

Therefore, the following specific aims are addressed in this thesis:

1. To demonstrate that neural mass models are not suitable to describe fast seizure initiation, if the goal is to use them to biophysically constrain the analysis of clinical and experimental data.

2. To overcome the limitations of neural mass models for this purpose, by introducing a population model based on the Fokker-Planck equation and developing the appropriate numerical schemes that guarantee computational scalability.

3. To develop a Bayesian method for the estimation of the proposed model from experimental data focusing on limit cycle regimes, and to show its application to *in vitro*

electrophysiological recordings from mouse hippocampal slices, bridging single neuron recordings with network generated gamma oscillations.

1.1.2 Thesis outline

1.1.2.1 Introduction

The remainder of this introductory chapter will briefly present the basic concepts of epilepsy, models of seizure initiation and their bifurcations, models of fast neuronal oscillations, and existing estimation methods applied to neuronal models. These concepts will be the basis of the developments presented in the remainder of this thesis.

1.1.2.2 Chapter 2

In the second chapter bifurcation analyses of standard neural mass models aimed at finding fast oscillatory modes are presented. The aim is to understand if these classes of models are suitable to describe fast seizure initiation with the goal of using them to biophysically constrain the analysis of patient specific data. The analyses presented in the chapter suggest that fast oscillatory modes only arise with biophysically unrealistic parameterizations, highlighting the need for more detailed modelling strategies.

1.1.2.3 Chapter 3

In this chapter a population model based on the Fokker-Planck equation of stochastic, conductance-based, integrate-and-fire neurons is presented. A numerical method based on exponential integrators is developed to enable scalable and efficient solving of the ensuing partial differential equations. A repertoire of commonly observed behaviours is showcased for the model including fast oscillations, cross-frequency coupling and chaos.

1.1.2.4 Chapter 4

In the fourth chapter a Bayesian model estimation method aimed at models in limit cycle regimes is introduced. The method is applied primarily to the Fokker-Planck population model developed in the previous chapter, and its estimation is based on data from electrophysiological recordings of hippocampal slices (acquired by colleagues). The estimation of neural mass models of spike and wave absence seizures is also explored addressing clinical EEG.

1.1.2.5 Chapter 5

In the final chapter of this thesis we synthesize the findings of the previous chapters and suggest possible directions for future work.

1.2 What is epilepsy and what are seizures

Operationally, the definitions of "epilepsy" and "epileptic seizure" adopted by the International League Against Epilepsy were introduced in (Fisher et al., 2005), and follow:

> *"An **epileptic seizure** is a transient occurrence of signs and/or symptoms due to abnormal excessive or synchronous neuronal activity in the brain.*
>
> ***Epilepsy** is a disorder of the brain characterized by an enduring predisposition to generate epileptic seizures and by the neurologic, cognitive, psychological, and social consequences of this condition. The definition of epilepsy requires the occurrence of at least one epileptic seizure."*

Hence, Epilepsy, often referred to as "*the Epilepsies"*, encompasses a recognizable diversity in its pathophysiology and manifestations. Its prevalence in the population is often cited to be around the 0.5% (corresponding to 50 million worldwide) and, when medication is accessible, about 70% of the cases are respondent. (WHO, n.d.)

In cases where medication is not effective, patients may be candidates for resective surgery. These are conditions where the seizures are believed to initiate from a confined region of the brain, the seizure onset zone (SOZ); such conditions are classified as focal epilepsies (Berg et al., 2010). The goal of the surgery is to lesion the epileptogenic zone, which is defined, again operationally, as the minimal brain volume whose lesion results in seizure control. The main aim of the pre-surgical evaluation is to identify the brain regions involved in seizure activity, particularly the SOZ, which is often a crucial component to be resected. (Shorvon et al., 2012)

Nowadays a large plethora of clinical and imaging methods is available and contributes to the pre-surgical evaluation of epilepsy. However, when performed, the intracranially recorded EEG (icEEG) can be the most informative technique contributing to the decision of the areas which to resect.

1.2.1 Seizure onset and high frequency activity

Over the past two decades, with the advent of wide bandwidth EEG acquisition equipment, oscillations in the higher end of the icEEG spectrum have been increasingly linked to concepts of "epileptogenicity" (Bartolomei et al., 2008). These oscillations may occur at the onset of seizures (60 ~ 99 Hz) (Allen et al., 1992; Park et al., 2012) or during inter-ictal/pre-ictal events (Jacobs et al., 2009) and have been observed at up to 600 Hz. Furthermore the resection of areas showing this type of activity has been positively correlated with better surgical outcomes (Jacobs et al., 2008; Park et al., 2012).

The mechanistic understanding of these phenomena is still incomplete and several hypotheses overlap and vary according to the frequency ranges under scrutiny. Features as out-of-phase firing in neural clusters, strong excitatory AMPA synaptic currents and recurrent inhibitory connectivity appear to play key roles in epileptic high frequency oscillations ((Jefferys et al., 2012) and references therein).

1.2.2 Epilepsy and seizures: a network dysfunction perspective

Epilepsy is increasingly regarded as a condition emerging from networks, as opposed to single isolated regions, and therefore measures of connectivity are at the heart of several research efforts (Bertram et al., 1998; Lemieux et al., 2011; Spencer, 2002; Stefan and Lopes da Silva, 2013). The notions of the classification of focal and generalized epilepsies are also questioned as to rather be a matter of speed of generalization (Holmes et al., 2004; Stefan and Lopes da Silva, 2013). These perspectives can be formalized in a nonlinear dynamical system context, leading to the notion of the transition to seizure as form of bifurcation crossing (Grimbert and Faugeras, 2006; Jirsa et al., 2014; Wang et al., 2012), for example, in lumped models of neural populations as addressed in the following section.

1.3 Neural mass models

Neural mass models have a relatively long history in neuroscience. Since their inception in the 1970's (Wilson and Cowan, 1972; 1973;Lopes da Silva et al., 1974) they have been successfully used to improve our understanding of large-scale neuronal phenomena. Neural mass models consist of summary descriptions of the state of neuronal ensembles and different strategies may be adopted to arrive at mathematical

descriptions that share a common form with two main ingredients: a linear filtering operation and a static sigmoid non linearity.

In the context of the modelling of epileptic dynamics the most common form of neural mass models uses a second-order linear convolution operation to model a neural population's mean membrane response to presynaptic inputs. Each population is described by two state variables, the average post-synaptic potential of a population and its derivative. The instantaneous sigmoid nonlinearity is then applied to translate the mean membrane depolarization into a firing rate, endowing the system with nonlinear dynamics. Examples of applications of such models date back to Lopes da Silva et al. (1974), where they were used to study the alpha rhythm generated by the cortico-thalamic loop. Jansen and Rit (1995) developed a related model that has been applied to the study of cortical dynamics such as event related potentials (David et al., 2006), steady-state spectral responses (Moran et al., 2009;Friston et al., 2012) and epileptic spike and wave discharges (Lopes da Silva et al., 2003; Nevado-Holgado et al., 2012; Suffczynski et al., 2006).

The Jansen and Rit (JR) model (Ben H Jansen and Rit, 1995) describes a cortical column consisting of three coupled populations: an excitatory pyramidal cell population, whose average post-synaptic potential can be used to predict LFP/EEG signals, a secondary excitatory population and an inhibitory population. Several of these elementary, so-called "canonical", circuits can be coupled together to model the interactions of different brain regions as introduced in (David et al., 2006) and applied in, e.g., (Isabel and Garrido, 2008) to the study of event-related potentials (ERPs).

This family of models has been extended by Wendling and colleagues (Molaee-Ardekani et al., 2010; Wendling et al., 2005) to address the transition to seizure in focal epilepsies with fast oscillatory onsets (see a discussion of the approach's limitations in Chapter 2, page 25). By adding an extra fast inhibitory population representing peri-somatic targeting inhibitory interneurons, they showed how slow changes in the model parameters can lead to transitions that resemble the stereotypical evolution of focal seizure dynamics (Molaee-Ardekani et al., 2010; Wendling et al., 2005).

A slightly simpler family of neural mass models are based on the seminal work of Wilson and Cowan (WC) (Wilson and Cowan, 1972). Here the linear filtering operation is of first order, hence each population can be described with a single state variable representing the proportion of cells in the population that are excited at any given

instant in time; here, the sigmoid activation function embodies the fact that only a proportion of these cells are sensitive to pre-synaptic inputs. The simple yet powerful formulation of this family of models make them very popular in applications, e.g., (Akam et al., 2012; Nevado-Holgado et al., 2014), however their more abstract nature does not attempt to address membrane dynamics, and the time constants of the model reflect lumped population properties that cannot be directly assessed experimentally.

In (Marreiros et al., 2009) conductance-based neural mass models were introduced for the neuronal architectures considered by Jansen and Rit (see **Figure 1.1**). Conductance-based models of neuronal membrane dynamics date back to Lapicque (1907) (see (Brunel and van Rossum, 2007)). In contrast to convolution-based models, conductance-based models allow for an explicit representation of the activity of specific ion channels and the effects that these have on population dynamics. However, the average membrane responses of the populations no longer follow linear filter dynamics, making them slightly more nonlinear in nature. Furthermore, each population is now described by one state variable representing average membrane voltages and one extra variable for each family of synaptic ion channels modelled. Applications of this class of models include simulation studies (Moran et al., 2011a) and model inversions based on electrophysiological data (Marreiros et al., 2010;Moran et al., 2011b;Marreiros et al., 2012) with dynamic causal modelling (DCM) (Friston et al., 2003).

1.3.1 Bifurcation analyses of neural mass models

Convolution-based neural mass models have been the subject of comprehensive analytical and numerical studies. Lower dimensionality models, such as the two population WC model, can be analysed via phase plane techniques, e.g., (Borisyuk and Kirillov, 1992). Larger models such as the JR and its variants can be analysed via numerical simulations (Suffczynski et al., 2006; Wendling et al., 2005) and possibly use semi-analytical results and numerical continuation algorithms (Breakspear et al., 2006;Grimbert and Faugeras, 2006;Spiegler et al., 2010;Touboul et al., 2011). Of particular interest are the interpretations that relate specific bifurcation classes to epileptic phenomena. Namely, how Hopf bifurcations can be related to transitions that involve low amplitude oscillations appearing from fixed point like behaviours, and also, how homoclinic bifurcations can be related to epileptic spike behaviours, in the sense that large excursions appear from apparent fixed-point dynamics. These classes of

bifurcations are present in the JR model given particular parameterisations (Spiegler et al., 2010; Touboul et al., 2011).

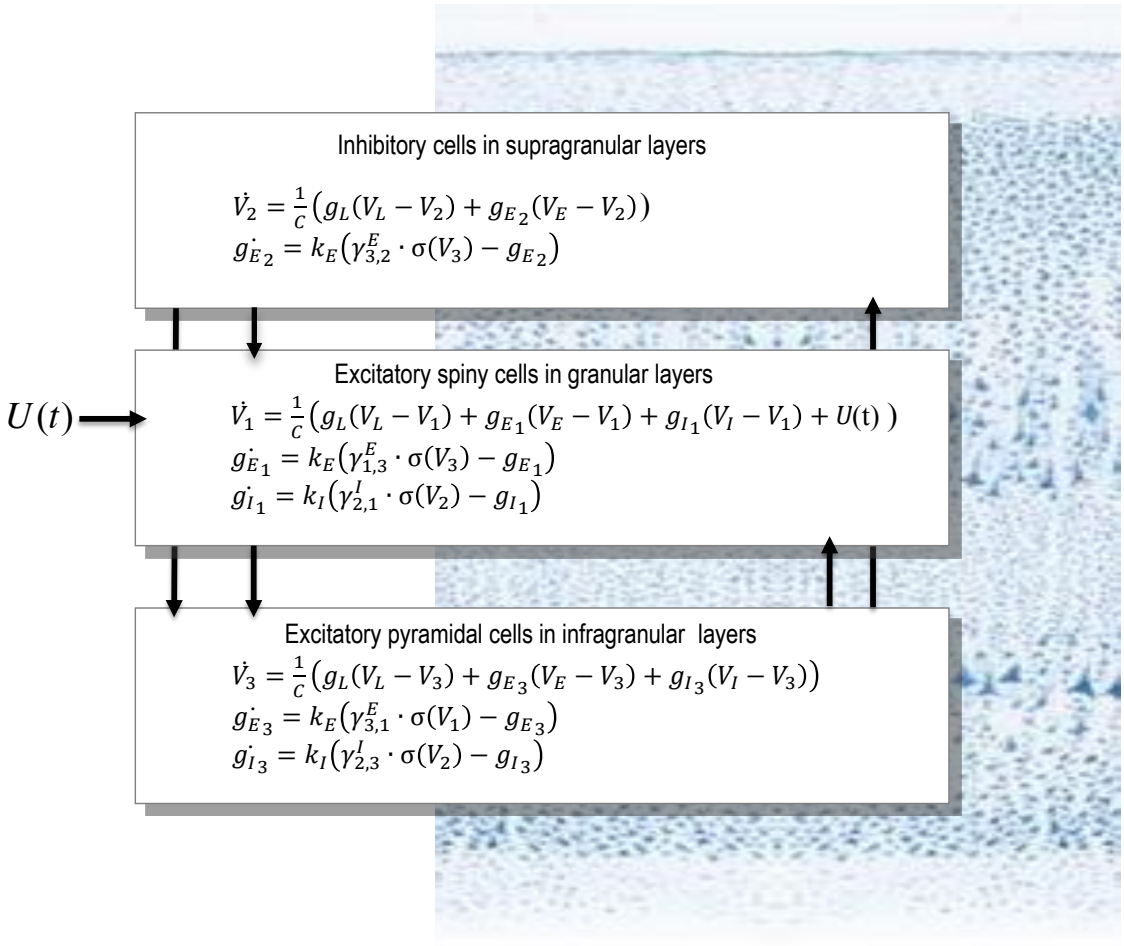

Figure 1.1 - Neuronal state-equations for a source model with a layered architecture comprising three interconnected populations (spiny-stellate, interneurons, and pyramidal cells), each of which has (at most) three different states (voltage "*V*", excitatory and inhibitory conductances, "*g*"). (Figure adapted from Marreiros et al., 2009).

This sort of interpretation from specific bifurcation patterns inspires a class of purely phenomenological models, which do not attempt to model directly neural parameters or biophysical quantities, but rather address how to describe these abstract dynamics with a minimal number of state variables, e.g., (Jirsa et al., 2014; Wang et al., 2012). These state variables can be related *ad hoc* to neurophysiological variables that correlate with the modelled dynamics (Jirsa et al., 2014).

Contrarily to the literature on convolution based neural mass models, conductance-based models lack exhaustive dynamical characterisation. This is important because the

dynamical repertoire of conductance-based models may limit their application in cognitive and clinical neuroscience. Also, the convolution-based neural mass models can be regarded as an approximation to the conductance based ones (Rodrigues et al., 2010), hence biophysical limitations of the dynamical repertoire of the first should be translated likewise in the latter. There has been a recent trend – especially in DCM practice – towards the use of conductance-based models, because they enable the modelling of specific currents and receptors, which may be the target of pharmacological interventions or indeed affected by disease (e.g., Moran et al., 2012). This motivated the work on fast gamma oscillations presented in chapter 2.

1.4 Fokker-Planck mean-field neuronal populations models

Mean-field treatments on stochastic models of single neurons based on the Fokker-Planck (FP) equation are alternative approaches to the modelling of populations of neurons. These models offer a good compromise between the mathematical and computational tractability of the lumped neuronal mass models (e.g. as reviewed in (Deco et al., 2008)) and the direct parameter and state space interpretability of the more detailed models of neural networks (e.g. (Tiesinga et al., 2001)), which can be directly related to experimental data. As discussed in the previous section, lumped neuronal mass models summarise neural population activity with a small number of lumped states (usually between one and four states per population), whose dynamics are then described by a small set of ordinary differential equations (ODEs). In contrast, mean-field FP models track the full probability density of the stochastic neuronal state variables of the neurons in the population. The dynamics of the population are accordingly embodied in sets of partial differential equations (PDEs). The mean-field approach retains the interpretation of the state variables as in single neuron models, under the simplifying assumption that all neurons are assigned the same parameters, are only differentiated by random state fluctuations and are effectively infinite in number. These are approximations that explicit network models of multiple neurons eschew, and can therefore address questions about neuronal heterogeneity, for example, that cannot be easily addressed by mean-field FP models (e.g. (Burkitt, 2006)).

The mean field modelling of (non-lumped) neuronal populations dates back to the 1990s (Abbott and van Vreeswijk, 1993; Brunel and Hakim, 1999; Gerstner, 2000;

Knight, 2000), followed by developments based on the dynamical formalism of full neural population densities in a mean-field FP model context (e.g. (Baladron et al., 2012; Harrison et al., 2005; Knight, 2000; Kovacic et al., 2009; Marpeau et al., 2009; Mattia and Del Giudice, 2004; Mattia and Giudice, 2002)). The most popular family of neuronal models used in mean-field FP approaches consists of variants of the leaky-integrate-and-fire (LIF) neurons (Brunel and van Rossum, 2007). The fact that these neuronal models can usually be described by a single state variable makes them particularly appropriate since the computational cost of solving FP equations grows exponentially with the number of state variables of the single neuron model. Notable exceptions exist, e.g. (Baladron et al., 2012), wherein FP models of the six-dimensional Hodgkin-Huxley neuron model are explored.

Of particular interest here are studies where FP models of LIF neurons are used to study gamma oscillations (Brunel, 2000; Brunel and Hakim, 2008, 1999; Brunel and Wang, 2003). In these studies, analyses of FP models of coupled excitatory and inhibitory LIF neurons are used to illustrate several alternative population states, such as, asynchronous or oscillatory regimes; the latter can be dominated by the excitatory-inhibitory loop (sometimes coined PING, for pyramidal-interneuron gamma) or the inhibitory-inhibitory loop (sometimes coined ING, for interneuron gamma). These oscillations can arise either with regular or sparse firing of the neurons of each population depending on the strength of the connections and stochastic drive for each population. In other words, all these different model regimes have been found to have a level of validity, and specific physiological and experimental conditions may be explained by any combination of such regimes. In chapter 4 we develop methods that allow the identification of the properties of the model for specific conditions given experimental data.

1.5 Neuronal model estimation

The estimation of statistical models of neuronal activity based on neurophysiological measurements has received substantial attention in the past decade. Two broad categories can be distinguished with regards to estimation strategies: one in which stochastic hidden states of the models are explicitly estimated, and another in which model estimations are based on summary statistics, eschewing stochastic hidden state estimation.

1.5.1 Estimation of models with stochastic dynamics

Examples for both single-neuron and population models exist in which the estimation of model parameters relies on the direct estimation of the trajectories for the underlying stochastic dynamical models. These estimations have been made based on neuronal spike train data to estimate, e.g., single LIF neuron parameters (Pillow et al., 2004) or population rate empirical models with linear dynamics (Buesing et al., 2012), coping with the difficulty of handling non-Gaussian observation models due to the sparse nature of spike trains. However, perhaps more commonly, the data features used to estimate neural population models can be assumed to have Gaussian observation noise, e.g. LFP, EEG, fMRI. In these instances, approaches based on generalizations of Kalman-filtering, extended to handle non-linear dynamics and parameter estimation (Daunizeau et al., 2009; Friston et al., 2010, 2008; Havlicek et al., 2011), have been applied to a wide variety of scenarios, including seizure dynamics as modelled by the JR model (Freestone et al., 2014; López-Cuevas et al., 2015; Ullah and Schiff, 2010). These approaches have the advantage of allowing online model estimation; however, for more complex models and long datasets, they can become computationally very intensive.

1.5.2 Estimation of models with deterministic dynamics

Alternative approaches to the explicit modelling of stochastic dynamical systems, rely on extracting summary statistics from data, and use these to inform models with deterministic dynamics but noisy observations. Examples of such strategies include estimating exponential LIF single neuron models based on dynamic input-to-voltage curves measured *in vitro* from different classes of neurons (Badel et al., 2008a), estimating WC population models with cycle averaged *in vivo* firing rates (Nevado-Holgado et al., 2014) and a vast literature on neural population model estimations based on Dynamic Causal Modelling (DCM) (Friston et al., 2003) for M/EEG, LFP and fMRI data.

In the context of deterministic DCM (Friston et al., 2003), the literature has mainly focused on approaches based on the study of models in stable fixed point configurations, and subsequently analysing how they behave with respect to perturbations. These perturbations can be small and random such that linearised approximations of the neuronal population models can be used to predict the resulting

summary cross spectral responses of the measured fMRI, M/EEG or LFP (Friston et al., 2014, 2012; Moran et al., 2009). The perturbations can also be deterministic and with possibly larger amplitudes, and the estimation of the models can be based on the analysis of how the system relaxes back to the stable fixed point, as in the case of M/EEG ERP average responses (David et al., 2006; Friston et al., 2003; Penny et al., 2009).

However, there is increasing interest in using these techniques to analyse oscillations that are more non-linear in nature, e.g. EEG of epileptic seizure dynamics (Cooray et al., 2015; Papadopoulou et al., 2015), albeit current DCM techniques are not fully adapted to the analysis of limit cycle dynamics. In these studies the summary cross-spectra of short windows of EEG/LFP acquired during seizures was used to inform model estimation. However, since these analyses are intrinsically linear, they cannot address specifically the bifurcation crossing interpretations of seizure dynamics.

The general family of approaches based on deterministic dynamics have the advantage of not having to deal with the added complexity of uncertainty on the dynamics of the hidden states of the models, and also the computational advantage of using smaller datasets for the model fits. However, implicit stationary assumptions of the data have to be made, i.e., the summary statistics of the data must remain constant throughout acquisition.

1.5.3 Single neuron versus population models

In the aforementioned estimation approaches, neural population models are usually based on the lumped JR and WC family of models, whose relation to the single neuron dynamics has been abstracted for the benefit of simplified dynamics. Hence the measurements addressable by such models are also agglomerate population properties such as local field potentials (LFP), and their predictive capacity is also more difficult to assess. At the other end of the spectrum lie the techniques devoted to the estimation of single neuron models (Badel et al., 2008a, 2008b; Gerstner and Naud, 2009) that enjoy remarkable predictive value under very well controlled conditions, but are unable to address how these properties impact behaviour at the population level. Approaches that bridge these two scales and levels abstraction are lacking in the literature.

1.6 Summary and conclusions

Mathematical and computational modelling are important tools in neuroscience due to the complexity of the systems under study. They are important not only to illustrate theoretical mechanisms that can reproduce neural phenomena, but also to synthesize experimental data into coherent conceptual and quantitative frameworks. In this chapter we have described how some of these models address the phenomenology of epileptic seizures or bridge single neuron properties to its neural population behaviour. We have also surveyed the strategies used to estimate neural models from experimental data.

In the following chapters we seek to further extend these perspectives by accommodating biophysically plausible models and estimation methods to the study of gamma oscillations.

2 BIFURCATION ANALYSIS OF A CONDUCTANCE BASED NEURAL MASS MODEL[1]

In this chapter we investigate, by means of bifurcation analyses, the dynamical repertoire of a commonly used conductance-based neural mass model with three neuronal populations. We extend the analyses to study the spectral responses of the system in the small perturbation limit, and focus on the constraints necessary for the emergence of fast gamma oscillatory modes. We find that, for physiologically plausible model parameters, the maximum peak frequencies of the spectral response of the system are below 60 Hz. We conclude by arguing that parameterizations showing fast gamma activity (range: ~60 -120 Hz) are either not physiologically plausible or violate model assumptions. This may have important implications for the use of these models as forward (dynamic causal) models of recorded brain activity, or as generative models of emergent behaviour in cognitive neuroscience (e.g., attention research) or clinical neuroscience (e.g., epilepsy).

[1] This chapter is the subject of an article entitled "Bifurcation analysis of conductance based neural mass models" submitted to NeuroImage

2.1 Introduction

In this chapter we seek to investigate if conductance based neural mass models are suitable to model the fast oscillations observed at the start of focal epileptic seizures. This class of models are computationally very tractable while offering insights at membrane current dynamics and specific ion-channel characteristics. As such, they are the ideal first candidates to use in conjunction with model estimation techniques in order to address the mechanisms behind specific clinical or experimental data. The emphasis here is to potentially identify physiologically plausible parameter regions that produce fast oscillations (~>60 Hz) as reported in previous works addressing this model (Moran et al., 2011) or its approximations (Molaee-Ardekani et al., 2010).

We then perform a bifurcation analysis of the conductance-based neural mass model introduced in (Marreiros et al., 2009), including a description of the spectral response of the system under different parameterisations. We start by rewriting the model equations compactly in vector form to find their stationary points analytically, and then evaluate local stability and spectral responses at these fixed points. In the event of local instabilities, we proceed to explore the system's limit cycle behaviour through numerical integrations. In order to frame the results obtained in the larger context of bifurcation analyses of neural mass models, we translate the model equations, via a series of approximations, to a second order differential equation similar to the Jansen and Ritt convolution-based neural mass model.

2.2 Methods

2.2.1 Model equations

The equations of motion for the system under consideration are presented schematically in **Figure 1.1**. For economy of notation, we introduce a set of equations that describe an arbitrarily connected conductance-based model by grouping in vector form, for all populations, the mean membrane potential, V, mean excitatory conductance, g_E, and mean inhibitory conductance, g_I:

$$\dot{V}(t) = \frac{1}{C}\left(g_L(V_L - V(t)) + g_E(t) \circ \left(V_E - V(t)\right) + g_I(\mathrm{t}) \circ (V_I - V(t)) + U(t)\right)$$

$$\dot{g_E}(t) = k_E(\Gamma_E \cdot \Sigma(V(t)) - g_E(t)) \tag{2.1}$$

$$\dot{g_I}(t) = k_I(\Gamma_I \cdot \Sigma(V(t)) - g_I(t))$$

where, the symbol "$\circ$" denotes the Hadamard product (matrix or vector "entry by entry" multiplication), Γ_E and Γ_I are excitatory and inhibitory connectivity matrices between the populations, with channel reversal potentials V_E and V_I, respectively. The function $\Sigma(V(t))$ denotes a sigmoid activation function, σ, applied to depolarisation $V(t)$. In the present case, the sigmoid function is the cumulative probability function of a normal distribution (see (Marreiros et al., 2008) for a detailed motivation). The variable $U(t)$ denotes a vector of population-specific exogenous inputs, and C is the cell membrane capacitance. The terms g_L and V_L represent the membrane leakage conductance and reversal potential, respectively. Finally, k_E and k_I are the time constants of the first order synaptic filter.

2.2.2 Stationary points

By definition, the stationary points of a system are the points in state space at which all time derivatives are equal to zero. We will now briefly go through some manipulations that allow us to derive an explicit solution for the stationary points of the system presented above. First, note that the conductance terms, at the stationary points, are functions of the voltages, specifically, of the form:

$$0 = k(\,\Gamma \cdot \Sigma(V^0) - g^0) \Leftrightarrow g^0 = \Gamma \cdot \Sigma(V^0) \tag{2.2}$$

Having noted this, the problem of finding the stationary points reduces to solving the following system of nonlinear equations:

$$0 = g_L(V_L - V^0) + \left(\Gamma_E \cdot \Sigma(V^0)\right) \circ (V_E - V^0) + \left(\Gamma_I \cdot \Sigma(V^0)\right) \circ (V_I - V^0) + U^0 \tag{2.3}$$

We employ the particular form of the matrices Γ_E and Γ_I, and the vector U, which ensure a closed form solution in the case of the three cortical populations of **Figure 1.1**:

$$\Gamma_E = \begin{bmatrix} 0 & 0 & \gamma_{1,3}^E \\ 0 & 0 & \gamma_{2,3}^E \\ \gamma_{3,1}^E & 0 & 0 \end{bmatrix}; \Gamma_I = \begin{bmatrix} 0 & \gamma_{1,2}^I & 0 \\ 0 & 0 & 0 \\ 0 & \gamma_{3,2}^I & 0 \end{bmatrix} \text{ and } U(t) = \begin{bmatrix} u^0 \\ 0 \\ 0 \end{bmatrix} \tag{2.4}$$

We can now use this system of equations to derive the stationary points as a function of V_3^0: using the second line of the Γ matrices, V_2^0 is given by:

$$V_2^0 = \frac{g_L \cdot V_L + \gamma_{2,3}^E \cdot \sigma(V_3^0) \cdot V_E}{g_L + \gamma_{2,3}^E \cdot \sigma(V_3^0)} \tag{2.5}$$

Using the third line of the Γ matrices we can express V_1^0 in terms of V_2^0 and V_3^0:

$$V_1^0 = \sigma^{-1}\left(-\frac{g_L \cdot (V_L - V_3^0) + \gamma_{3,2}^I \cdot \sigma(V_2^0) \cdot (V_I - V_3^0)}{\gamma_{3,1}^E \cdot (V_E - V_3^0)}\right) \tag{2.6}$$

This result is valid if σ^{-1} is defined at that point; i.e., if its argument lies between 0 and 1. Now using the first line of the matrices, we obtain:

$$u^0 = -\left(g_L(V_L - V_1^0) + \gamma_{1,3}^E \cdot \sigma(V_3^0) \cdot (V_E - V_1^0) + \gamma_{1,2}^I \cdot \sigma(V_2^0) \cdot (V_I - V_1^0)\right) \tag{2.7}$$

Equations (2.5), (2.6) and (2.7) provide a closed form expression for the stationary points of the system as a function of V_3^0.

2.2.3 Stability and oscillatory modes

The stability and oscillatory response of the system at the stationary points can be evaluated by tracking the eigenvalues of the Jacobian of the equations of motion, *f*, of the entire system. Specifically, we express equation (2.1) in terms of collective states *X*:

$$\begin{gathered} \dot{X(t)} = f\big(X(t)\big) \\ X(t) = [V(t)^T \; g_E(t)^T \; g_I(t)^T]^T \end{gathered} \tag{2.8}$$

Hence the Jacobian of $f(X)$ can be expressed as:

$$J = \begin{bmatrix} -\frac{1}{C}\left(g_L \cdot I + diag(g_E(t) + g_I(t))\right) & \frac{1}{C}diag\left(V_E - V(t)\right) & \frac{1}{C}diag\left(V_I - V(t)\right) \\ k_E \cdot \Gamma_E \cdot \mathrm{diag}(\Sigma'(V(t))) & -k_E \cdot I & \overline{0} \\ k_I \cdot \Gamma_I \cdot \mathrm{diag}(\Sigma'(V(t))) & \overline{0} & -k_I \cdot I \end{bmatrix} \quad (2.9)$$

In our case of three populations, J is a 9 by 9 matrix, organized in blocks of 3 by 3 matrices. Here '*diag'* stands for a diagonal matrix with the argument vector on its diagonal (as in MatLab code) and *I* is the identity matrix. The eigenvalues of this matrix have no closed-form solution (the eigenvalues consist of $-k_I, -k_E$ and the roots of a 7th order polynomial expression), but can be evaluated numerically when required.

The (linear) spectral response of the system can be derived from the eigenvalues of the Jacobian; see Appendix A. In brief, for a spectral peak at frequency *f*, the Jacobian will have a pair of conjugate eigenvalues with imaginary parts close to $\pm 2\pi f$, where the height of the spectral peak will be determined by how close their real part is to zero. If time delays are introduced in the equations of motion (e.g. representing axonal conduction times), the spectral response of the system near stationary points changes (the stationary points themselves do not change, but their stability may be altered). An exact solution for the spectral responses of time delay models is given in Appendix A, (and was the solution used in this work) – where an approximation for the Jacobian is given in (David et al., 2006). We will not report results under different delays, but note that more intricate spectra, with sharper peaks (resonant structures), emerge with large delays; however, for standard values (~2ms), delays have a relatively modest impact and, to simplify our analysis, we set them to zero.

In what follows, we report the spectral behaviour of the conductance-based model above under different parameterisations. When the fixed points where unstable, the system was numerically integrated – to obtain the form and time period of the system's stable limit cycles.

2.2.4 Explorations under different parameterizations

We initially set the parameter values to the model priors used in (Moran et al., 2011a) (see Table 2.1). **Figure 2.1** shows the bifurcation diagram obtained by varying the exogenous input *u*. The bifurcation profile shows two supercritical Hopf bifurcations, delimiting a region where the only fixed point of the system loses stability. The spectral profile under small perturbations also changes considerably when changing the

exogenous input strength: for low or very high inputs (**Figure 2.1**, A and E), the system shows a broadly peaked spectrum; while for intermediate values (**Figure 2.1**, B and D), the system shows a sharp peak at around 10 Hz as it approaches instability (**Figure 2.1**, C). The peak frequency generally increases from 10 to 20 Hz, as the intensity of the exogenous input increases.

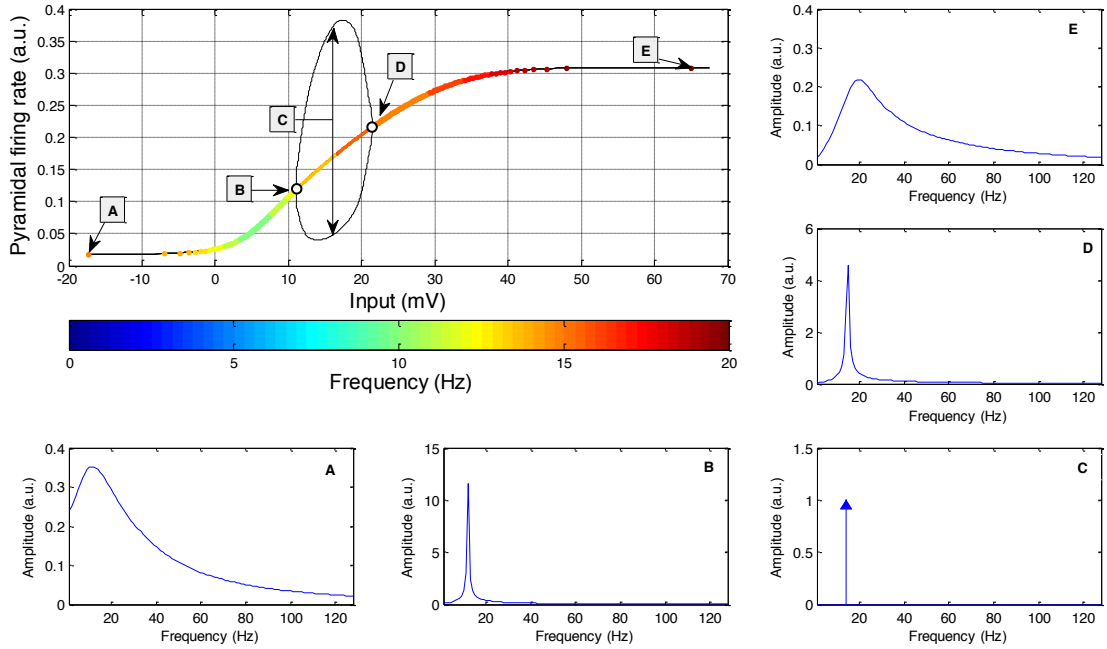

Figure 2.1 - Bifurcation diagram for the standard parameter values, under varying exogenous input strengths. The fixed points are evaluated at equally spaced pyramidal firing rates and the peak frequencies of the spectral responses are colour coded. Illustrative examples of the spectral responses under small perturbations are plotted alongside in panels A, B D and E. Panel C represents schematically the frequency of the self-sustained oscillation. Supercritical Hopf bifurcations are marked with white circles. Maximum and minimum firing rates for the limit cycle are also shown plotted in black.

We explored the system's fast oscillatory regimes by altering the system parameter values such that, heuristically, the Jacobian would be as "large" and antisymmetric as possible, yet maintaining the parameters within the limits of physiological plausibility. For plausibility, we took as a reference the measurements in (Badel et al., 2008a) and (Badel et al., 2008b). The value for the membrane time constant adopted for the previous analysis was already the lower bound of their reports; i.e. C/gl = 8 ms. Using the arguments presented in (Marreiros et al., 2008), the dispersion of depolarisation in

each population is a lower bound on the dispersion of the Gaussian whose cumulative distribution is the sigmoid activation function. In this instance, we took as reference the coefficient of variation of the measure of the difference between the neuronal spiking threshold voltage and the membrane resting potential, V_t-V_L, which was 22% (Badel et al., 2008a;Badel et al., 2008b). This translates to a value of the dispersion parameter, *s,* equal to 6 mV. The lower bounds for the excitatory and inhibitory synaptic time constants were set to 2 ms, following (Molaee-Ardekani et al., 2010); we note that these are the values observed for perisomatic dendritic synapses. (Please refer to Table 2.1 for a summary)

The strength of (intrinsic) connections between populations will also affect the rates at which the system will oscillate, where excitatory-inhibitory loops are of crucial importance. In this context, there is no clear basis on which the parameters can be bound– other than the fact that they should be roughly the same order of magnitude as the leakage conductance. Therefore we investigated the effect of a scaling parameter ($e^{\alpha}, \alpha \in [-3, 3]$) on the inhibitory connectivity matrix. The excitatory connections were also investigated, but these had a smaller impact on the system's oscillatory behaviour (as their effect on the antisymmetric part of the Jacobian is less pronounced).

To illustrate the effects the above parameters have on system behaviour, we plotted bifurcation diagrams with two bifurcation parameters: the exogenous input, u, and the scaling of the inhibitory connectivity matrix, α; first under the default parameterization (**Figure 2.2** A), and then – changing in sequence – synaptic time constants, k_i, (**Figure 2.2** B) and the sigmoid activation function slope, s^2 (**Figure 2.2** C). Table 2.1 shows the range of parameter values explored (from standard to limit values).

Under the default parameterization (**Figure 2.2** A), the system shows, for a large range of inhibitory strengths, the limit cycle presented in **Figure 2.1** (which can be regarded as a cut along the plane $\alpha=0$). As inhibition increases ($\alpha>0$), the frequency and amplitude of this limit cycle increase. However, if inhibition decreases ($\alpha<0$), a different bifurcation dependency on the exogenous input appears: the limit cycle starts to decrease in amplitude and frequency, until it disappears. Close to the point where the limit cycle disappears, there is a cusp (codimension-2) bifurcation where two limit point bifurcations (codimension-1), also known as 'fold bifurcations', emerge. The surface of the fixed points is "folded" and a region with two stable (and one unstable) fixed points emerges.

Table 2.1 - Model parameters, physiological interpretation and values used in the analyses.

Constant	Symbol	Standard Value	Limit Value
Excitatory inverse time constant	k_E	1/2 ms^{-1}	1/2 ms^{-1}
Inhibitory inverse time constant	k_I	1/16 ms^{-1}	1/2 ms^{-1}
Excitatory reversal potential	V_E	60 mV	-
Inhibitory reversal potential	V_I	-90 mV	-
Leakage reversal potential	V_L	-70 mV	-
Normalized Leakage conductance	g_L	1 a.u.	-
Excitatory connection strengths	Γ_E	$\begin{bmatrix} 0 & 0 & ½ \\ 0 & 0 & 1 \\ ½ & 0 & 0 \end{bmatrix}$ a.u.	-
Inhibitory connection strengths	Γ_I	$\begin{bmatrix} 0 & ¼ & 0 \\ 0 & 0 & 0 \\ 0 & 1 & 0 \end{bmatrix}$ a.u.	$\begin{bmatrix} 0 & ¼ & 0 \\ 0 & 0 & 0 \\ 0 & 1 & 0 \end{bmatrix} \cdot e^{\alpha}$ a.u. $\alpha \in [-3, 3]$
Normalized membrane capacitance	C	8 ms ($pF \cdot nS^{-1}$)	8 ms ($pF \cdot nS^{-1}$)
Sigmoid activation function	$\sigma(V)$	$½ \cdot (1+\mathrm{erf}[(V-V_t)/(2 \cdot s^2)^{½}])$ a.u.	-
Firing threshold	V_t	-40 mV	-
Population dispersion	s^2	75 mV^2	36 mV^2

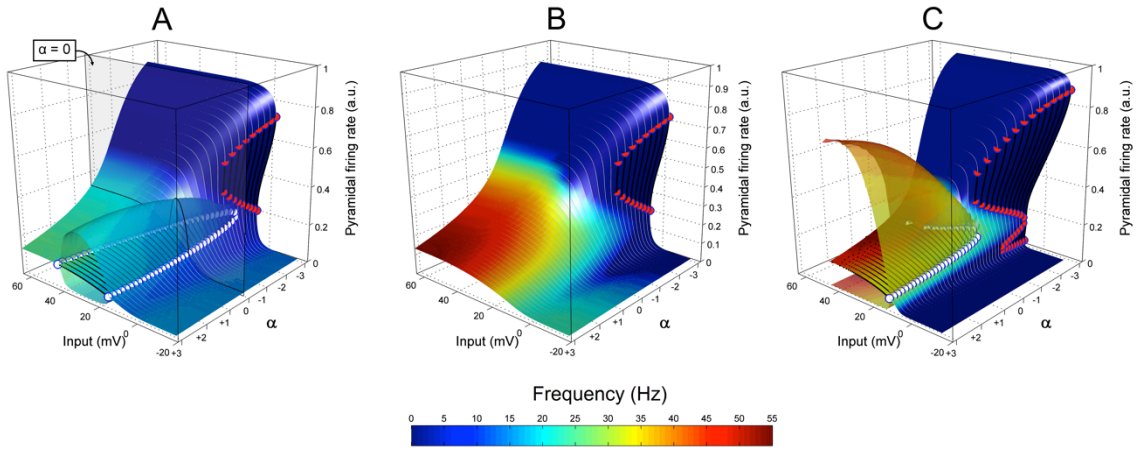

Figure 2.2 - Bifurcation diagrams for different parameter values: the exogenous input strength and the inhibitory scaling α were the free bifurcation parameters. (A) Standard parameters, (B) Fast synaptic constants, (C) Fast synaptic constants + high sigmoid activation function slope. The solid surfaces indicate pyramidal firing rates at the fixed points, and transparent surfaces indicate maxima and minima of limit cycles. Black dotted lines indicate unstable fixed points and grey dots indicate stable ones. White circles indicate the occurrence of Hopf bifurcations, and red circles indicate limit point bifurcations. The surfaces are colour-coded for the peak frequency of the spectral response of the system. The transparent vertical plane α = 0 in (A) corresponds to the cut presented in **Figure 2.1**.

When the synaptic time constants are decreased (**Figure 2.2** B), the fixed points remain unaltered, yet their local stability increases, such that the region previously showing limit cycles no longer exists over the range of α values considered. Furthermore, the peak frequencies of the spectra generally increase, reaching 50 Hz with very high inputs and inhibitory strengths. When the slope of the sigmoid function is increased (**Figure 2.2** C), the local stability of the fixed points at high inhibition and input strengths is again lost – and a region with a limit cycle emerges again, delimited by supercritical Hopf bifurcations. The general structure of the surface of fixed points is transformed and – for a certain region of low inhibition and moderate input strength – new limit point bifurcations appear, establishing a small region with three stable (and two unstable) fixed points. Regarding the spectral response of the system, the maximum peak frequency encountered is now around 55 Hz, again for high inhibition and input strengths. In this case, the peak frequency is found for a limit cycle whereas previously it was found for a stable fixed point. The imaginary part of the pair of eigenvalues that have positive real parts at the unstable fixed point is approximately 65 Hz, yet the time

constants of the system do not afford stability for such fast oscillations, resulting in the reduced oscillatory frequency of the limit cycle. For completeness, an increased range of connection strengths is also presented in Appendix B – the results are similar to **Figure 2.2**.

2.2.5 Mapping to a linear second order model for the membrane response

In this section we will follow one of the approaches presented in (Rodrigues et al., 2010), and map the conductance based model discussed so far, to a more widely used linear second order differential system for the membrane response of the populations. We will then illustrate the effect of this mapping in the different bifurcation profiles and spectral responses portrayed in **Figure 2.2**.

To make such mapping one must make the following set of approximations:

- Consider the effects of each synaptic family on the population mean membrane voltages separately, and then, consider their effect on the population firing rate to be additive.
- Consider the difference between the reversal potential of each channel and the time varying membrane voltage constant and approximated by an "average effective voltage", i.e., $V_E - V(t) \approx \bar{V}_E$ and $V_I - V(t) \approx \bar{V}_I$.

Furthermore, to simplify the equations and to improve the mapping towards previous literature (e.g. Grimbert and Faugeras, 2006; Touboul et al., 2011, etc), we also perform a change of variables in the voltage terms, such that the leakage reversal potential is set to zero.

In concrete terms, the membrane response to excitatory synaptic inputs with instantaneous firing rate $\phi(t)$, for example, now becomes:

$$\begin{aligned} \dot{V}_{Eeff}(t) &= \frac{1}{C}\left(-g_L \cdot V_{Eeff}(t) + g_E(t) \cdot \bar{V}_E\right) \\ \dot{g_E}(t) &= k_E(\phi(t) - g_E(t)) \end{aligned} \tag{2.10}$$

Rearranging:

$$g_E(t) = \frac{C}{\bar{V}_E} \cdot \dot{V}_{Eeff}(t) + \frac{g_L}{\bar{V}_E} \cdot V_{Eeff}(t)$$

$$\frac{\partial}{\partial t}\left(\frac{C}{\bar{V}_E} \cdot \dot{V}_{Eeff}(t) + \frac{g_L}{\bar{V}_E} \cdot V_{Eeff}(t)\right) = k_E\left(\phi(t) - \left(\frac{C}{\bar{V}_E} \cdot \dot{V}_{Eeff}(t) + \frac{g_L}{\bar{V}_E} \cdot V_{Eeff}(t)\right)\right) \tag{2.11}$$

Applying the time derivative operator and simplifying, one gets the following second order ODE:

$$\ddot{V}_{Eeff} = -\left(\frac{g_L}{C} + k_E\right)\dot{V}_{Eeff}(t) - \frac{k_E \cdot g_L}{C} V_{Eeff}(t) + \frac{k_E \cdot \bar{V}_E}{C}\phi(t) \tag{2.12}$$

Here $V_{Eeff}(t)$ represents the average excitatory postsynaptic potential that a population with firing rate $\phi(t)$ exerts over its efferent populations, apart from possibly a linear gain. The same treatment can be made regarding other types of channels, adapting the effective reversal potentials, $\bar{V}$, and the time constants, k, accordingly. The firing rate, $\phi(t)$, of a population affected by, e.g., inhibitory and excitatory connections, is then given by:

$$\phi(t) = \Sigma_L(\Gamma_E \cdot V_{Eeff}(t) + \Gamma_I \cdot V_{Ieff}(t) + U(t)) \tag{2.13}$$

Here $\Sigma_L(V) = \Sigma(\mathrm{V} + V_L)$ to account for the change of variables made in the voltage terms. The $V(\mathrm{t})$ terms are the voltage effect each population exerts over its efferent populations, which are then multiplied by the linear gain matrices Γ.

Assuming now the same model architecture as before (see **Figure 1.1**), the resulting model resembles Jansen and Rit's (B H Jansen and Rit, 1995) with two key differences:

- The time constants of the post synaptic response are now separated into synaptic conductance time constant, k, and membrane time constant, g_L/C. A complete equivalence is reached if $g_L/C = k$.
- The external input affects the secondary excitatory population (spiny stellate), instead of directly affecting the principal pyramidal cell population.

Again, this system has a closed form solution for the fixed points as a function of the pyramidal population mean voltage and it can be obtained with a treatment similar to the one made in (Touboul et al., 2011):

$$V_2^0 = \frac{\bar{V}_E}{g_L}\sigma_L(\gamma_{2,3}^E \cdot V_3^0)$$

$$V_1^0 = \frac{\sigma_L^{-1}\left(\frac{g_L}{\bar{V}_E} \cdot V_3^0\right) - \gamma_{3,2}^I \cdot V_2^0}{\gamma_{3,1}^E} \tag{2.14}$$

$$u^0 = \sigma_L^{-1}\left(\frac{g_L}{\bar{V}_E} \cdot V_1^0\right) - \gamma_{1,2}^I \cdot V_2^0 - \gamma_{1,3}^E \cdot V_3^0$$

Subject to σ_L^{-1} being defined for its arguments.

Performing the same analysis as in **Figure 2.2** but now for the mapped second order model, the bifurcation profiles of

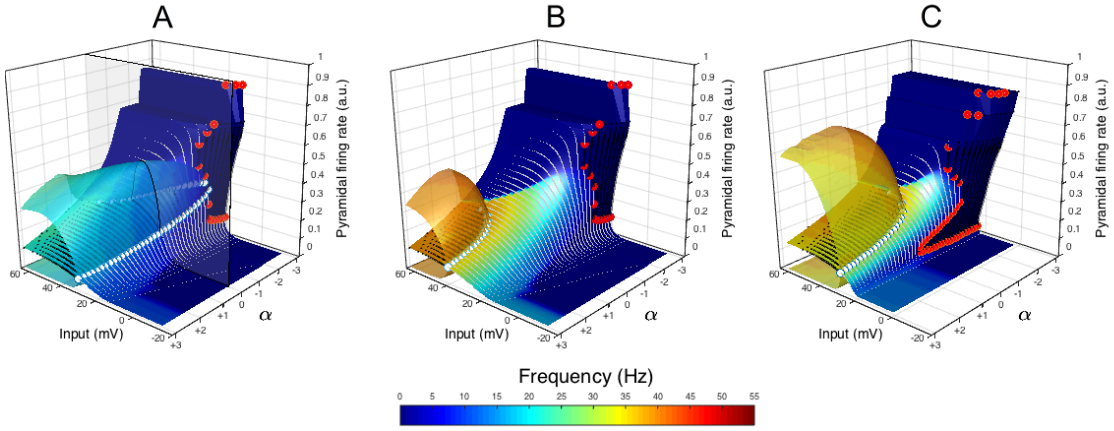

Figure 2.3 are obtained. The same parameter ranges were used, apart from an adaptation of the $\Sigma_L(V)$ function, which consisted in a 0.5 scaling of its slope to accommodate the new effective reversal potentials, $\bar{V}_E = 100\,mV$ and $\bar{V}_I = -50\,mV$, and generate comparable bifurcation profiles.

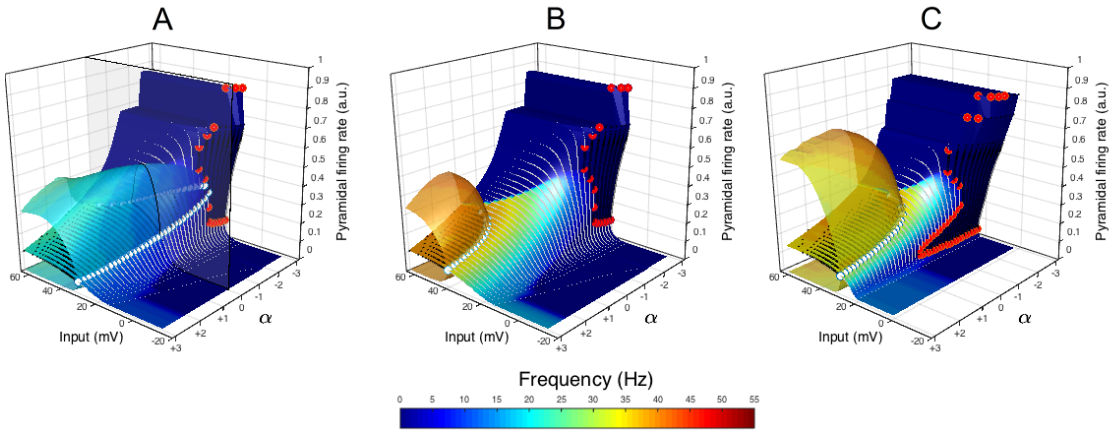

Figure 2.3 - Bifurcation diagrams, as in **Figure 2.2**, but for the mapped second order model: the exogenous input strength and the inhibitory scaling α were the free bifurcation parameters. (A) Standard parameters, (B) Fast synaptic constants, (C) Fast synaptic constants + high sigmoid activation function slope. The solid surfaces indicate pyramidal firing rates at the fixed points, and transparent surfaces indicate maxima and minima of limit cycles. Black dotted lines indicate unstable fixed points and grey dots indicate stable ones. White circles indicate the occurrence of Hopf bifurcations, and red circles indicate limit-point bifurcations. The surfaces are colour-coded for the peak frequency of the spectral response of the system.

The general properties of the bifurcation structure of the model are maintained given that the slope of $\Sigma_L(V)$ is properly scaled. The most prominent difference is that time constants of the mapped model are slightly decreased when compared to the conductance-based model, resulting in less stable fixed points and slightly decreased oscillation frequencies. A wide range of bifurcation profiles is obtainable with this model structure, by changing the connectivity matrices and population parameters (Spiegler et al., 2010), however, using the parameter ranges of Table 2.1 fast oscillatory modes remain elusive.

2.3 Discussion

We have presented a bifurcation analysis of a conductance-based neural mass model, using analytical results and complementing them, when necessary, with numerical integrations. This analysis illustrates the effect of key neuronal parameters on the dynamical behaviour of the system. This allowed us to identify previously unreported (Moran et al., 2011a) regions of multi-stability and – importantly – show that, for

physiologically plausible parameterizations, membrane and synaptic time constants prohibit the expression of very fast modes (>60 Hz), in the model architecture considered. This comes in contrast with the numerical results previously reported in (Moran et al., 2011a), whereby regions of high gamma are apparent. However, these results come from regions where the numerical precision of the algorithms used therein is compromised.

Complementing the analysis of the conductance based neural mass model, we mapped its structure and parameters to a linear second order model of the neuronal population membrane response. This allows for a direct comparison of the results discussed so far to the broader literature on this family of models. Namely, we show that by separating the traditional use of a single population time constant into a synaptic component (k_e) and a membrane response component (g_L/C), fast oscillations (e.g. (Molaee-Ardekani et al., 2010; Wendling et al., 2012)) only become viable with unrealistically fast membrane time constants.

We consider this an important limitation given the potential importance of fast oscillatory components of induced responses, and their potential importance in a clinical setting – such as epilepsy research. In what follows, we consider some of the limitations of the class of models we have considered in this chapter, and comment upon alternatives for future work.

2.3.1 Limitations of the neural mass model

The formal derivation of the model considered here (Marreiros et al., 2008;Marreiros et al., 2009) simplifies neuronal spiking mechanisms, assuming binary neurons that are in one of two states: firing, if the membrane potential is above threshold, or at rest, if below threshold. This approach does not model spiking effects such as membrane voltage resetting or refractoriness, which are thought to be important for fast oscillatory activity (as comprehensively reviewed in (Wang, 2010)). Alternative neural mass model derivations like Wilson and Cowan's (Wilson and Cowan, 1972) are based on different, but equally limiting, assumptions, namely that the activity of the populations change slowly (Wilson and Cowan, 1973;Abbott and van Vreeswijk, 1993), and that the time constants of the population can be related to neural membrane time constants (Gerstner, 2000), as we did in the present work. Models with these properties can be used as minimal form surrogates for fast oscillatory activities. However, the parameters'

quantitative interpretability would be compromised in those regimes, and predicted behaviours may be also debatable.

In addition to the results shown here we investigated single conductance-based self-connected inhibitory populations with tonic inputs, which we found can generate arbitrarily high frequency spectral peaks if the self-inhibition and exogenous input strengths are sufficiently high (not shown). The fast oscillations are nonetheless heavily damped and our general conclusions stand.

Contrasting to the results from neural mass models, spiking neural network models can easily achieve fast oscillations (Wang, 2010) . Examples of such networks can be found in, e.g., (Brunel, 2000; Brunel and Hakim, 1999; Suffczynski et al., 2014) where model systems with synaptically coupled excitatory pyramidal cells and fast-spiking interneurons can generate high-gamma frequencies (e.g 60-200Hz (Suffczynski et al., 2014))

2.3.2 Implications for future work

In summary, to model fast oscillatory dynamics, it may be necessary to consider conductance-based models that have more realistic synaptic mechanisms mediating explicit spiking and refractoriness. These considerations motivate the development of full population density models with refractoriness (Gerstner, 2000;Knight, 2000;Mattia and Del Giudice, 2002;Kovacic et al., 2009) for the study of fast oscillatory neural population activity and their comparison with the neural mass limit. In the next chapters we develop such models in the context of Dynamic Causal Modelling. This is an important step towards the development of a biophysically principled connectivity framework applicable to, e.g., neocortical focal epileptic seizure fast oscillatory onsets (Lemieux et al., 2011).

3 FOKKER-PLANCK POPULATION MODELS OF INTEGRATE AND FIRE NEURONS[1]

In this chapter, we describe a class of mean-field Fokker-Planck (FP) population models of conductance based leaky integrate-and-fire (LIF) neurons, for characterising the mechanisms of fast oscillatory activity generated by coupled neural populations. We explore plausible population architectures, and parameter ranges garnered from public databases. We first demonstrate how this class of models can produce a range of behaviours that can be related directly to neurobiological states, particularly gamma oscillations. We then propose a generic and efficient numerical approach for solving (integrating) the model equations, and address the prediction of voltage-clamp currents and spiking statistics of single-cell recordings. We anticipate that the proposed modelling approach, combined with the inversion scheme that will be presented in chapter 4, may be useful in characterising specific aspects of neural circuits, at a level previously unattainable, based on electrophysiological measurements.

[1] This chapter is the subject of an article entitled "Fokker-Planck population models of integrate and fire neurons for gamma oscillation investigations" submitted to PlosOne

3.1 Introduction

In the following sections, we bring together some aspects of mean-field FP models considered in previous works and investigate more thoroughly the dynamical repertoire that these models possess when several populations are coupled together, while considering variables that can be inferred experimentally. In particular, we are interested in bringing together, in a single framework, results that are traditionally more associated with lumped models, such as alpha and beta rhythms (e.g. (Grimbert and Faugeras, 2006; Moran et al., 2007)), with results more commonly addressed with network models, such as faster gamma rhythms (e.g. (Brunel and Hakim, 2008; Tiesinga et al., 2001)).

We build on a family of models that bridge two distinct levels of neuronal complexity: the single neuron and the interactions of coupled neuronal populations. A primary methodological goal of our enterprise is to provide means of better interpreting the measurements made at the single-neuron level, while taking into account their interactions with populations of other neurons (e.g. *in vitro* slice preparations, or *in vivo* single unit measurements). The principal scientific aim of our work is to better understand the mechanisms that give rise to gamma-range oscillatory activity.

Our ultimate objective is to fit such models in the dynamic causal modelling framework (Friston et al., 2007, 2003), which calls on a Bayesian model inversion methodology. We are therefore interested in computationally efficient models that are suitable for inversion. We will consequently place an emphasis on the economy of state variables necessary to describe the single neuron and enable mean-field interactions between populations. Therefore, we follow (Brunel, 2000; Harrison et al., 2005; Kovacic et al., 2009; Marpeau et al., 2009; Mattia and Giudice, 2002) who investigated mean-field models of different flavours of the one-dimensional leaky-integrate-and-fire (LIF) neurons. We considered this sort of model sufficient to provide a basic description of the phenomena we propose to address. Specifically, we will use a conductance based LIF neuron similar to that used in (Kovacic et al., 2009). We include the neuronal firing refractoriness described in (Harrison et al., 2005), but absent in (Kovacic et al., 2009; Marpeau et al., 2009; Mattia and Giudice, 2002). Crucially, we implement this using one-dimensional (single state) neuron models, as in (Kovacic et al., 2009; Marpeau et al., 2009; Mattia and Giudice, 2002); treating boundary conditions (i.e. spiking and

refractoriness) explicitly, as opposed to using multiple state variables, as in (Harrison et al., 2005).

We present a numerical analysis of the dynamical response of the model expanding the single population results of (Harrison et al., 2005; Marpeau et al., 2009; Mattia and Giudice, 2002), and offering a novel solution to tackle the problem of integrating the full nonlinear FP equation of coupled neural populations. To accomplish this, we have adapted an exponential integration numerical scheme (Hochbruck and Ostermann, 2010) that copes with the stiffness and fast oscillatory modes of the ensuing differential equations (Mattia and Giudice, 2002).

3.2 Methods

In the following, we formulate a population model for conductance-based LIF neurons, starting with a description of individual neurons, their behaviour as populations and the interactions between populations. We then address the computation of measurable quantities, such as cell voltage-clamped currents, local field potentials (LFPs) and inter-spike intervals (ISIs). We also describe the numerical algorithms used for the integration of the proposed model equations, with a particular emphasis on the adaptation of an exponential type integration method to the equations specificities. Finally, we present the general architecture of the neural systems that are explored with simulations.

3.2.1 Fokker-Planck population model for LIF neurons

In this section, we present the equations describing the single-neuron model used in this work and how it interacts with other neurons in a mean-field setting.

3.2.1.1 Leaky integrate-and-fire neurons

We define the behaviour of the conductance-based LIF neuron using the following stochastic differential equation:

$$dV = \frac{1}{C}\left(g_L \cdot (V_L - V) + I(V,t)\right) dt + \sigma dW, \qquad V \in]-\infty, V_{th}] \tag{3.1}$$

with the boundary rule:

$$if\ V(t) = V_{th};\ set\ V(t + T_r) = V_r$$

Here V is the membrane potential, C the cell membrane capacitance, g_L its leakage conductance, V_L the resting potential, $I(V,t)$ is an input current, and σ is the volatility of the stochastic process. V_{tr} is the firing threshold, T_r is the firing refractory time, and V_r the resetting potential.

Under a mean-field approximation, the input function $I(V,t)$ is equal for all neurons of a given population, and the differences among constituent neurons are embodied in the term σdW (or in the initial conditions of the problem). We model input currents in terms of changes in synaptic conductances as follows:

$$I(V,t) = \sum_k g_k(t) \cdot (V_k - V)$$

$$dg_k = \frac{1}{T_k}(S_k(t - \tau_k) - g_k)dt \tag{3.2}$$

$$k = AMPA, GABA, \dots$$

where $g_k(t)$ are the channel conductances over time, V_k are the channel reversal potentials, T_k are the channel inactivation time constants, and $S_k(t - \tau_k)$ are the collective synaptic inputs from other populations, with a delay τ_k. In this work, we limit k to two types of channels: inhibitory GABAergic channels and excitatory AMPA type receptors; however, the channel types can easily be extended to model an arbitrary number of receptor types.

3.2.1.2 Population dynamics and the Fokker-Planck equation

To describe the time evolution of the probability density function, $p(x,t)$, of an ensemble of random variables, x ,whose behaviour is determined by the stochastic differential equation $dx = \mathrm{D}^{(1)}(x,t,p,u)dt + \sqrt{2 \cdot \mathrm{D}^{(2)}(x,t,p,u)}dW$, we introduce the one-dimensional nonlinear FP equation (Risken, 1989):

$$\frac{\partial}{\partial t}p(x,t) = L_{FP}\ p(x,t) = \left(-\frac{\partial}{\partial x}\mathrm{D}^{(1)}(x,t,p,u) + \frac{\partial^2}{\partial x^2}\mathrm{D}^{(2)}(x,t,p,u)\right)p(x,t) \tag{3.3}$$

where L_{FP} is the FP operator and u is an input function (note: the differential operators act also outside the brackets).

We also define the probability current S as:

$$S(x,t) = \left(\mathrm{D}^{(1)}(x,t,p,u) - \frac{\partial}{\partial x} \mathrm{D}^{(2)}(x,t,p,u) \right) p(x,t) \tag{3.4}$$

so that

$$L_{FP}\, p(x,t) = -\frac{\partial S(x,t)}{\partial x}$$

Here, we have introduced the drift, $\mathrm{D}^{(1)}$, and diffusion, $\mathrm{D}^{(2)}$, functions, which in the case of the LIF population are given by:

$$\begin{cases} \mathrm{D}^{(1)}(x,t,p,u) = \dfrac{1}{C}\left(g_L \cdot (V_L - x) + I(x,p,u,t)\right) \\ \mathrm{D}^{(2)}(x,t,p,u) = \frac{1}{2}\sigma^2 \end{cases}, \qquad if \;\; x \in \,]-\infty, V_{th}[\,\backslash V_r \tag{3.5}$$

$$\begin{cases} \mathrm{D}^{(1)}(x,t,p,u) = l/T_r \\ \mathrm{D}^{(2)}(x,t,p,u) = 0 \end{cases}, \qquad if \;\; x \in \,]V_{th}, V_{th} + l[$$

In the above, we have divided the 1-dimensional parameter space (spanned by x) into two parts: one representing the sub-threshold membrane voltage fluctuations ($]-\infty, V_{th}[$), and the other representing the refractory time period before the neurons reset ($]V_{th}, V_{th} + l[$) (c.f. **Figure 3.1**). Note that the current input function, $I(x,p,u,t)$, not only depends on voltage, here represented by the variable x, and time, as previously made explicit in equation (3.5), but also possibly depends on the firing rate of the population p and the external inputs u. The definition of $\mathrm{D}^{(1)}$ on the queue region follows from imposing that the neuron should travel the distance l (from V_{th} to $V_{th} + l$) in the refractory time T_r, hence the drift speed $\mathrm{D}^{(1)} = l/T_r$.

This allows us to specify the following boundary conditions:

$$S(x)\big|_{-\infty} = 0 \tag{3.6a}$$

$$p(x)|_{V_r^+} - p(x)|_{V_r^-} = 0 \tag{3.6b}$$

$$S(x)|_{V_r^+} - S(x)|_{V_r^-} = S(x)|_{V_{th}+l} \tag{3.6c}$$

$$p(x)|_{V_{th}^-} = 0 \tag{3.6d}$$

$$S(x)|_{V_{th}^-} = S(x)|_{V_{th}^+} \tag{3.6e}$$

where, for notational convenience, we use $f(x)|_a = \lim_{x \to a} f(x)$. Condition (3.6a) is a so-called natural boundary condition at $-\infty$; it represents a reflecting wall at $-\infty$, so that no probability flux is gained or lost; condition (3.6b) is a continuity condition on the probability density function at the resetting potential; condition (3.6c) ensures the conservation of probability density – replenishing the neurons, after waiting T_r, back into voltage space; condition (3.6d) represents an absorbing barrier at V_{th}, such that a neuron that crosses V_{th} cannot return; and condition (3.6e) ensures flux conservation condition at V_{th}.

Finally, the integral of p over its domain, being a probability density function, must be equal to 1:

$$\int_{-\infty}^{V_{th}+L} p(x,t)dx = 1 \tag{3.7}$$

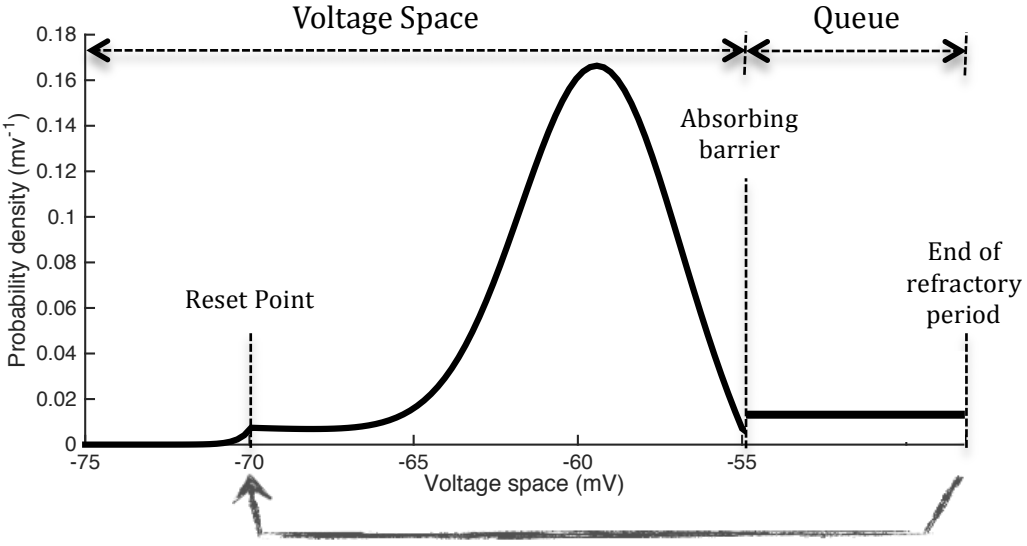

Figure 3.1 – Schematic representation of the probability sample space and a stationary probability density function of a population of LIF neurons. The sample space is divided into two regions: a "voltage space", where neurons follow standard sub-threshold dynamics, and a "queue" implementing the refractory period after neuronal spiking, after which neurons are reintroduced in the "voltage space" at the reset point.

3.2.1.3 Coupling of neuronal populations

We assume that neuronal populations only communicate through their firing rates, and that these influence the input current function in the postsynaptic population as described in equation (3.2). The population firing rate is a deterministic quantity and is given by the flux S at each population's firing threshold; note that it may vary quickly, in transient perturbations of individual populations. However, given that the firing rates are synaptically filtered in equation (3.2), the coupled population FP equation drift terms,$D^{(1)}$, vary relatively slowly. By combining the state space of equation (3.5) with the states of the postsynaptic conductances that each population exerts through its efferent connections, we obtain the following equation for the input current function for each population, i (note that equation (3.2) is linear, and therefore we can apply the different connectivity strengths after its integration; as a result one can integrate g_i with the FP operator of the presynaptic population):

$$I_i(V,t) = \sum_j \sum_k (\Gamma_{i,j,k} g_{j,k}(t) + C_{i,k} u_{i,k}) \cdot (V_k - V) \tag{3.8}$$

where $\Gamma_{i,j,k}$ is the connectivity matrices from population j to i for channel type k and $C_{i,k}u_{i,k}$ represent exogenous inputs to the k channels of population i.

3.2.1.4 Estimation of individual neuron dynamics

The trajectory of the neuronal state of single neurons can be recovered from the FP equation; in general (Frank, 2005):

$$\frac{\partial p(x,t|x',t')}{\partial t} = \left(-\frac{\partial}{\partial x} \mathrm{D}^{(1)}(x,t,p(x,t),u) + \frac{\partial^2}{\partial x^2} \mathrm{D}^{(2)}(x,t,p(x,t),u) \right) p(x,t|x',t') \tag{3.9}$$

Note that $\mathrm{D}^{(1)}$ and $\mathrm{D}^{(2)}$ depend only on the solution of the FP equation, $p(x,t)$, and not on the conditional probability densities $p(x,t|x',t')$.

3.2.1.5 Inter-spike interval distribution

To determine the ISI distribution over an interval T, we must compute the following integral:

$$ISI(\Delta t) \propto \int_T p(V_{th}^+, t' + \Delta t | V_r, t' + T_r) p(V_{th}^+, t') dt' \tag{3.10}$$

The term inside the integral is proportional to the probability of a spike being fired after time interval Δt, given that the neuron has produced a spike at time t', multiplied by the probability of firing a spike at time t' in the first place (in order to obtain an ISI probability density per unit time, we evaluate the integral in terms of the corresponding probability fluxes $S(x)$). Under periodic oscillatory conditions, the integral can be limited to a period of the oscillation of the system (or a point evaluation if the system is at a fixed point):

$$ISI(\Delta t) \propto \int_0^{2\pi} p\left(V_{th}^+, \frac{\varphi}{\omega} + \Delta t | V_r, \frac{\varphi}{\omega} + T_r\right) p\left(V_{th}^+, \frac{\varphi}{\omega}\right) d\varphi \tag{3.11}$$

Here, we set the origin of time to the zero of the phase, φ, of the oscillation of frequency ω. This can be computed using equation (3.9) based on the solution of the non-linear FP equation (note that in order to recover ISIs, we have to remove the reset condition from the FP equation, because we are only interested in the timing between consecutive spikes).

3.2.1.6 Predictions of voltage-clamp currents and LFPs

Following the solution of the non-linear FP equation it is straightforward to compute the currents a neuron of population i would experience if clamped at a certain voltage V_{hold}, by evaluating the input current equation (3.8) at that voltage: $I_i(V_{hold}, t)$. A simplistic model of the currents that generate LFPs can be computed by averaging the input currents over the population:

$$I_i^{LFP}(t) = \int p_i(V,t) I_i(V,t)\ dV \tag{3.12}$$

This is a simplistic LFP model and, due to the point nature of the LIF neuron, eschews all the geometric complexities that more accurate LFP models may incorporate (e.g. (Einevoll, 2014)). Heuristically we follow the classical assumption that the inputs to pyramidal cell populations are the main generators of LFPs (e.g.(B H Jansen and Rit, 1995)), and only use these LFP estimates as illustrative quantities.

This concludes our mathematical description of the mean-field model, and how this description furnishes predictions of various electrophysiological measures in terms expectations over the probability density of (hidden) neuronal states.

Summarising the differential equations introduced so far: we have partial differential equations (PDEs) describing the time evolution of the probability densities of the neurons in one or more populations. These populations are coupled by the postsynaptic conductances that are described by ordinary differential equations (ODEs), which in turn depend on the population probability densities.

3.2.2 Numerical integration for the non-linear Fokker-Planck equations

We now turn to the practical issue of solving these equations, for any given set of parameters, to examine the emergent behaviour – or, in the context of dynamic causal modelling, generate predictions of empirical data. We use a finite difference scheme to

discretise the voltage space in the PDEs and keep the time variable continuous. This results in a large system of coupled ODEs, which have some special characteristics that can be exploited for computational efficiency.

Each FP equation (3.3) can be rewritten as:

$$\begin{aligned} \dot{p}_i &= L_{FP}(\boldsymbol{\Gamma} \cdot \boldsymbol{g}, \boldsymbol{C} \cdot \boldsymbol{u}) \cdot p_i \\ \dot{g}_i &= -T^{-1} g_i + T^{-1} s(p_i) \end{aligned} \tag{3.13}$$

where p_i is a vector representing the neuron probability density over the discretised voltage space; $L_{FP}(\boldsymbol{\Gamma} \cdot \boldsymbol{g}, \boldsymbol{C} \cdot \boldsymbol{u})$ is the matrix approximating the FP operator via finite differences (c.f. Marpeau for a detailed treatment of the discretisation of the FP operator (Marpeau et al., 2009)); $\boldsymbol{\Gamma}, \boldsymbol{g}, \boldsymbol{C}$ and $\boldsymbol{u}$ represent the collection of all connectivity matrices, efferent conductances and exogenous inputs for all channels and populations; the g_i vectors represent the conductances over all ion channels that the population i elicits; T are diagonal matrices that encode the time constants of each channel type; and $s(p_i)$ is the flux across the firing barrier of the population (approximated via finite differences). Note that $s(p_i)$ is a linear function of p_i (discretised from equation (3.4)), so we can group p_i and g_i from all populations together in $\hat{\boldsymbol{p}}$ and re-write (3.13) as:

$$\dot{\hat{\boldsymbol{p}}} = L(\boldsymbol{\Gamma} \cdot \boldsymbol{g}, \boldsymbol{C} \cdot \boldsymbol{u}) \cdot \hat{\boldsymbol{p}} \tag{3.14}$$

It has been observed that some components in $\hat{\boldsymbol{p}}$ can show very fast oscillatory behaviors over time (Mattia and Giudice, 2002), but $\boldsymbol{g}$ and $\boldsymbol{u}$ usually vary slowly due to the synaptic temporal filtering. This separation of temporal scales renders equation (3.14) almost linear at the fast temporal scales of $\hat{\boldsymbol{p}}$, motivating the use of exponential integrators to solve the equation over relatively large time steps (Chu and Berman, 1974; Hochbruck and Ostermann, 2010; Pope, 1963). However, an important drawback of exponential integrators is that the exponentiation of large matrices can become computationally very costly ($O(N^3)$ if implemented naively (Moler and Van Loan, 2003)), and therefore we opt for a slight adaptation that enables the matrices to be exponentiated in block-diagonal form. First, we re-write equation (3.14) as:

$$\dot{\hat{\boldsymbol{p}}}(t) = L_0 \cdot \hat{\boldsymbol{p}}(t) + (L(\boldsymbol{\Gamma} \cdot \boldsymbol{g}(t), \boldsymbol{C} \cdot \boldsymbol{u}(t)) - L_0) \cdot \hat{\boldsymbol{p}}(t) \tag{3.15}$$

which is equivalent to the integral equation:

$$\widehat{\boldsymbol{p}}(t) = e^{tL_0} \cdot \widehat{\boldsymbol{p}}(0) + \int_0^t e^{(t-\tau)L_0} (L(\boldsymbol{\Gamma} \cdot \boldsymbol{g}(\tau), \boldsymbol{C} \cdot \boldsymbol{u}(\tau)) - L_0) \cdot \widehat{\boldsymbol{p}}(\tau)\, d\tau \tag{3.16}$$

Second, using a forward Euler time discretisation, we hold $(L\,(\boldsymbol{\Gamma} \cdot \boldsymbol{g}(\tau), \boldsymbol{C} \cdot \boldsymbol{u}(\tau)) - L_0) \approx \; (L\,(\boldsymbol{\Gamma} \cdot \boldsymbol{g}(0), \boldsymbol{C} \cdot \boldsymbol{u}(0)) - L_0)$ constant for the whole interval. Choosing $L_0 = L\,(\boldsymbol{\Gamma} \cdot \boldsymbol{g}(0), \boldsymbol{C} \cdot \boldsymbol{u}(0))$ renders the integral null, with the added advantage that L_0 is block-diagonal. By adding a midpoint adaptation, the full numerical scheme is:

$$\begin{aligned} \widetilde{\widehat{\boldsymbol{p}}}(t_{i+1}) &= \; e^{\Delta t/2 \cdot L\,(\boldsymbol{\Gamma} \cdot \boldsymbol{g}(t_i), \boldsymbol{C} \cdot \boldsymbol{u}(t_i))} \cdot \widehat{\boldsymbol{p}}(t_i) \\ \widehat{\boldsymbol{p}}(t_{i+1}) &= \; e^{\Delta t \cdot L\left(\boldsymbol{\Gamma} \cdot \widetilde{\boldsymbol{g}}(t_{i+1}), \boldsymbol{C} \cdot \boldsymbol{u}(t_i + \Delta t/2)\right)} \cdot \widehat{\boldsymbol{p}}(t_i) \end{aligned} \tag{3.17}$$

where $\widetilde{\boldsymbol{g}}(t_{i+1})$ is extracted from the midpoint approximation $\widetilde{\widehat{\boldsymbol{p}}}(t_{i+1})$. Additionally, we control the numerical errors by adjusting the time step size ensuring the following condition:

$$\left\| \widehat{\boldsymbol{p}}(t_{i+1}) - \; e^{\Delta t/2 \cdot L\,(\boldsymbol{\Gamma} \cdot \boldsymbol{g}(t_i), \boldsymbol{C} \cdot \boldsymbol{u}(t_i))} \cdot \widetilde{\widehat{\boldsymbol{p}}}(t_{i+1}) \right\| < numerical\ tolerance \tag{3.18}$$

Note that our scheme does not require the inversion of L which is singular (by construction of the FP operators (Mattia and Giudice, 2002)), thereby avoiding a problem in many currently available exponential integrators.

3.2.3 Simulations and Numerical Tests

To illustrate the behavioural repertoire of the models considered in this chapter, we performed a number of simulations using an excitatory ("E") and an inhibitory ("I") population that are coupled together - "E-I" model. We used, whenever available, parameters based on CA1 pyramidal cells and parvalbumin positive inhibitory interneurons on the NeuroElectro database (www.neuroelectro.org) (Tripathy et al., 2015) (see Table 3.1). One can reproduce a range of behaviours by varying the synaptic coupling strengths and external driving inputs. We also coupled five of these excitatory – inhibitory pairs (making a total of ten populations) to illustrate the scaling of the numerical scheme presented here. The connection strengths we used are shown in Table 3.2.

Table 3.1 - Cell parameters for the two modelled populations

Parameter	Inhibitory interneurons	Pyramidal cells
Capacitance*, C	84 pF	150 pF
Leak reversal potential*, V_L	-62 mV	-65 mV
Leak conductance*, g_L	84/12 nS (pF/ms)	150/30 nS (pF/ms)
Threshold voltage*, V_{th}	-55 mV	-48 mV
Refractory time*, T_r	1 ms	8 ms
Reset voltage, V_r	-70 mV	-70 mV
AMPA reversal potential, V_{AMPA}	0 mV	0 mV
AMPA time constant, T_{AMPA}	16 ms	16 ms
GABA reversal potential, V_{GABA}	-70 mV	-70 mV
GABA time constant, T_{GABA}	5 ms	5 ms
Diffusion term, $\frac{1}{2}\sigma^2$	2000 mV^2/s	1000 mV^2/s
Efferent conduction delay	1 ms	1 ms

* Values adapted from www.neuroelectro.org for CA1 neurons.

Table 3.2 - Connection parameters for each model

Model	Excitatory External Input	Inhibitory connections	Excitatory connection
E - I	$\begin{bmatrix}0.1\\3\end{bmatrix}$ (nS)	$\begin{bmatrix}0.001 & 0\\1 & 0\end{bmatrix}$ (nS neuron^{-1} s)	$\begin{bmatrix}0 & 0.25\\0 & 0.001\end{bmatrix}$ (nS neuron^{-1} s)
I - I	$\begin{bmatrix}4\\4\end{bmatrix}$ (nS)	$\begin{bmatrix}1 & 0\\0.5 & 0\end{bmatrix}$ (nS neuron^{-1} s)	$\begin{bmatrix}0 & 0.01\\0 & 0.0005\end{bmatrix}$ (nS neuron^{-1} s)
CFC	$\begin{bmatrix}0.1\\2\end{bmatrix}$ (nS)	$\begin{bmatrix}0.01 & 0\\0.5 & 0\end{bmatrix}$ (nS neuron^{-1} s)	$\begin{bmatrix}0 & 2\\0 & 0.5\end{bmatrix}$ (nS neuron^{-1} s)
Chaotic	$\begin{bmatrix}0.1\\8\end{bmatrix}$ (nS)	$\begin{bmatrix}0.5 & 0\\1 & 0\end{bmatrix}$ (nS neuron^{-1} s)	$\begin{bmatrix}0 & 2\\0 & 0.15\end{bmatrix}$ (nS neuron^{-1} s)
Chain	$\begin{bmatrix}0\\0\\0\\0\\0\\2\\1\\1\\1\\1\end{bmatrix}$ (nS)	$\begin{bmatrix} & \bar{0}_{5\times5} & & & & \bar{0}_{5\times5}\\ 0.5 & 0.5 & 0.25 & 0 & 0 & \\ 0.5 & 0.5 & 0.5 & 0.25 & 0 & \\ 0.25 & 0.5 & 0.5 & 0.5 & 0.25 & \bar{0}_{5\times5}\\ 0 & 0.25 & 0.5 & 0.5 & 0.5 & \\ 0 & 0 & 0.25 & 0.5 & 0.5 & \end{bmatrix}$ (nS neuron^{-1} s)	$\begin{bmatrix} & 0.25 & 0 & 0 & 0 & 0\\ & 0 & 0.25 & 0 & 0 & 0\\ \bar{0}_{5\times5} & 0 & 0 & 0.25 & 0 & 0\\ & 0 & 0 & 0 & 0.25 & 0\\ & 0 & 0 & 0 & 0 & 0.25\\ & 0.25 & 0.25 & 0 & 0 & 0\\ & 0.25 & 0.25 & 0.25 & 0 & 0\\ \bar{0}_{5\times5} & 0 & 0.25 & 0.25 & 0.25 & 0\\ & 0 & 0 & 0.25 & 0.25 & 0.25\\ & 0 & 0 & 0 & 0.25 & 0.25\end{bmatrix}$ (nS neuron^{-1} s)

All numerical methods were implemented in MATLAB (ver. 8.4.0.150421 [R2014b]) and are available online at https://github.com/mfpleite/NeuralPop. The exponential integrator was benchmarked against both *ode45*, the default solver in the MATLAB suite, and *ode15s*, designed for stiff problems, both available in the standard MATLAB package. An initial rough solution was computed with the exponential integrator in order to find the stationary behaviour of each system. The timing and numerical precision of the integrators was subsequently analysed for the computation of a full cycle of an oscillation, using each method. The proxy for the true solution was taken to be the integration with a tolerance of 10^{-12} with each method. The numerical error was calculated as the norm of the difference of the solutions at the end of the integration interval.

3.3 Results and discussion

We start by illustrating "E-I" oscillatory behaviour; this is achieved by allowing strong connection strengths between an excitatory and inhibitory population (see Table 3.2). Self-sustained oscillations in the high beta range of the spectrum (~23 Hz) emerge (**Figure 3.2**). This is in line with the lower frequency limit of more phenomenological models of gamma like oscillations based on Wilson and Cowen type of lumped modes (e.g. 24~80 Hz in (Akam et al., 2012)). However, our model allows us to make specific predictions about a wider array of empirical measurements. In **Figure 3.2** we showcase the predictions of an LFP current generated by the excitatory population, cell voltage-clamp currents for a neuron in the excitatory population, and ISIs for neurons of both populations. For illustrative purposes, we also show the probability densities of the neurons over time for both populations, although these would not be directly easily observable. A schematic representation of the system is also presented.

Key features of gamma like oscillations in hippocampal slice preparations (Akam et al., 2012; Hájos et al., 2004) are qualitatively well characterized by the simulations, including: excitatory currents anticipating inhibitory currents as reflected by the counter-clockwise trajectory in **Figure 3.2**, panel (B) and sparse pyramidal cell firing, with concomitant close to every-cycle firing of inhibitory interneurons. We now take this model as the basis for an exploration of different connection properties.

If the excitatory connection from the "E" to the "I" population is decreased and the self inhibition of the "I" population is increased, along with the steady exogenous excitatory input to "I", fast high gamma oscillations are generated as shown in **Figure 3.3**. This replicates well-established findings based on network and population modelling (e.g. (Brunel and Wang, 2003)). It is interesting to note that our model predicts very different features for measurable data above and beyond the obvious increase in frequency. These include: a clockwise trajectory of the inhibitory currents plotted against the excitatory currents; and highly phase-coupled firing of the inhibitory cells, as shown in the discrete intervals for the ISI distribution, versus a less phase-coupled firing of the excitatory population. It should be noted that, in this case, the inhibitory cells do not fire in many cycles of the oscillations (as can be observed by the heavy tail of the ISI distribution, for example).

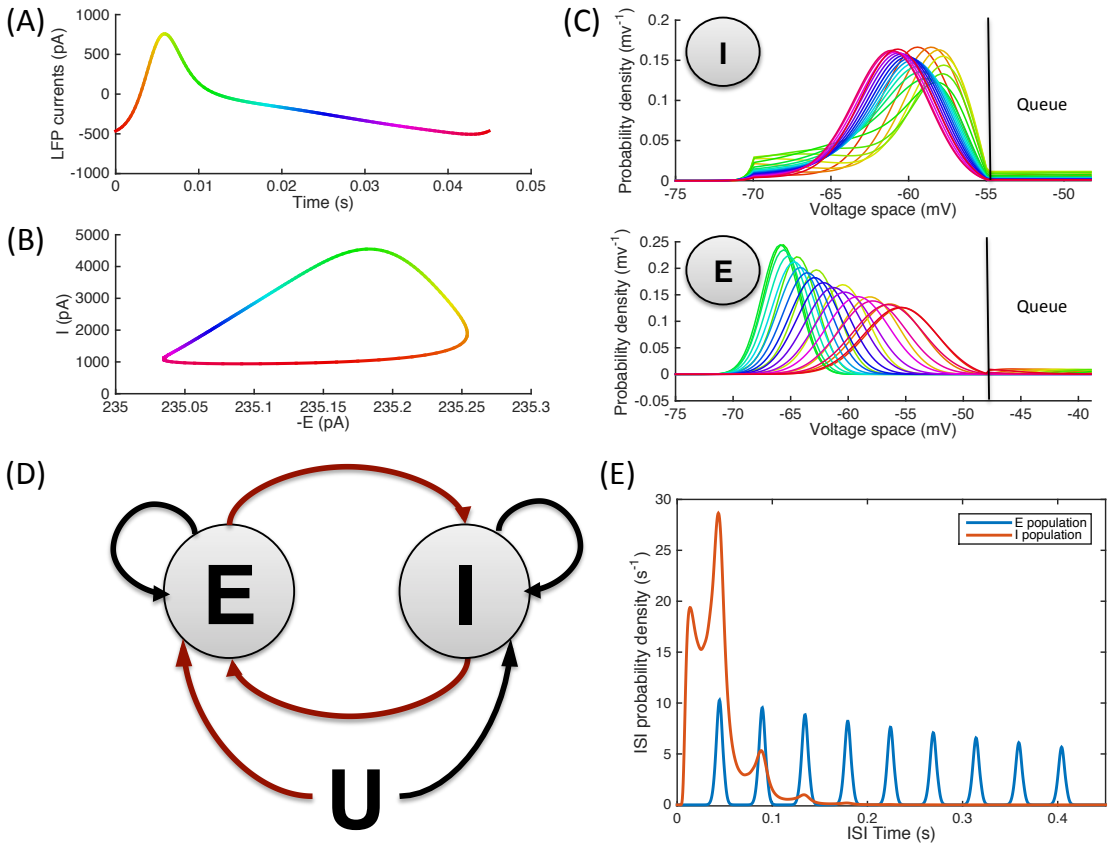

Figure 3.2 - Illustration of a ~23 Hz "E-I" type oscillation: (A) LFP waveform along an oscillation cycle. Time is colour coded in parts (A)-(C). (B) Cell clamp currents for the excitatory population: inhibitory currents (cell clamped at 0 mV) plotted against excitatory currents (cell clamped at -70 mV), time colour code indicates a counter clockwise orientation of the cycle. (C) Neuron probability densities over voltage/queue space for the two populations. (D) Schematic representation of the system simulated: red arrows indicate strong connections, black arrows indicate weak connections. (E) Inter-spike interval probability density distribution: the inhibitory population spikes almost every oscillation cycle (~40 ms), sometimes twice, while the excitatory population spikes more sparsely, but strongly phase coupled with the oscillation.

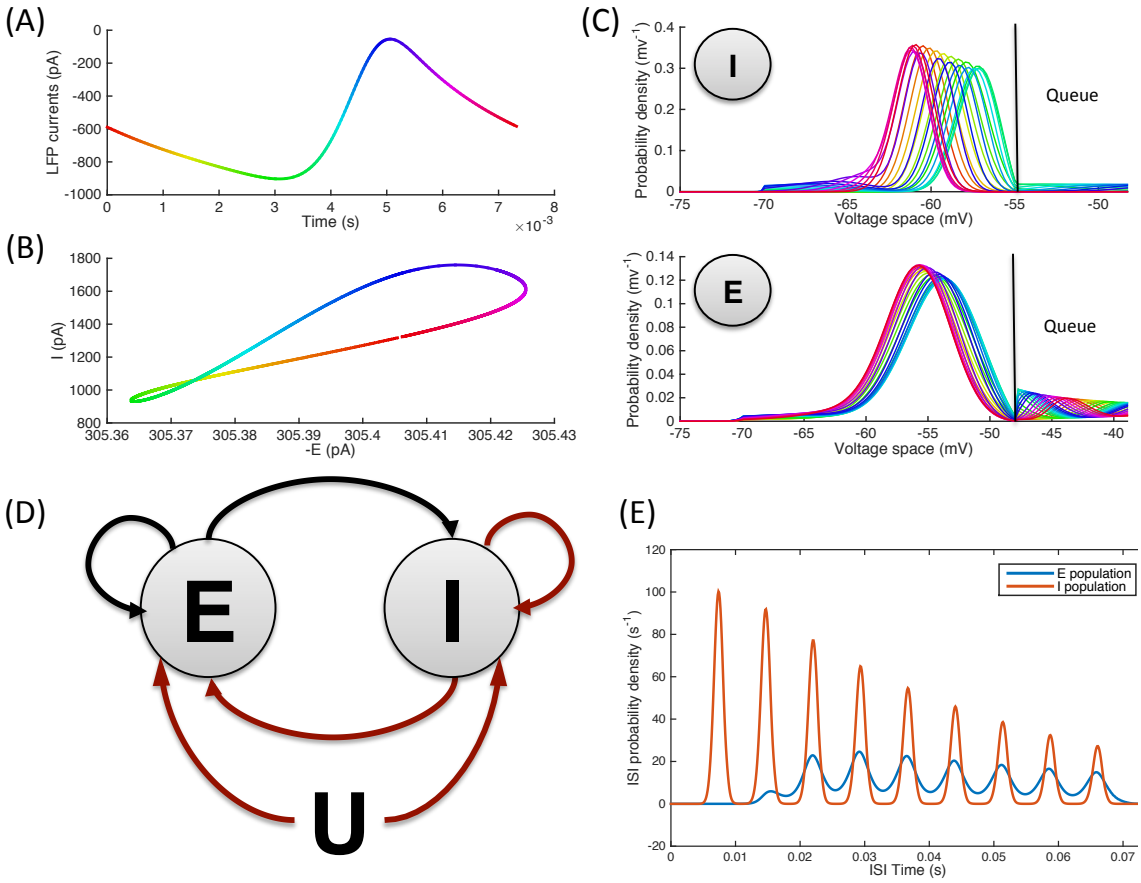

Figure 3.3 - Illustration of a ~130 Hz "I-I" type oscillation: (A) LFP waveform along an oscillation cycle. Time is colour coded in parts (A)-(C). (B) Cell clamp currents for the excitatory population: inhibitory currents (cell clamped at 0 mV) plotted against excitatory currents (cell clamped at -70 mV), time colour code indicates a predominantly clockwise orientation of the cycle (C) Neuron probability densities over voltage/queue space for the two populations. (D) Schematic representation of the system simulated: red arrows represent strong connections, black arrows represent weak connections. (E) Inter-spike interval probability density distribution: both populations fire sparsely within the oscillation, the inhibitory firing rate is in this case more phase coupled to the ongoing oscillation than that of the excitatory population.

Another possible mechanism for generating fast oscillations is the synchronous bursting of populations of neurons (e.g. (Tiesinga et al., 2001)). We induce such behaviour in the "E-I" model by increasing the phasic excitation to the "I" population from the "E" population, and the self-connections of the "E" population, such that these balance the increased inhibition due to increased "I" population firing rates. As illustrated in **Figure 3.4** this scenario generates a fast oscillation in the frequency range of the firing rates of

the individual inhibitory cells, ~175 Hz, that is phase-coupled with the excitatory peak of a lower frequency oscillation, ~24 Hz, dominated by the "E-I" mechanism. The "E" population here fires very sparsely, while the inhibitory neurons fire several times per oscillation cycle of the lower frequency.

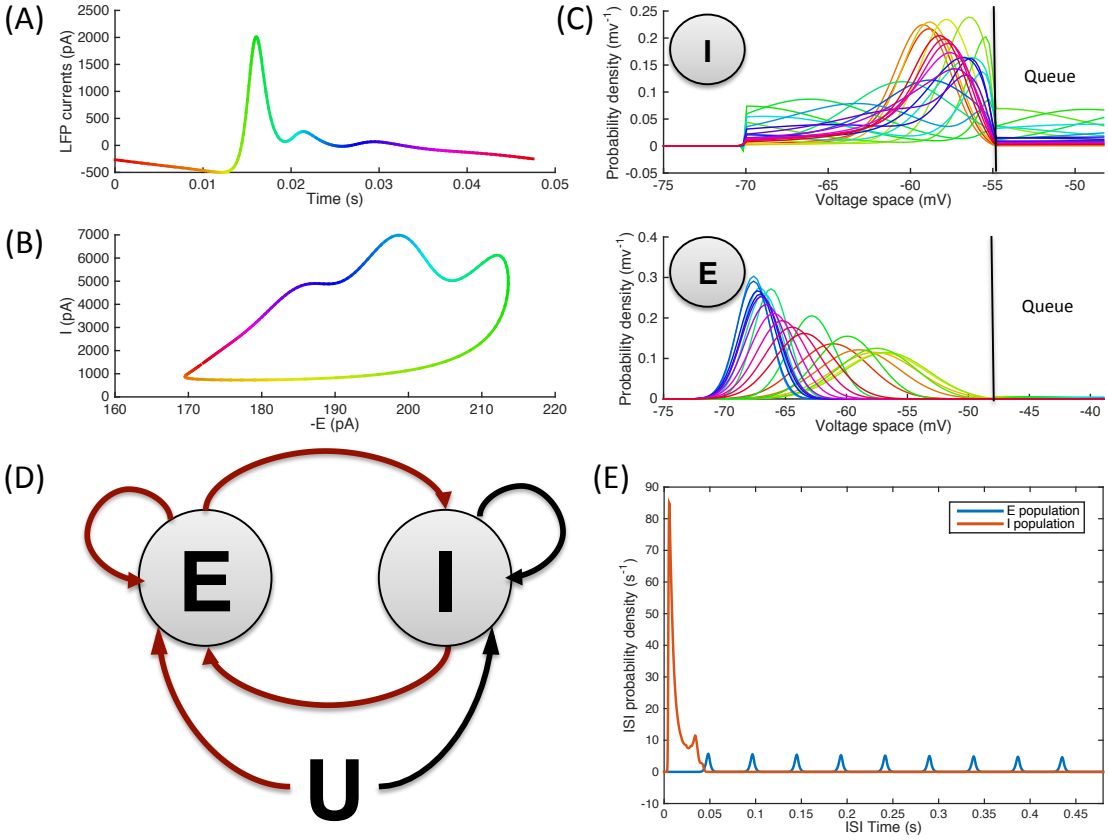

Figure 3.4 - Illustration of a ~24 Hz cycle displaying a cross-frequency coupling with a lower amplitude faster ~175 Hz oscillation: (A) LFP waveform along an oscillation cycle. Time is colour coded in parts (A)-(C). (B) Cell clamp currents for the excitatory population: inhibitory currents (cell clamped at 0 mV) plotted against excitatory currents (cell clamped at -70 mV), time colour code indicates a counter-clockwise orientation of the cycle (C) Neuron probability densities over voltage/queue space for the two populations. (D) Schematic representation of the system simulated: red arrows represent strong connections, black arrows represent weak connections. (E) Inter-spike interval probability density distribution: the excitatory population fires sparsely and highly phase coupled slower oscillation, the inhibitory firing rates are higher and firing occurs multiple times per oscillation cycle. The inhibitory population ISI statistical mode of ~5.5 ms is reciprocal of the faster oscillation frequency of ~175 Hz.

A chaotic behaviour is observed if the connections are set such that both "I-I" and "E-I" coupling co-exist strongly (**Figure 3.5**). In this scenario, "I-I" oscillations occur and interact non-trivially with the slower "E-I" oscillations. The "E" population fires sparsely, contrasting with high 'I' population firing rates. Note however that the ISIs here were computed only for the simulation period ~1 s, and do not portray an asymptotically periodic solution as in the previous examples. Also, note that the regions of phase space explored by the system and portrayed by the neural probability distributions and voltage clamped currents (proportional to the conductance terms) is considerably more complicated than in the previous examples. We note that chaotic behaviour is common in delay differential equations (e.g. (Sprott, 2007)), which are here implicitly included in the queue structure of the nonlinear FP equations. A formal exploration of the chaotic properties of this system falls beyond the scope of the present work – we simply acknowledge the existence of non-stationary and non-periodic deterministic solutions that can be found in this mean-field formulation.

Finally, we simulate a chain of "E-I" nodes coupled through lateral connections between the excitatory nodes and between the inhibitory nodes. The parameters chosen for this system yield a similar dynamical behaviour to that of the single "E-I" system. The purpose here is to illustrate the scalability of the models presented here and, in particular, how the exponential integration scheme can cope with high-dimensional systems.

In **Figure 3.6** we present the results of the comparison of the new numerical scheme's performance in relation to standard solvers, for the systems that yield periodic oscillatory behaviours. As expected, *ode15s* consistently outperforms *ode45*. The new exponential integrator outperforms *ode15s* in two situations: 1) relatively crude error tolerances, due to the particularly stable properties of exponential integrators (Chu and Berman, 1974; Hochbruck and Ostermann, 2010; Pope, 1963) and 2) large systems of coupled populations, due to the new method's computational complexity being linear in the number of populations.

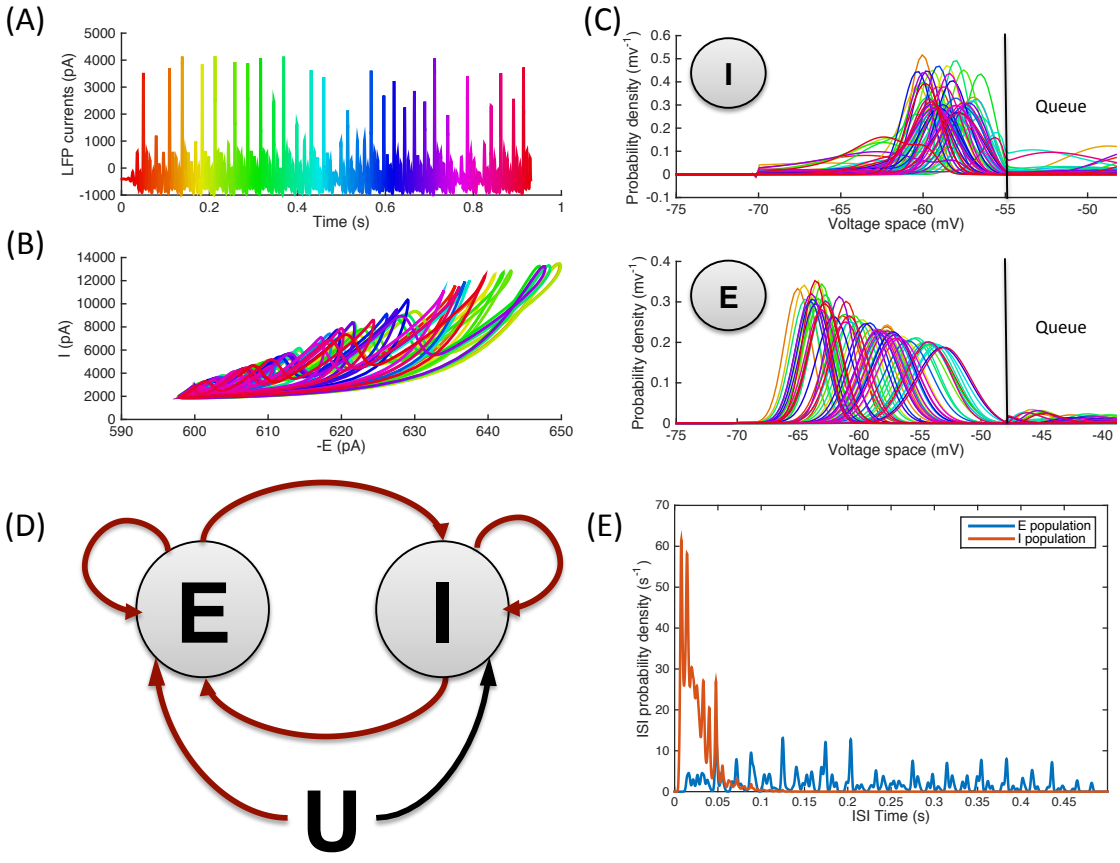

Figure 3.5 - Illustration of a chaotic type behaviour: (A) LFP waveform along an oscillation cycle. Time is colour coded in parts (A)-(C). (B) Cell clamp currents for the excitatory population: inhibitory currents (cell clamped at 0 mV) plotted against excitatory currents (cell clamped at -70 mV), time is colour coded illustrating that the system returns to similar configurations (reflected in these slower state variables) after arbitrarily long time intervals (C) Neuron probability densities over voltage/queue space for the two populations. (D) Schematic representation of the system simulated: red arrows represent strong connections, black arrows represent weak connections. (E) Inter-spike interval probability density distribution: the inhibitory firing rates are higher than that of the excitatory population which fires sparsely.

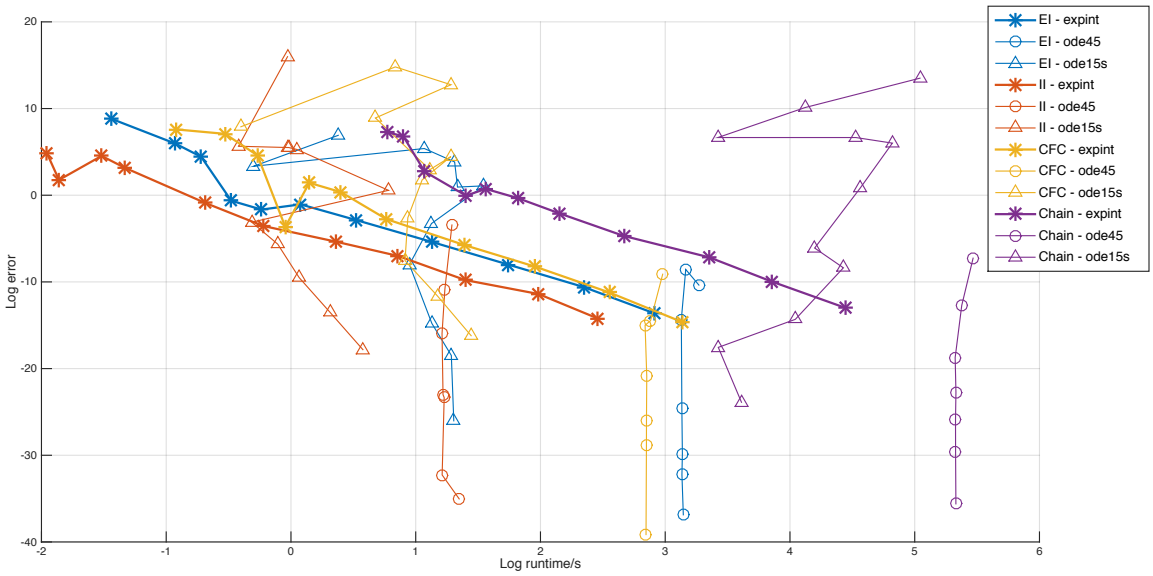

Figure 3.6 - Numerical error plotted against runtime for the *exponential*, *ode45* and *ode15s* integration methods. Colours code the different models, marker shapes code the different integrators. The solvers designed for stiff problems, *exponential* and *ode15s*, outperform the *ode45* in terms of lower runtimes for equivalent numerical precisions. For crude numerical tolerances and systems with a large number of populations, the *exponential* integrator outperforms *ode15s*. When high a numerical precision is required, and the systems involve only two populations, the *ode15s* outperforms the other methods.

3.4 Conclusion

The family of models presented in this work brings together – in a single biologically plausible framework – a wide range of behaviours observed *in vivo* and *in vitro*, some explored in previous separate computational studies (E-I and II gamma behaviour (Brunel, 2000; Brunel and Wang, 2003)), but others, to the best of our knowledge, previously not described via this class of models (cross-frequency-coupling and chaotic behaviour). Expanding on the works of Mattia and Brunel and colleagues (Brunel and Hakim, 1999; Mattia and Giudice, 2002), our mean-field model (and respective integration scheme) can make quantitatively more precise predictions of data that can be acquired in different scenarios; e.g., voltage-clamp slice recordings, or in vivo LFP and multiple unit activity recordings (while previous instances only addressed multiple unit activity). These features make the foundational work reported in this chapter crucial for the developments of chapter 4; where the parameters of the model can be estimated from data in a dynamical causal modelling framework. In this regard, the

computationally efficient numeric scheme introduced here becomes relevant, extending the applicability of such efforts to regular computational resources (such as standard desktop computers). Precise mechanistic and formal modelling of empirical data and predictions of unobserved measurements are then feasible under the above model.

4 BAYESIAN MODEL INVERSION OF MODELS IN LIMIT-CYCLE REGIMES[1]

Bridging the knowledge obtained from single neuron measurements to the behaviour of interacting populations of such neurons is a non-trivial task, particularly when the dynamics of the latter are strongly nonlinear. In this chapter we present a novel methodology that allows the fitting of the interacting populations of conductance based leaky-integrate-and-fire (LIF) neurons, introduced in Chapter 3, to *in vitro* electrophysiological measurements of membrane currents and firing rates during gamma oscillations. These models are able to reproduce mechanistically and quantitatively the interactions between the measured neurons and the general populations in which they are immersed. In this fashion, we comprehensively model and invert autonomous oscillations generated by non-linear neuronal systems.

[1] This chapter is the subject of an article entitled "Bayesian inversion of population models of gamma oscillations" in preparation.

4.1 Introduction

In this thesis so far, we have addressed the modelling of gamma oscillations in a biophysically plausible fashion, while ensuring a level of computational tractability that allows for model estimation endeavours. In this chapter we embark in such undertaking. Our goal is to extend the DCM (Friston et al., 2003) suite of techniques with the ability to address the limit cycle regimes characteristic of the models of neuronal oscillations, and demonstrate its applicability and usefulness with regards to the FP population model introduced in chapter 3, particularly in the setting of *in vitro* gamma oscillation recordings.

We start by describing a number of general methodological advances relative to previous approaches that allow for such model inversion, namely, we extend previous DCM techniques to handle the boundary value problems involved in solving for limit cycle regimes, and to handle full population models based on interacting Fokker-Plank partial differential equations (PDEs). We take special care with the computation of the gradients of the objective function w.r.t the parameters of the model, since this is the most relevant computational bottleneck. Furthermore, we address multimodal data features, which is not standard in DCM practice. We validate the approach by making both qualitative and quantitative predictions about data features that were not used to inform model inversion

The proposed method is general, in the sense that it can be used with any type of generative model based on non-linear systems of ordinary differential equations (ODEs), or discretised PDEs (e.g. neural mass models, predator prey models, central heating thermostats, etc.). To the best of our knowledge, this is also the first attempt at developing a general-purpose Bayesian estimation method for limit cycle waveforms.

4.2 Theory

We seek to model cycle-averaged waveforms around a central oscillation frequency, ω, corresponding to neuronal trans-membrane currents measured via whole-cell voltage-clamp and cell firing rates.

4.2.1 Generative model

In accordance with the DCM standard formalism, we base our approach on a generative model of the following form:

$$\begin{cases} \dot{x} = f(x,\theta) \\ y = g(x,\theta) + \varepsilon \end{cases}$$
$$\varepsilon \sim \mathcal{N}\left(0, \Sigma_\varepsilon(h)\right) \tag{4.1}$$
$$\theta \sim \mathcal{N}(\mu_\theta, \Sigma_\theta)$$
$$h \sim \mathcal{N}(0, \Sigma_h)$$

where f specifies the equations of motion for the hidden states x. Our observations, y, are generated by the observation model, g, and are subject to normally distributed noise ε, with covariance $\Sigma_\varepsilon(h)$, hyper-parameterized by h. The hyper parameter h usually is a vector of scaling factors on the block diagonal components of Σ_ε, with each block pertaining to the autocorrelations of each data channel or modality. The parameter vectors θ and h are also assumed to be normally distributed *a priori*. Note that this last assumption is not overly restrictive since f and g can be chosen to make non-linear transformations to these parameters.

Now the observation model g can, in principle, generate very diverse observation features. Usually in the DCM literature these are based on fMRI BOLD signals, M/EEG recordings or LFP, and pertain to continuous time recordings (as in fMRI BOLD (Friston et al., 2003)), averaged event related potentials (DCM for ERP (David et al., 2006)), cross-spectral features (DCM for cross-spectra (Moran et al., 2009)), or time-frequency data (DCM for induced responses (Chen et al., 2008)). Here we will address cycle-averaged waveforms around a centre oscillation frequency ω. Namely, in our first application these waveforms will be neuronal trans membrane currents measured via whole cell voltage-clamp and cell firing rates.

Because the functions f and g are in general nonlinear, equation (4.1) can in principle have multiple solutions. However, DCMs are usually parameterized in such a way that multiple stable solutions are avoided (or use heuristics to avoid such scenarios, e.g., unambiguous state space initialization and *ad hoc* stabilization of linearly unstable eigenmodes). In contrast to this, we are interested in exploring all those possible

solutions, yet we are not explicitly modelling stochastic effects on the state variables *x*, hence there is no particular reason to prefer one solution to another. Heuristically we then define the likelihood function as the maximum likelihood over all possible solutions, x_i, as:

$$p(y|\theta,h) = max_i\{p(y|x_i,\theta,h)\} \tag{4.2}$$

noting that in practice usually we are not able, nor attempt, to compute all solutions x_i, but during the optimization we allow for the exploration of such solutions. (Depending on the optimization algorithm used, it may be possible to guarantee that the optimal solution is obtained asymptotically).

Still in accordance with the usual DCM formalism, we implement the model inversion scheme within the context of a variational free energy approach to approximate the posterior density of the parameters, $p(\theta,h|y,m)$, given some observed data, y, and generative model m. In the classical DCM approach we seek the approximate posterior density, $q(\theta,h)$, which maximizes the Free Energy lower bound, F, on the model log-evidence, $\ln p(y|m)$, for the observed data under the assumption that q has a fixed Gaussian form and factorizes between θ and h. This can be summarized by the following equations:

$$q(\theta,h) = argmax_q\{F\} \approx p(\theta,h|y,m)$$

$$\begin{aligned} F &= \int \ln p(y,\theta,h|m)\ dq(\theta,h) - \int \ln q(\theta,h)\ dq(\theta,h) \\ &= \ln p(y|m) - D_{KL}\big(q(\theta,h)\ ||\ p(\theta,h|y,m)\big) \leq \ln p(y|m) \end{aligned} \tag{4.3}$$

A variational Bayes (VB) algorithm is used to find the approximate posteriors $q(\theta,h)$ as described in (Friston et al., 2007), and implemented in the SPM academic open source software. However, in the applications that follow, the variance of the hyperparameters *h*, is shrunk to values close to zero for two reasons: first, given the nature of the data (averages over many oscillation cycles), we can get good empirical estimates of the noise amplitude from the experimental measurements; and secondly, the Free Energy functional empirically becomes better conditioned and the optimization procedures converge more robustly. This shrinking of Σ_h reduces the VB algorithm to what effectively becomes a simpler maximum *a posteriori* (MAP) estimate of the

parameters θ, $\mu_{\theta p}$, whereby the covariance of the posterior distribution, $\Sigma_{\theta p}$, is given by the local curvature of the log-posterior function, i.e.:

$$\begin{aligned} \mu_{\theta p} &= argmax_{\theta}\{p(y|\theta)p(\theta)\} \\ \Sigma_{\theta p} &= \left(J^T \Sigma_{\varepsilon}{}^{-1} J + \Sigma_{\theta}{}^{-1}\right)^{-1} \\ J &= -\frac{dg(x,\mu_{\theta p})}{d\mu_{\theta p}} \end{aligned} \tag{4.4}$$

In the following sections we are concerned with the computation of the periodic solutions to equation (4.1) and the computations of the derivatives of the predictions $g(x,\theta)$ with respect to (*w.r.t.*) the model parameters, which are usually the most important computational bottleneck.

4.2.2 Limit cycle solutions

We seek solutions to equation (4.1) at which the system shows self-sustained attracting periodic oscillations, i.e., is in a limit cycle regime. This condition can be formally expressed and summarised with the system of equations $\phi(x,\theta) = \overline{\mathbf{0}}$, as follows:

$$\phi(x,\theta) = \begin{cases} f(x(t),\theta) - \dfrac{\partial}{\partial t}x(t) \\ x(0) - x(T) \\ \dfrac{\partial}{\partial t}x_i(t_k) \end{cases} = \begin{cases} f(x(s),\theta) - \dfrac{1}{T}\dfrac{\partial}{\partial s}x(s) \\ x(0) - x(1) \\ \dfrac{\partial}{\partial s}x_i(s_k) \end{cases} = \overline{\mathbf{0}} \tag{4.5}$$

The first condition here is equivalent to the first condition in equation (4.1). The second condition enforces the periodicity of the solution to a period T. The third condition is an arbitrary "phase anchor" for the solution, such that the system becomes determined; otherwise any delayed version of one solution would also be a solution to the system of equations - $\frac{\partial}{\partial t}x_i(t_k)$ stands for the time derivative of the (one dimentional) state variable x_i at a prescribed time t_k. For convenience we renormalize time, t, such that solutions have unitary period on the variable s. The equations need to be solved for $x(t)$ and T. This type of system of equations is closely related to numerical continuation algorithms (Govaerts and Sautois, 2006), differing only in the absence of a control parameter.

Under the condition that the Jacobians of *f* are not singular, the solution to equation (4.5) is unique in a vicinity of $x(t)$. If the Jacobians are singular, extra conditions have to be incorporated to make the system determined. This is the case of Fokker-Plank equations where the system Jacobians are always singular by construction (Mattia and Giudice, 2002). The constraint that probability densities must to sum to unity has to be incorporated *ad hoc* to render the system invertible and biophysically meaningful. This is done by adding an extra equation for each population *j* and time *t*:

$$\sum_{i \in P_j} x_i(t) = 1, \qquad \forall\, t, j \tag{4.6}$$

where P_j is the set of state space variable indices pertaining to the discretised probability density of population *j*.

4.2.2.1 Finding limit cycles

Solving equation (4.5) requires resorting to numerical algorithms, time discretisation and the use of a zero-finding algorithm, such as Newton's (Newton-Raphson) method. Using a simple first order finite-difference scheme, the first condition of (4.5) becomes:

$$\frac{1}{2}\Big(f\big(x(s_j),\theta\big) + f\big(x(s_{j+1}),\theta\big)\Big) - \frac{1}{T}\frac{1}{(s_{j+1}-s_j)}(x(s_{j+1}) - x(s_j)) = 0 \tag{4.7}$$

We allow for arbitrary step sizes in time to allow for efficient implementations of stiff problems, where certain parts of the limit cycle have to be very finely sampled to achieve a satisfactory numerical precision. We can now write a discretised version of (4.5) as follows:

$$\boldsymbol{\Phi}\big(\widehat{\boldsymbol{X}}\big) = \begin{cases} \boldsymbol{F}_{\boldsymbol{mN}\times\boldsymbol{1}} - \frac{1}{T}\boldsymbol{D}_{\boldsymbol{mN}\times\boldsymbol{mN}}\boldsymbol{X}_{\boldsymbol{mN}\times\boldsymbol{1}} \\ \dfrac{1}{(s_{k+1}-s_k)}\big(x_i(s_{k+1}) - x_i(s_k)\big)_{\boldsymbol{1}\times\boldsymbol{1}} \end{cases} = \overline{\boldsymbol{0}} \tag{4.8}$$

where the $\boldsymbol{D}$ matrix represents the finite difference operator. Note that we can include the second condition of equation (4.5) as a circular structure in $\boldsymbol{D}$, hence the apparent reduction in conditions. For clarity, the dimensions of the matrices and vectors are

subscripted: m is the number of dimensions of the state space and N is the number of discretised time points.

As required for Newton's (Newton-Raphson) method, the Jacobian of the system w.r.t. the unknowns $\widehat{\boldsymbol{X}}$ can be expressed as:

$$\widehat{\boldsymbol{X}} = \left[\boldsymbol{X}_{\boldsymbol{mN}\times\boldsymbol{1}}{}^{T}, \frac{1}{T}\right]^{T}$$

$$\frac{\partial \boldsymbol{\Phi}}{\partial \widehat{\boldsymbol{X}}} = \begin{bmatrix} \frac{1}{2}J_1 - \frac{1}{T}\frac{1}{ds_1}I & \frac{1}{2}J_2 + \frac{1}{T}\frac{1}{ds_1}I & 0 & \cdots & 0 & X_1 - X_2 \\ 0 & \frac{1}{2}J_2 - \frac{1}{T}\frac{1}{ds_2}I & \frac{1}{2}J_3 + \frac{1}{T}\frac{1}{ds_2}I & & & X_2 - X_3 \\ \vdots & & & \ddots & & \\ \frac{1}{2}J_1 + \frac{1}{T}\frac{1}{ds_N}I & 0 & 0 & & \frac{1}{2}J_N + \frac{1}{T}\frac{1}{ds_N}I & X_N - X_1 \\ & \cdots & & \frac{-1}{ds_k} \quad \frac{1}{ds_k} & \cdots & 0 \end{bmatrix} \tag{4.9}$$

The last line non-zero entries pertain to the columns [$m\ k + i$] and [$m\ (k$+1) + i], and J_i are the Jacobians of the equations of motion at time s_i.

We can obtain an initial approximate solution $\widehat{\boldsymbol{X}}_{\boldsymbol{0}}$ either from the previous iteration of the VB algorithm, or by forward integrating the system for a finite interval of time. We then iterate:

$$\widehat{\boldsymbol{X}}_i = \widehat{\boldsymbol{X}}_{\boldsymbol{i-1}} - \left[\frac{\partial \boldsymbol{\Phi}}{\partial \widehat{\boldsymbol{X}}}(\widehat{\boldsymbol{X}}_{\boldsymbol{i-1}})\right]^{-1} \boldsymbol{\Phi}\left(\widehat{\boldsymbol{X}}_{\boldsymbol{i-1}}\right) \tag{4.10}$$

until convergence. The function $f(x, \theta)$ is nonlinear in x, hence $\frac{\partial \boldsymbol{\Phi}}{\partial \widehat{\boldsymbol{X}}}$ must be recomputed at each iteration. The system $\left[\frac{\partial \boldsymbol{\Phi}}{\partial \widehat{\boldsymbol{X}}}(\widehat{\boldsymbol{X}}_{\boldsymbol{i-1}})\right]^{-1} \boldsymbol{\Phi}\left(\widehat{\boldsymbol{X}}_{\boldsymbol{i-1}}\right)$ can be efficiently solved using MATLAB's sparse matrix implementations. In the case of Fokker-Planck equations, a pseudo inverse is necessary due to the addition of the extra linear conditions.

4.2.2.2 Derivatives w.r.t. parameters

We can compute derivatives of the solutions *w.r.t.* the parameters θ more efficiently than with a naïve finite difference method through the use of the analytic implicit function theorem:

$$\phi(x,\theta) = \phi(\varphi(\theta),\theta) = \overline{\mathbf{0}} \Longrightarrow \frac{\partial\varphi(\theta)}{\partial\theta_j} = \left[-\frac{\partial\phi}{\partial x}(\varphi(\theta),\theta)\right]^{-1}\frac{\partial\phi}{\partial\theta_j}(\varphi(\theta),\theta) \quad (4.11)$$

While $\frac{\partial\phi}{\partial\theta_j}$ is computed via finite differences, solving the system to find $\frac{\partial\varphi(\theta)}{\partial\theta_j}$ is computationally little more expensive than one iteration of the Newton's method.

The data predictions and their total derivative *w.r.t.* the parameters can be written as follows:

$$g(x,\theta) = g(\varphi(\theta),\theta)$$
$$\frac{dg}{d\theta_j}(x,\theta) = \frac{\partial g}{\partial\theta_j}(\varphi(\theta),\theta) + \frac{\partial g}{\partial x}\cdot\frac{\partial\varphi(\theta)}{\partial\theta_j} \quad (4.12)$$

in which $\frac{\partial g}{\partial x}$ is never computed since instead we compute finite differences along the directions of $\frac{\partial\varphi(\theta)}{\partial\theta_j}$ which are typically of much lower dimension.

4.2.2.3 Summary, heuristics and caveats

This concludes the description of the necessary elements that allow an efficient implementation of the VB algorithm presented in (Friston et al., 2007) applied to models in limit cycle regimes that enable one to generate model predictions of the data and their derivatives *w.r.t.* the model parameters.

At this stage we also need to address some algorithmic heuristics that, for simplicity of presentation, were not made explicit in the previous sections. Namely, in order to drive the optimization out of stable fixed-point configurations, a penalty term proportional to the real part of the largest eigenvalue of J, is added to the log posterior density. This can be formalised as an implicit prior belief that the observed system does not live in stable fixed-point configurations. This term provides a differentiable expression whose gradient *w.r.t* the parameters ultimately points towards configurations that are linearly unstable.

The Free Energy functional of the approximate posterior density is not necessarily continuous *w.r.t.* the parameters when the optimization algorithm encounters bifurcations of the generative model. However, we have found that these

discontinuities are not too detrimental to the optimization, as the VB algorithm used here employs regularizations and safeguards with respect to discontinuities in Free Energy.

A summary of the algorithm used to generate the data predictions from the model and its derivatives *w.r.t* the parameters is presented in **Figure 4.1**. All the methods presented in this chapter were implemented in MATLAB (ver. 8.4.0.150421 [R2014b]) and will soon be made publically available at https://github.com/mfpleite/NeuralPop.

4.2.3 Non-linear interacting Fokker-Planck population models of conductance based LIF neurons

In this application we use the model described in Chapter 3, which consists of interacting populations described by Fokker-Planck equations of conductance based, stochastic, leaky integrate-and-fire neurons (FP-LIF model). From these we are able to extract predictions of whole-cell voltage clamp currents, single-cell average firing rates and oscillation frequencies when the system adopts a limit cycle configuration. We used a system of one excitatory and one inhibitory population, whose prior parameter distributions were based on data from the Neuroelectro (Tripathy et al., 2015) database for CA1 pyramidal and basket cell inhibitory interneurons (c.f. Table 4.1), which are populations involved in carbachol induced gamma oscillations in this region (Lasztóczi and Klausberger, 2014). The connectivity parameters between the populations were modelled with fairly uninformative prior distributions and were initialized with parameters that result in a fixed-point configuration (Table 4.2).

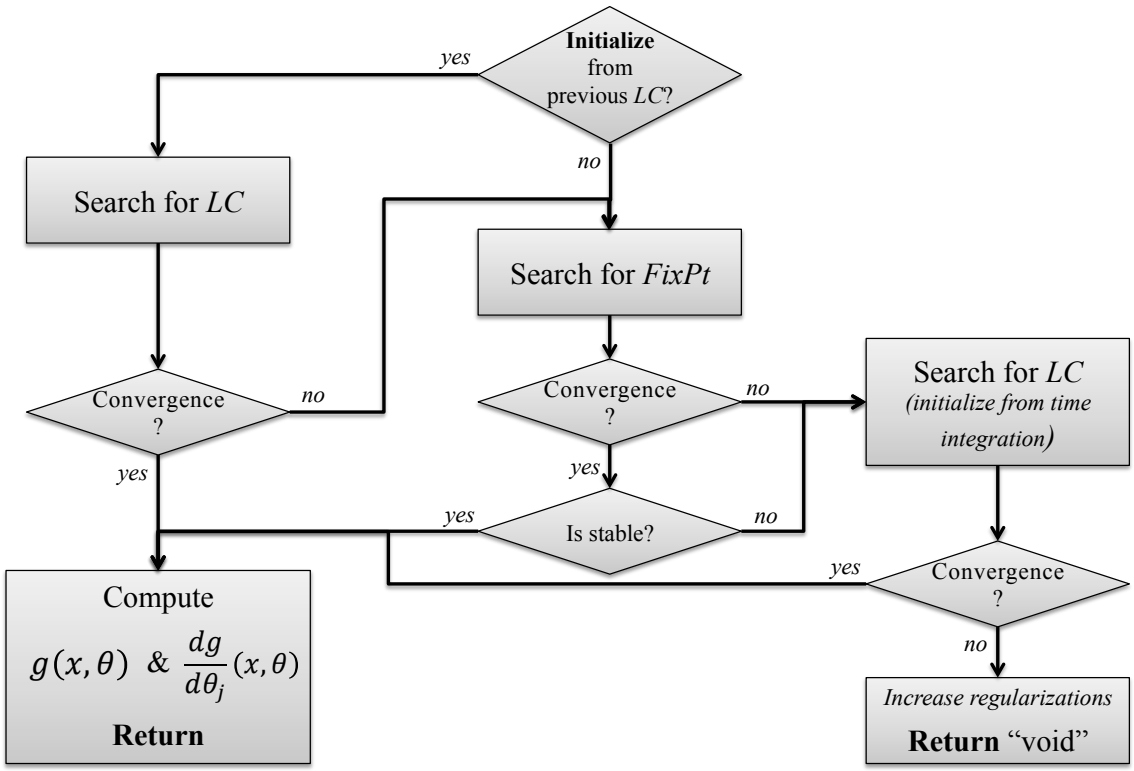

Figure 4.1 – Flowchart of the algorithm developed to compute the model predictions in the context of DCM nonlinear system identification. *LC* – Limit Cycle; *FixPt* – Fixed Point.

Table 4.1 - Cell parameter priors for the two modelled populations

Parameter	Inhibitory interneurons		Pyramidal cells	
	μ_θ	Σ_θ	μ_θ	Σ_θ
log - Capacitance*, C (pF)	log(84)	log(2)	log(150)	log(2)
Leak reversal potential*, V_L (mV)	-62	3	-65	4
log - Leak conductance*, g_L (pF/ms)	log(84/12)	log(2)	log(150/30)	log(2)
Threshold voltage*, V_{th} (mV)	-55	100	-48	50
log - Refractory time*, T_r (ms)	log(1)	log(4)	log(8) [log(36])**	log(4)
Reset voltage, V_r (mV)	-70	0	-70	0
AMPA reversal potential, V_{AMPA} (mV)	0	100	0	100
log - AMPA time constant, T_{AMPA} (ms)	log(16)	log(2)	log(16)	log(2)
GABA reversal potential, V_{GABA} (mV)	-70	100	-70	100
log - GABA time constant, T_{GABA} (ms)	log(5)	log(2)	log(5)	log(2)
log - Diffusion term, $\frac{1}{2}\sigma^2$ (mV²/s)	log(3000)	log(8)	log(4000)	log(8)
Efferent conduction delay (ms)	1	0	1	0

* Values adapted from www.neuroelectro.org for CA1 Basket cells and pyramidal cells.

** Adapted value to reflect maximum firing rate.

Table 4.2 - Network connectivity parameters priors

Excitatory External Input		Inhibitory External Input		Inhibitory connections		Excitatory connections	
μ_θ	Σ_θ	μ_θ	Σ_θ	μ_θ	Σ_θ	μ_θ	Σ_θ
$\log\begin{bmatrix}0.1\\8\end{bmatrix}$ (nS)	50	$\log\begin{bmatrix}0.1\\0.1\end{bmatrix}$ (nS)	50	$\log\begin{bmatrix}0.25 & 0\\0.5 & 0\end{bmatrix}$ (nS neuron^{-1} s)	50	$\log\begin{bmatrix}0 & 0.5\\0 & 0.15\end{bmatrix}$ (nS neuron^{-1} s)	50

4.3 Experimental data and pre-processing

4.3.1 Experimental data

Rita Zemankovics acquired the experimental data used in this chapter. Animals were kept and used according to the regulations of the European Community's Council Directive of 24 November 1986 (86/609/EEC), and experimental procedures were approved by the Animal Welfare Committee of the Institute of Experimental Medicine, Hungarian Academy of Sciences, Budapest. The data set used in the current study overlaps with the data set described in Zemankovics et al. (2013) and the methods for in vitro preparation and electrophysiological recordings are reported in detail there. Briefly, acute horizontal hippocampal slices (450 μm) were prepared from CD1 mice of both sexes (postnatal day 15-23). Experiments were performed at 30-33°C. Oscillations were induced by bath application of the cholinergic agonist carbachol (10-20 μM). Extracellular field potentials and unit activity of neurons were recorded simultaneously in the CA1 region of the hippocampus using standard patch pipettes filled with artificial cerebrospinal fluid (aCSF; with a resistance of 3-6 MOhm). After measuring spiking of individual cells in a loose-patch configuration, the electrode was replaced and whole-cell patch-clamp recordings were performed on the same cells with a new pipette filled with K+-based intrapipette solution. Meanwhile the other electrode was kept in place for continuous recording of the extracellular field potentials. Cells were held at the estimated inhibitory (~ -70 mV) and excitatory (~ 0 mV) reversal potentials to record excitatory and inhibitory postsynaptic currents (EPSCs and IPSCs), respectively.

4.3.2 Pre-processing

Figure 4.2 illustrates the pre-processing of the LFP recordings. Firstly we compute Morlet wavelet transforms (R=4) for each LFP time course. Then we identify the central frequency of the oscillation as the peak of the power averaged across time. The (un-wrapped) instantaneous phase at the central frequency was used to re-sample both the LFP and the concomitant current/spike recording time courses. The resulting time courses are rearranged to matrix form, in which each gamma cycle has an equal number of samples. An automated algorithm (developed in-house) was used to identify the neuronal spike times from the cell-attached recordings. An overview of the pre-processing data for a representative inter-neuron is presented in **Figure 4.3**. The

covariance structure of the measurement noise ($\Sigma_\varepsilon(h)$) was estimated from the data (regularized covariance of the mean estimator) and the hyper-prior covariance, Σ_h, was set to very small values.

A total of 7 pyramidal neurons and 2 inhibitory interneurons were selected, from a pool of 32 neurons, with the criterion that their spiking should be phase coupled with the gamma oscillations (**Figure 4.4**) in accordance with previous experiments involving carbachol induced gamma oscillations (Oren et al., 2006). An average dataset, representative of the average neuron of each population, was generated by (precision-weighted) averaging the mean currents, firing rates and oscillatory frequencies of each of the selected neurons. The covariance matrices were also averaged in order to represent a typical dataset. We chose not to assume a fixed effects model (i.e. summing the inverse covariance matrices) as the data was too heterogeneous for such assumption to be realistic, nor did we have enough neurons to estimate a random effects model (N=2 for the interneuron population). The adopted average covariance is an intermediate solution between these two options.

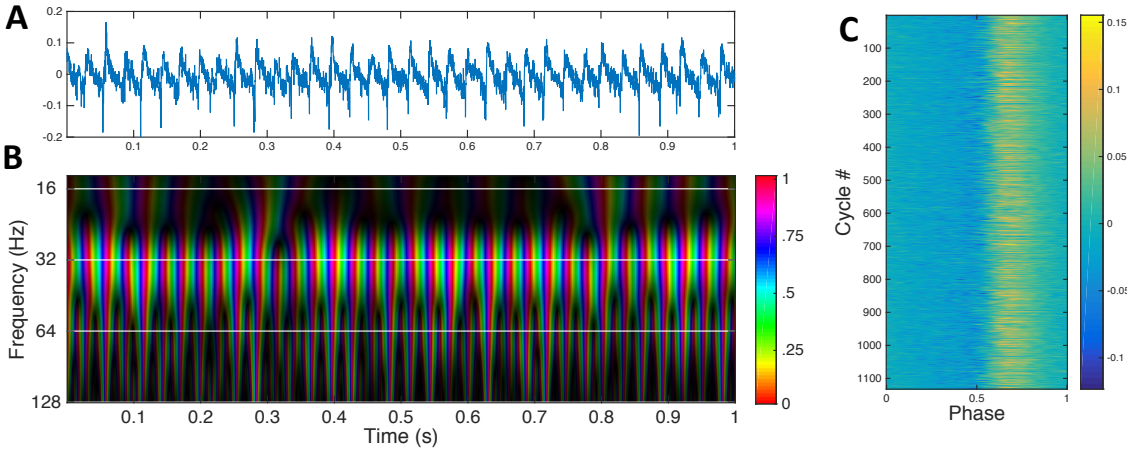

Figure 4.2 - **A** – Example 1 second segment of the LFP recording of the carbachol induced gamma oscillation. **B** – Morlet wavelet transform of the LFP segment presented in A. The *hue* component of the colour map codes for phase and the *value* codes for amplitude. **C** – LFP resampled to constant phase intervals of the dominant frequency and rearranged with aligned cycles.

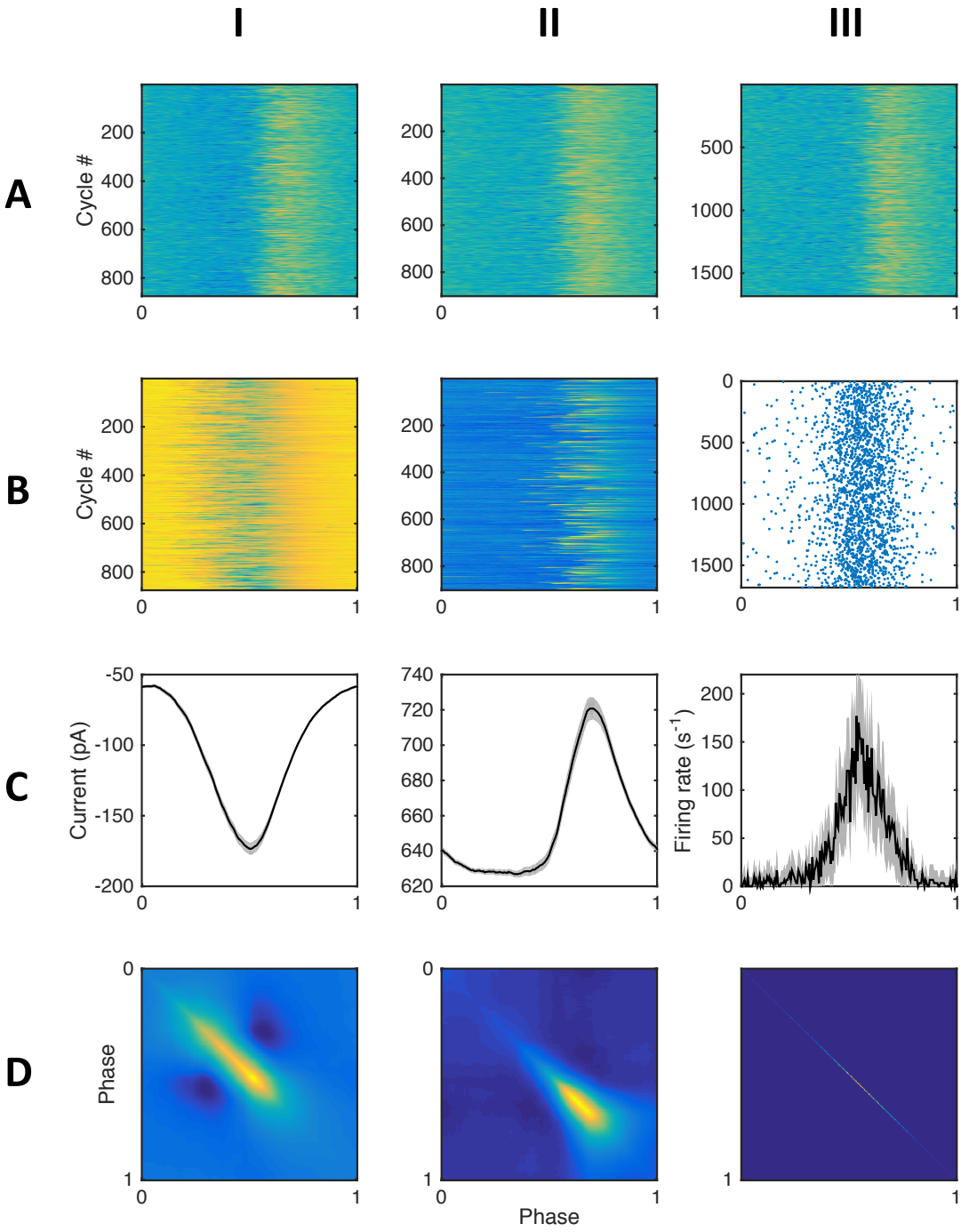

Figure 4.3 - Data summary for an example inhibitory interneuron – **Column I** - whole cell voltage clamp recordings at -70 mV (excitatory currents); **Column II** - whole cell voltage clamp recordings at 0 mV (inhibitory currents); **Column III** - cell attached recordings (spiking activity); **Row A** – resampled LFP (as in **Figure 4.2** C); **Row B** – resampled currents/spike times measured concurrently to the LFP of row A; **Row C** – Cycle averaged Currents/ firing rates plus and minus two standard errors of the mean; **Row D** – Covariance of the estimator of the means of row C.

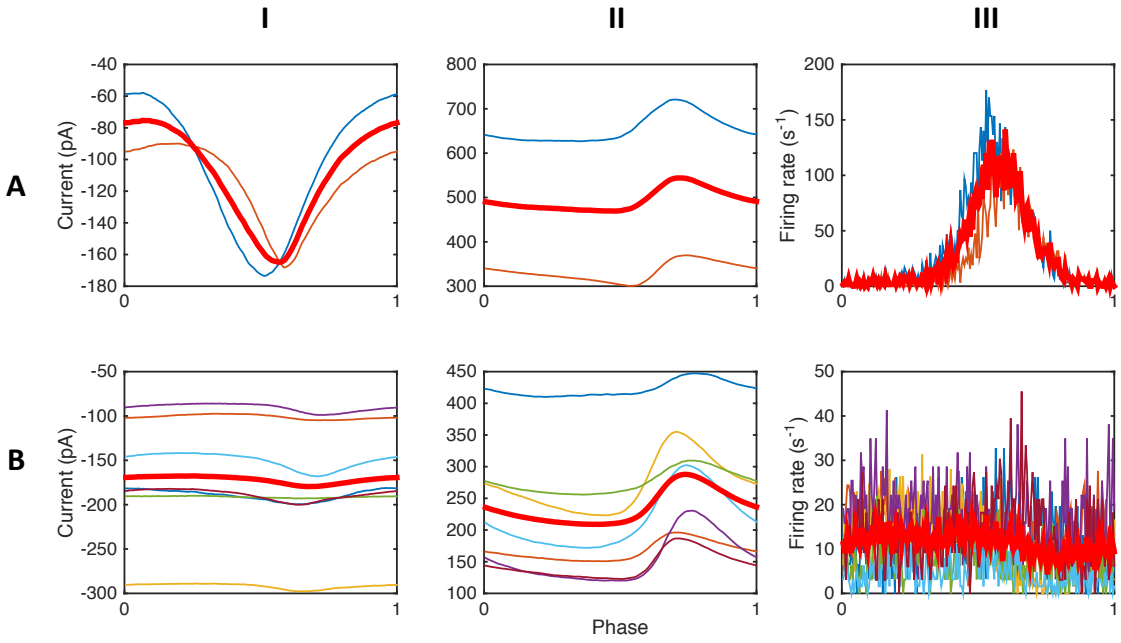

Figure 4.4 - Cycle averaged excitatory currents (column **I**), inhibitory currents (column **II**) and firing rates (column **III**) for the selected inhibitory interneurons (N=2, row **A**) and pyramidal cells (N=7, row **B**) – each colored thin trace represents one neuron, and the red bold traces represent the respective population averages.

4.4 Results

4.4.1 Model fits

The FP-LIF generative model was fit to the data summarized in the cycle-averaged waveforms as described so far. In **Figure 4.5** we illustrate how the algorithm evolves over iterations. The Free Energy optimization is initialized with the prior distribution, which results in a stable fixed-point configuration for the FP-LIF system. The VB algorithm then quickly escapes the stable fixed-point configuration and gradually fits the data features in a limit cycle configuration. The main features of the data are accurately explained by the model: the membrane current amplitudes are appropriately fitted (the DC component was removed from the waveforms, as these are not measured reliably); the excitatory currents slightly precede inhibition; the firing rate values and phase coupling for each population are consistent; and the frequency of the self sustained oscillation is also well approximated by the model.

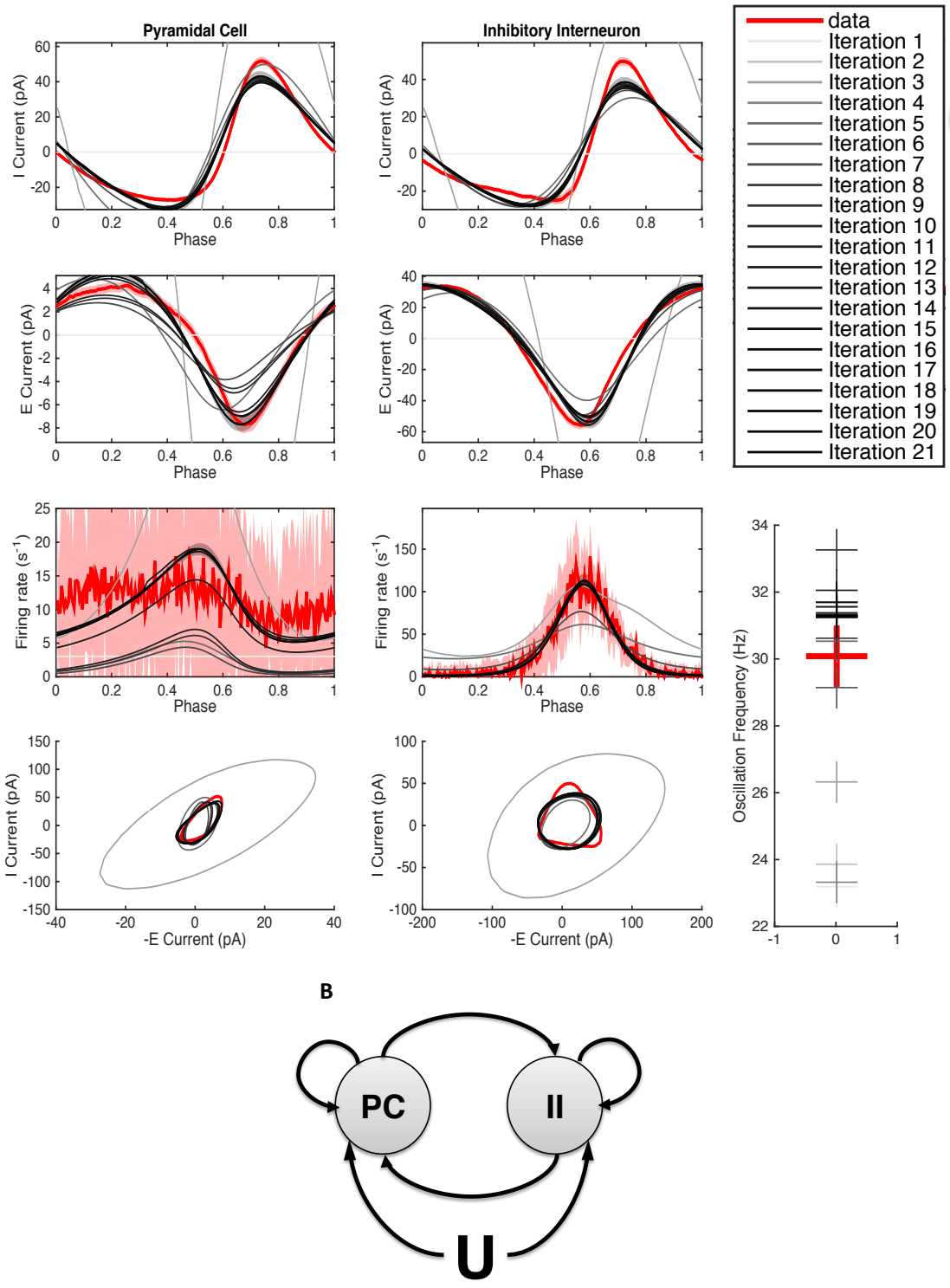

Figure 4.5 - **A** - Model fit to the summary data along the iterations of the VB algorithm – Shaded regions indicate the 2-sigma confidence intervals of the data (pink) and final model fits (gray). **B** – Schematic representation of the structure of the fitted model.

4.4.2 Model predictions

Figure 4.6 shows the predicted inter-spike-interval (ISI) distributions computed based on the posterior expected parameters obtained by fitting the cycle-averaged data. We compare these to the histograms of the gamma cycle aligned ISIs observed for the two populations of neurons. Also, as a benchmark, we show the ISIs that a Gamma rate neuron model would predict if the cycle averaged firing rates were fitted perfectly. We show results for two different *prior* settings for the refractory time of the excitatory population based on the Neuroelectro database for this neuron class; the first represents the duration of the neuronal spike, and the second reflects the inverse of the maximum firing rate.

The results in **Figure 4.6** are remarkable because they are based on parameters estimated purely on cycle-averaged data – data that do not contain any explicit information about inter-spike intervals. The fact that the distribution of spikes can be predicted in this fashion speaks to the validity of the model and, crucially, the parameter estimates afforded by the estimation scheme. In order to get similar results with a Gamma rate model (Barbieri et al., 2001), the shape parameter of the gamma distribution needed to be fitted to the ISI data itself.

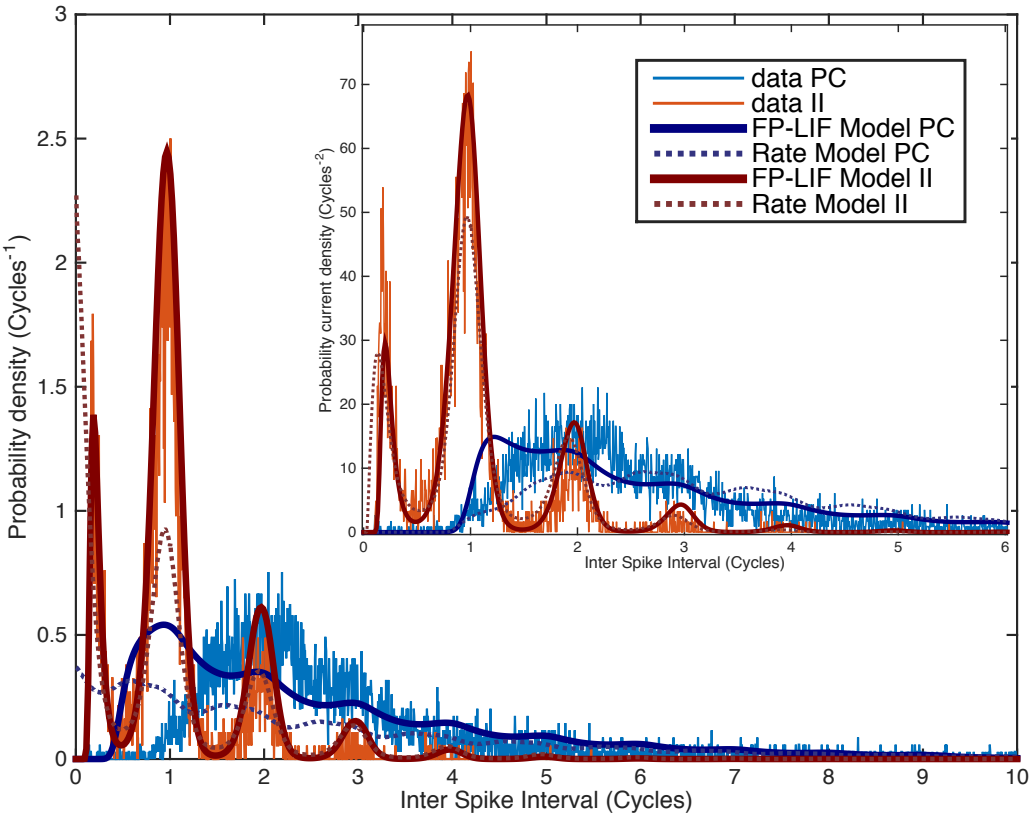

Figure 4.6 - Inter-spike-interval (ISI) distributions predicted by the fitted FP-LIF model and a Gamma rate model compared to the ISI distributions measured from the data. The insert corresponds results obtained from an altered prior distribution for the refractory time of the principal cell population in the FP-LIF model, and as well as a fine-tuned shape parameter (k = 1 vs k = 2.6) for the Gamma rate model based on the data ISI distributions. Blue lines represent pyramidal cells (PC), red lines represent inhibitory interneurons (II). Thin lines represent the measured densities, solid bold lines represent the FP-LIF model predictions and dashed bold lines the Gama rate model predictions.

4.5 Discussion

A crucial element in any computational modelling task is to achieve the right balance between realism and abstraction: realism in the sense that the model should be able to accurately describe the key features that one is interested in describing; and abstraction in the sense that the model should be simple enough to be practically manageable and to be able to provide insight on the phenomena it seeks to describe. In the present work several simplifying assumptions were made in the model while providing at least some degree of predictive power on the phenomenon of gamma oscillations.

4.5.1 Modelling assumptions and approximations

We start by addressing the assumption that the observed system is in a deterministic limit-cycle regime. This assumption can be contrasted with the substantial degree of heterogeneity (above white noise) of the currents that the individual neurons receive at each gamma cycle (**Figure 4.3**). However, we are interested in describing an "average oscillation", hence we average the cycle-to-cycle observed variability. This operation of time averaging can correspond to, by evoking ergodic arguments, a state-space averaging of the stochastic dynamics, wherein the average of the state space dynamics approximates the limit cycle of the deterministic component on the condition that the stochastic terms are reasonably small.

Similarly, the variability in the averaged dynamics of each measured neuron seems to challenge the "mean-field" assumption, in which all neurons in each model population are assumed to be equal and only distinguishable by their random input fluctuations (see **Figure 4.4**). However, key qualitative features are preserved throughout the selected neurons: the relative phases at which excitatory and inhibitory currents peak are similar and the phase coupling of the firing rates with the LFP oscillation is also qualitatively similar across neurons. The averaged results resemble a realistic neuron and are, at least qualitatively, indistinguishable from the ones experimentally measured. The effects of neural heterogeneity in neural population dynamics have been explored in the literature (Grabska-Barwinska and Latham, 2014), yet these render more complex, and computationally expensive, models that are less suitable to attempts at inverting them based on experimental data. Hence the mean-field approximation is an assumption that carries invaluable practical advantages, but its possibly non-trivial effects need to be acknowledged with respect to the interpretability of the posterior model parameters.

4.5.2 Model inversion: theoretical and practical considerations

The Bayesian model inversion method introduced in this paper suffers from the same caveats as any approximate Bayesian inference method on non-linear models. In particular, and perhaps most importantly, the posterior distributions are only approximate and the optimization methods are generally susceptible to trapping in local extrema. Methods that alleviate these issues exist, albeit computationally expensive, and were left out of the scope of the present work. These are being studied elsewhere in the

context of DCM (Lomakina et al., 2015; Sengupta et al., 2016, 2015) and might be applied to this problem in the future.

Furthermore, degenerate dynamics (i.e. similar solutions with different model parameters) are also commonplace in nonlinear system models. This type of problems can be addressed by adding different experimental conditions to the data that can only be explained by changes to a sub-set of the model parameters (such as for example, pharmacological manipulations that should not affect cell capacitances). This strategy is standard in the DCM literature (Stephan et al., 2010) and shall be used in future applications of the methodology introduced here.

4.5.3 Model's predictive power

Finally the two-population FP-LIF model chosen here was able to fit the features of the data both qualitatively and quantitatively and convergence to a local maximum was rapid (yet one cannot guarantee that this is an absolute maximum). We note that the parameters obtained, when used to generate ISI distribution estimates, produced predictions in remarkable agreement with the measurements. The better fit of inhibitory firing rates relative to the excitatory ones, may explain the better quality of the predicted ISI distributions for this population. However, high-quality fits to the firing rates do not necessarily correspond to superior ISI predictions, as illustrated by the Gamma rate model predictions; therefore the predictive power of the model showcased here is not a trivial consequence of data fitting.

A noteworthy feature of the inverted model is that it translates to a PING model ("E-I" model of Chapter 3) where both the excitatory and inhibitory population are critical for the dynamics of the gamma oscillation, as opposed to ING models ("I-I" model of Chapter 3) of gamma oscillations, where these are sustained mostly by self-inhibition of the interneuron population.

The potential applications of model inversion in this context are manifold. There are several important conditions that implicate a loss of cortical excitability and gain control – possibly mediated by abnormal exchange between inhibitory interneurons and excitatory pyramidal cells. A clear candidate here is epilepsy (that we will pursue below). Another important condition – that is often considered in terms of a pathophysiology of excitation-inhibition balance – is schizophrenia. It is possible that

the methodology developed here will contribute to understanding the synaptic basis of conditions such as schizophrenia and epilepsy.

4.6 Conclusion

In this chapter we have presented a novel Bayesian method to invert generative models of limit cycle waveforms. The method extends DCM, allowing for the first time the exploration of deterministic non-linear dynamics in limit cycle regimes that were previously not formally addressable by this family of methods. We illustrated the first application of this method to the new generative model (described in Chapter 3) of trans-membrane currents and firing rates of neurons incorporated in interacting neural population networks. To our knowledge, this constitutes the first demonstration of a Bayesian method designed to invert generative models of limit cycles and the first estimation of Fokker-Planck neural population models based on experimental data. These advances allow to mechanistically bridge multimodal data recorded from single neurons to properties of the behaviour of interacting neural populations, enabling a model-based approach to systems neuroscience. In the next chapter, we sketch a proof of principle application to the techniques described above to non-invasive data acquired during seizure activity.

5 EPILOGUE: AN APPLICATION TO EPILEPTIC GENERALIZED SPIKE AND WAVE SEIZURES

The methodology presented in this chapter can be applied to lumped neural mass models of generalised spike and wave seizure (SWS) activity as typically observed in clinical EEG recordings of patients with idiopathic generalised epilepsy: 3 Hz spike and wave discharges. In this closing section we illustrate such application and some of the caveats that it entails.

5.1 Neuronal mass model of SWS

In equation (5.1) a common neuronal mass model is presented. This model reproduces the dynamics of spike and wave seizures, as observed in the EEG of patients with generalized epilepsies. The model characterizes a cortical architecture with one principal cell population that is connected to a second excitatory population, a slow and a fast inhibitory population. A detailed motivation for such model is presented in (Wendling et al., 2005) and detailed studies of its dynamics were made in (Faugeras, 2006; Goodfellow et al., 2011; Touboul et al., 2011).

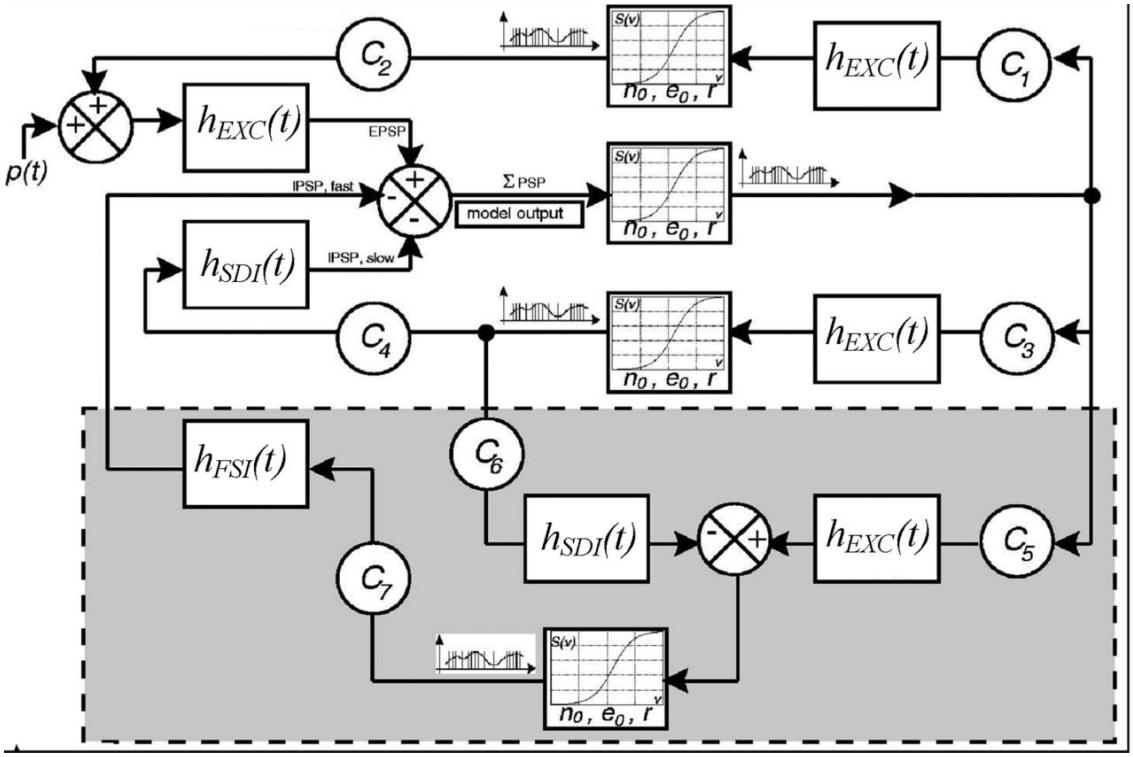

Figure 5.1 – Schematic representation of the neural mass model considered in the present chapter and formalized in equation (5.1) adapted from (Wendling et al., 2005).

The model is characterized by the following equations:

$$f(x,\theta) = \begin{bmatrix} x_5 \\ x_6 \\ x_7 \\ x_8 \\ AaS\left(x_2 - \frac{1}{2}x_3 - \frac{1}{2}x_4\right) - 2ax_5 - a^2x_1 \\ Aa\left(I + C_2S(C_1x_1)\right) - 2ax_6 - a^2x_2 \\ BbC_4S(C_3x_1) - 2bx_7 - b^2x_1 \\ DdC_4S(C_3x_1) - 2gx_8 - g^2x_1 \end{bmatrix}, \tag{5.1}$$

$$S(v) = 2e_0 / \left(1 + \exp\left(r_0(v_0 - v)\right)\right)$$

$$g(x,\theta) = \begin{bmatrix} L\left(x_1 - \frac{1}{2}x_2 - \frac{1}{2}x_3\right) \\ \log(\omega) \end{bmatrix},$$

The state variables x_1, x_2, x_3 and x_4, represent average voltages of the postsynaptic potentials elicited by each population, respectively: pyramidal cells, secondary excitatory population, fast inhibitory population and slow inhibitory population. The state variables x_5, x_6, x_7 and x_8 are their corresponding time derivatives. The standard observation model, *g,* is used, representing a single channel close to this cortical source and it is the average postsynaptic potential received by the population of pyramidal cells multiplied by an arbitrary lead field gain *L*. The prior parameters for the model were chosen such that they broadly yield a region where the model behaves in a spike and wave seizure like dynamic and are presented in Table 1. The priors were defined relative to log-scaling factors on base parameter values extracted from (Goodfellow et al., 2011) .

Table 5.1 - Model parameter priors for the SWS model

Index	Parameter	Description	Value	μ_θ	Σ_θ
1	A	Average excitatory gain	$e^{\theta_1} \cdot 3.25$ mV	0	1
2	B	Average fast inhibitory gain	$e^{\theta_2} \cdot 44$ mV	0	1
3	D	Average slow inhibitory gain	$e^{\theta_3} \cdot 8.8$ mV	0	1
4	a	Excitatory time constant	$e^{\theta_4} \cdot 100$ s^{-1}	0	1
5	b	Fast inhibitory time constant	$e^{\theta_5} \cdot 100$ s^{-1}	0	1
6	d	Slow inhibitory time constant	$e^{\theta_6} \cdot 20$ s^{-1}	0	1
7	C	Conectivity gains	$e^{\theta_3} \cdot 135$	0	1
8	L	Lead field gain	$e^{2\theta_8}$	0	1
9	I	External Input	$e^{\theta_3} \cdot 100$ s^{-1}	0	1
10	-	Arbitrary phase parameter	θ_{10}	0	10
8	r, e, v	Sigmoid function parameters	.56 mV^{-1}, 2.5 s^{-1}, 6 mV	-	fixed

5.2 Clinical EEG data, pre-processing and model fit.

The data used in this section was acquired as part of the clinical evaluation of a patient with idiopathic generalised epilepsy. It was acquired at the Hospital Júlio de Matos, in Lisbon, by Dr. Alberto Leal, and the use of the data for research had explicit consent by the legal guardians of the patient. An EEG system with 83 channels and 500 Hz sampling rate was used. The longest of ten seizures recorded for this patient was selected for this analysis. The EEG signal was band pass filtered from .5 Hz to 70 Hz, and the channel with highest SWS signal amplitude was selected. The remainder of the pre-processing was done in an analogous fashion to section 4.3.2 and is summarized in **Figure 5.2** (panels A-D) alongside with the model fit obtained by the methods described in 4.2.

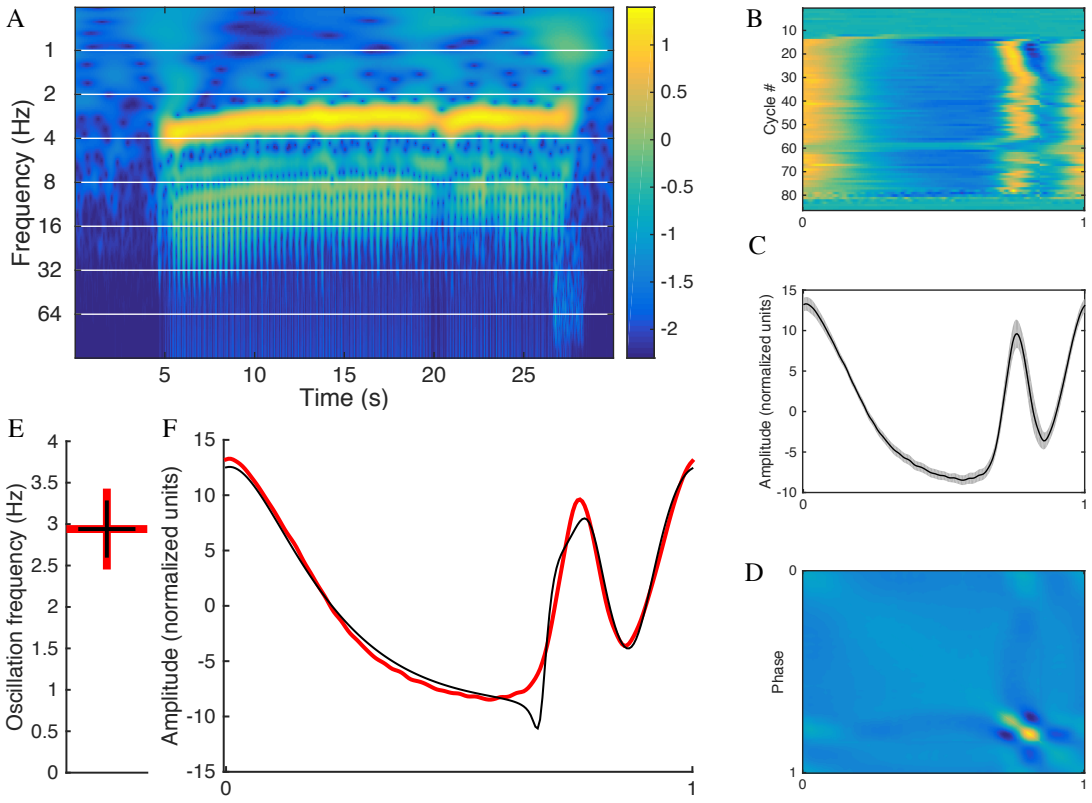

Figure 5.2 - **A** – Morlet wavelet transform of the EEG from the selected channel and seizure segment. The colour map represents log amplitude. **B** –EEG resampled to constant phase intervals of the dominant frequency and rearranged with aligned cycles. **C** – Mean seizure waveform (plus and minus two standard errors of the mean) computed from cycles 14 to 80 of panel B. **D** – Covariance of the estimator of the mean waveform of panel C. **E** – Central frequency of the seizure (red) and its model fit (black). **F** – Average waveform of the seizure (red) and its model fit (black)

The characteristically stable ~3 Hz waveform of this type of seizures is patent in panel A. This waveform remains relatively constant throughout the ~20 s seizure (panel B). The fitting algorithm applied to the neuronal mass model of equation (5.1) was able to broadly describe the central frequency and average waveform of the seizure (panels E and F). However, a characteristic negativity at phase ~0.7 on the model waveform was not eliminated by the fitting procedure, albeit absent in the data.

5.3 Face validity tests

To inquire the interpretability of the parameter estimates for this model, a face validity study was performed with simulated data for parameters near the prior mean (the simulation parameters were drawn from a Gaussian distribution with the same mean as the prior, but covariance scaled by 0.01). Noise with the same covariance structure as **Figure 5.2** panel D at a signal to noise ratio (SNR) of 20 was added to the simulated waveforms. The simulated waveforms and corresponding fits are presented in **Figure 5.3** alongside the estimated posterior distributions and simulation parameters.

The results from the simulated waveforms seem to indicate that the model lives near a bifurcation of limit cycles for the parameters close the prior mean: the waveforms cluster in two very distinct shapes, panels a) to e) and f) to j) **Figure 5.3**; these waveforms are similar to the ones reported in (Goodfellow et al., 2011). The fitting algorithm seems to cope well with such discontinuity and is able to fit the waveforms of both types of examples. However, the posterior estimates behave very differently in each cluster. For the a) to e) cluster the posterior means are much closer to the true simulated parameters, than in the f) to j) cluster; also, the posterior covariances are generally broader in the latter. These results are intuitive taking the fact that the a) to e) cluster has waveforms with more features (above noise level) than the f) to j) cluster, and parameter changes result in more abrupt differences in the generated data predictions. In both groups of waveforms the posterior estimates of the parameters are always overconfident, i.e., the true parameters of the simulated data lie, for all examples, outside the 95% confidence ellipsoid of the posterior. A particularly bad example is b), where the fit is slightly poorer, and the posteriors for parameters 4, 5 and 6 place precise confidence intervals on incorrect values.

5.4 Conclusion

The results of this section show that the Bayesian model inversion scheme developed in section 4.2 can be applied to neural mass models of SWS, being able to fit seizure waveforms as measured from clinical EEG. However, these results also show that the nonlinearities of the models at question considerably violate the variational Laplace approximations, and consequently the posterior parameter estimates are to be interpreted with due caution. Also, local minima can severely hinder model estimations, as example b) of **Figure 5.3**. As opposed to the results from section 4.4, here there are

no independent data features that would enable us to demonstrate predictive validity directly. As noted above, this problem can be finessed by using experimental manipulations such as pharmacological interventions and possibly results of surgical outcome. These interventions provide an opportunity to establish the predictive validity to the sorts of estimates described above.

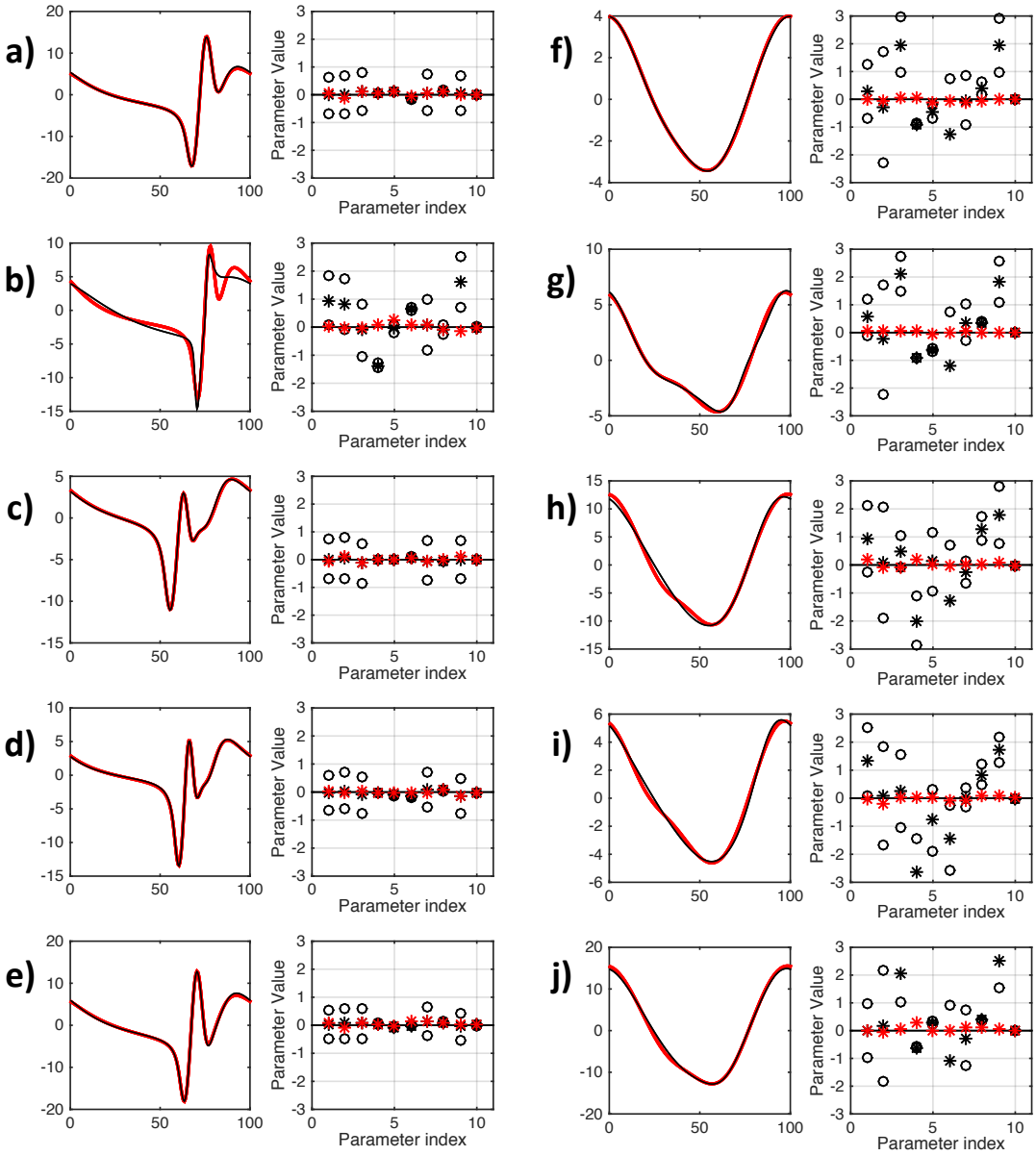

Figure 5.3 – Ten examples from face validity tests: Simulated parameters and waveforms in red. Fitted waveforms and posterior estimates in black: "*" markers represent posterior means and "o" markers +/- two standard deviations (more precisely: twice the square root of the diagonal component of the posterior covariance matrix)

6 CONCLUSIONS

6.1 Findings and achievements

In this thesis I started by arguing that the modelling of fast gamma oscillations based on neuronal mass models does not support a precise biophysical interpretation for its parameters, contrarily to what previous results in the literature might imply (Molaee-Ardekani et al., 2010; Moran et al., 2011). Consequently I avoided the use of this family of models in the pursuit of model-based analyses of patient specific focal seizure activity, whose fast oscillatory onsets are now believed to be a hallmark of epileptogenicity (Jacobs et al., 2008; Park et al., 2012), and the use of neural mass models could impose incorrect constrains on the inferences made about the specific pathologies of each patient.

Instead, I have then pursued an alternate, more flexible, and relatively more biophysically grounded approach to the modelling of neural populations, whose application to the study of gamma oscillations had already an established literature: mean-field Fokker-Planck models of integrate-and-fire neurons. I introduced and explored a new variant of these models that affords a rich repertoire of measurable data features, namely, both trans-membrane currents and firing rates as measured from single neurons, and also population properties, such as local field potentials and ensemble frequency responses.

This family of models are considerably more computationally demanding than neuronal mass models, since they are based on PDEs as opposed to small sets of ODEs. Hence I have tailored efficient numerical methods to the specificities of the ensuing nonlinear Fokker-Planck equations. These methods, based on exponential integrators, offered

sufficient performance to allow the exploration of model estimation techniques. However, in order to maintain the computational burden manageable by standard desktop computers, I have started by the exploration of estimation techniques based on summary statistics of data, avoiding more intensive techniques that rely on the estimation of stochastic dynamics.

In the remainder of the thesis I extended the DCM suite of techniques in order to handle models behaving in limit cycle regimes and address gamma oscillations as modelled by the LIF-FP population model. In this approach I have analysed data acquired from *in vitro* slice preparations of carbachol induced gamma oscillations in the CA1 region of the mouse hippocampus. This data was summarized in cycle averaged waveforms of excitatory and inhibitory trans-membrane currents and firing rates for two populations of neurons known to play key roles in gamma oscillations: pyramidal neurons and PV+ inhibitory interneurons. The two population excitatory-inhibitory LIF FP model was able to fit to a good degree of accuracy the experimental data of the *in vitro* gamma oscillations. Crucially, this fitted model was able to predict the inter-spike-interval distributions for these populations of neurons – data that were not used to optimise model parameters. Conceptually, the fitted model also illustrates a PING mechanism at play for this type of gamma oscillation, and bridges the properties measured at the single neuron micro scale, to the oscillatory behaviour of the population macro scale.

These new methodologies and applications provide the DCM literature with an unprecedented biophysical precision that in itself allows for more ambitious mechanistic claims that are also easily tested with independent data features.

6.2 Limitations and future work

The methods developed in this thesis suffer, however, from the same limitations as many estimation techniques have for nonlinear models; namely, they are only approximate and are prone to local extrema. These issues were illustrated in an example application to spike and wave seizure dynamics estimated with a JR model variant. Future work should therefore focus on the mitigation of these problems by exploring more robust nonlinear optimization techniques (e.g., stochastic gradient descent, genetic algorithms, etc.) and/or sampling approaches to the estimation of the parameter posterior distributions (e.g., MCMC (Sengupta et al., 2016)). Once these issues are better understood, applications of the FP population model to different systems and

conditions can be explored, eventually including estimations with stochastic dynamics in continuous time. The modularity and generality of the models and methods presented in this thesis endow them with a wide range of possible applications to be explored in the future (e.g. beta oscillations, *in vivo* multi-unit activity…).

7 REFERENCES

Abbott, L.F., van Vreeswijk, C., 1993. Asynchronous states in networks of pulse-coupled oscillators. Phys Rev E Stat Phys Plasmas Fluids Relat Interdiscip Top. 48, 1483–1490.

Akam, T., Oren, I., Mantoan, L., Ferenczi, E., Kullmann, D.D.M., 2012. Oscillatory dynamics in the hippocampus support dentate gyrus–CA3 coupling. Nat. Neurosci. 15, 1–9. doi:10.1038/nn.3081

Allen, P.J., Fish, D.R., Smith, S.J., 1992. Very high-frequency rhythmic activity during SEEG suppression in frontal lobe epilepsy. Electroencephalogr. Clin. Neurophysiol. 82, 155–9.

Badel, L., Lefort, S., Berger, T.K., Petersen, C.C.H., Gerstner, W., Richardson, M.J.E., 2008a. Extracting non-linear integrate-and-fire models from experimental data using dynamic I-V curves. Biol Cybern 99, 361–370. doi:10.1007/s00422-008-0259-4

Badel, L., Lefort, S., Brette, R., Petersen, C.C.H., Gerstner, W., Richardson, M.J.E., 2008b. Dynamic I-V curves are reliable predictors of naturalistic pyramidal-neuron voltage traces. J. Neurophysiol. 99, 656–66. doi:10.1152/jn.01107.2007

Baladron, J., Fasoli, D., Faugeras, O., Touboul, J., 2012. Mean-field description and propagation of chaos in networks of Hodgkin-Huxley and FitzHugh-Nagumo neurons. J. Math. Neurosci. 2, 10. doi:10.1186/2190-8567-2-10

Barbieri, R., Quirk, M.C., Frank, L.M., Wilson, M.A., Brown, E.N., 2001. models of neural spiking activity 105, 25–37.

Bartolomei, F., Chauvel, P., Wendling, F., 2008. Epileptogenicity of brain structures in human temporal lobe epilepsy: a quantified study from intracerebral EEG. Brain 131, 1818–30. doi:10.1093/brain/awn111

Berg, A.T., Berkovic, S.F., Brodie, M.J., Buchhalter, J., Cross, J.H., van Emde Boas, W., Engel, J., French, J., Glauser, T.A., Mathern, G.W., Moshé, S.L., Nordli, D., Plouin, P., Scheffer, I.E., 2010. Revised terminology and concepts for organization of seizures and epilepsies: report of the ILAE Commission on Classification and Terminology, 2005-2009. Epilepsia 51, 676–85. doi:10.1111/j.1528-1167.2010.02522.x

Bertram, E.H., Zhang, D.X., Mangan, P., Fountain, N., Rempe, D., 1998. Functional anatomy of limbic epilepsy: a proposal for central synchronization of a diffusely hyperexcitable network. Epilepsy Res. 32, 194–205.

Borisyuk, R.M., Kirillov, A.B., 1992. Bifurcation analysis of a neural network model. Biol. Cybern. 66, 319–25.

Brunel, N., 2000. Dynamics of sparsely connected networks of excitatory and inhibitory spiking neurons. J. Comput. Neurosci. 8, 183–208.

Brunel, N., Hakim, V., 2008. Sparsely synchronized neuronal oscillations. Chaos 18, 15113. doi:10.1063/1.2779858

Brunel, N., Hakim, V., 1999. Fast global oscillations in networks of integrate-and-fire neurons with low firing rates. Neural Comput. 11, 1621–1671. doi:10.1162/089976699300016179

Brunel, N., van Rossum, M.C.W., 2007. Lapicque's 1907 paper: from frogs to integrate-and-fire. Biol. Cybern. 97, 337–9. doi:10.1007/s00422-007-0190-0

Brunel, N., Wang, X.-J., 2003. What determines the frequency of fast network oscillations with irregular neural discharges? I. Synaptic dynamics and excitation-inhibition balance. J. Neurophysiol. 90, 415–30. doi:10.1152/jn.01095.2002

Buesing, L., Macke, J.H., Sahani, M., 2012. Learning stable, regularised latent models of neural population dynamics. Network 23, 24–47. doi:10.3109/0954898X.2012.677095

Burkitt, a N., 2006. A review of the integrate-and-fire neuron model: II. Inhomogeneous synaptic input and network properties. Biol. Cybern. 95, 97–112.

doi:10.1007/s00422-006-0082-8

Chen, C.C., Kiebel, S.J., Friston, K.J., 2008. Dynamic causal modelling of induced responses. Neuroimage 41, 1293–312. doi:10.1016/j.neuroimage.2008.03.026

Chu, S.C., Berman, M., 1974. An exponential method for the solution of systems of ordinary differential equations. Commun. ACM 17, 699–702. doi:10.1145/361604.361627

Cooray, G.K., Sengupta, B., Douglas, P.K., Friston, K., 2015. Dynamic causal modelling of electrographic seizure activity using Bayesian belief updating. Neuroimage 125, 1142–54. doi:10.1016/j.neuroimage.2015.07.063

Daunizeau, J., Friston, K.J.J., Kiebel, S.J.J., 2009. Variational Bayesian identification and prediction of stochastic nonlinear dynamic causal models. Physica D. 238, 2089–2118. doi:10.1016/j.physd.2009.08.002

David, O., Kiebel, S.J., Harrison, L.M., Mattout, J., Kilner, J.M., Friston, K.J., 2006. Dynamic causal modeling of evoked responses in EEG and MEG. Neuroimage 30, 1255–1272. doi:S1053-8119(05)00801-3 [pii] 10.1016/j.neuroimage.2005.10.045

Deco, G., Jirsa, V.K., Robinson, P. a, Breakspear, M., Friston, K., 2008. The dynamic brain: from spiking neurons to neural masses and cortical fields. PLoS Comput. Biol. 4, e1000092. doi:10.1371/journal.pcbi.1000092

Einevoll, G.T., 2014. LFPy : a tool for biophysical simulation of extracellular potentials generated by detailed model neurons 7, 1–15. doi:10.3389/fninf.2013.00041

Faugeras, O., 2006. Bifurcation Analysis of Jansen ' s Neural Mass Model 3068, 3052–3068.

Fisher, R.S., van Emde Boas, W., Blume, W., Elger, C., Genton, P., Lee, P., Engel, J., 2005. Epileptic seizures and epilepsy: definitions proposed by the International League Against Epilepsy (ILAE) and the International Bureau for Epilepsy (IBE). Epilepsia 46, 470–2. doi:10.1111/j.0013-9580.2005.66104.x

Frank, T.D., 2005. Nonlinear Fokker-Planck Equations, Springer Series in Synergetics. Springer-Verlag, Berlin/Heidelberg. doi:10.1007/b137680

Freestone, D.R., Karoly, P.J., Nešić, D., Aram, P., Cook, M.J., Grayden, D.B., 2014. Estimation of effective connectivity via data-driven neural modeling. Front. Neurosci. 8, 383. doi:10.3389/fnins.2014.00383

Friston, K., Mattout, J., Trujillo-Barreto, N., Ashburner, J., Penny, W., 2007. Variational free energy and the Laplace approximation. Neuroimage 34, 220–34. doi:10.1016/j.neuroimage.2006.08.035

Friston, K., Stephan, K., Li, B., Daunizeau, J., 2010. Generalised Filtering. Math. Probl. Eng. doi:10.1155/2010/621670

Friston, K.J., Bastos, a, Litvak, V., Stephan, K.E., Fries, P., Moran, R.J., 2012. DCM for complex-valued data: cross-spectra, coherence and phase-delays. Neuroimage 59, 439–55. doi:10.1016/j.neuroimage.2011.07.048

Friston, K.J., Kahan, J., Biswal, B., Razi, A., 2014. A DCM for resting state fMRI. Neuroimage 94, 396–407. doi:10.1016/j.neuroimage.2013.12.009

Friston, K.J., Trujillo-Barreto, N., Daunizeau, J., 2008. DEM: A variational treatment of dynamic systems. Neuroimage 41, 849–885. doi:10.1016/j.neuroimage.2008.02.054

Friston, K.J.J., Harrison, L., Penny, W., 2003. Dynamic causal modelling. Neuroimage 19, 1273–1302. doi:S1053811903002027 [pii]

Gerstner, W., 2000. Population dynamics of spiking neurons: fast transients, asynchronous states, and locking. Neural Comput 12, 43–89.

Gerstner, W., Naud, R., 2009. How Good Are Neuron Models? 329, 2008–2009.

Goodfellow, M., Schindler, K., Baier, G., 2011. Intermittent spike-wave dynamics in a heterogeneous, spatially extended neural mass model. Neuroimage 55, 920–32. doi:10.1016/j.neuroimage.2010.12.074

Govaerts, W., Sautois, B., 2006. Computation of the phase response curve: a direct numerical approach. Neural Comput. 18, 817–847. doi:10.1162/neco.2006.18.4.817

Grabska-Barwi??ska, A., Latham, P.E., 2014. How well do mean field theories of spiking quadratic-integrate-and-fire networks work in realistic parameter regimes? J. Comput. Neurosci. 36, 469–481. doi:10.1007/s10827-013-0481-5

Grimbert, F., Faugeras, O., 2006. Bifurcation analysis of Jansen's neural mass model. Neural Comput 18, 3052–3068. doi:10.1162/neco.2006.18.12.3052

Hájos, N., Pálhalmi, J., Mann, E.O., Németh, B., Paulsen, O., Freund, T.F., 2004. Spike timing of distinct types of GABAergic interneuron during hippocampal gamma

oscillations in vitro. J. Neurosci. 24, 9127–9137. doi:10.1523/JNEUROSCI.2113-04.2004

Harrison, L.M., David, O., Friston, K.J., 2005. Stochastic models of neuronal dynamics. Philos. Trans. R. Soc. Lond. B. Biol. Sci. 360, 1075–91. doi:10.1098/rstb.2005.1648

Havlicek, M., Friston, K.J., Jan, J., Brazdil, M., Calhoun, V.D., 2011. Dynamic modeling of neuronal responses in fMRI using cubature Kalman filtering. Neuroimage 56, 2109–2128. doi:10.1016/j.neuroimage.2011.03.005

Hochbruck, M., Ostermann, A., 2010. Exponential integrators, Acta Numerica. doi:10.1017/S0962492910000048

Holmes, M.D., Brown, M., Tucker, D.M., 2004. Are "generalized" seizures truly generalized? Evidence of localized mesial frontal and frontopolar discharges in absence. Epilepsia 45, 1568–79. doi:10.1111/j.0013-9580.2004.23204.x

Isabel, M., Garrido, F., 2008. Causal Modelling of Evoked Brain Responses by 1–164.

Jacobs, J., LeVan, P., Chander, R., Hall, J., Dubeau, F., Gotman, J., 2008. Interictal high-frequency oscillations (80-500 Hz) are an indicator of seizure onset areas independent of spikes in the human epileptic brain. Epilepsia 49, 1893–907. doi:10.1111/j.1528-1167.2008.01656.x

Jacobs, J., Levan, P., Chatillon, C.E., Olivier, A., Dubeau, F., Gotman, J., 2009. High frequency oscillations in intracranial EEGs mark epileptogenicity rather than lesion type. Brain 132, 1022–1037. doi:awn351 [pii]10.1093/brain/awn351

Jansen, B.H., Rit, V.G., 1995. Biological Cybernetics in a mathematical model of coupled cortical columns 366, 357–366.

Jansen, B.H., Rit, V.G., 1995. Electroencephalogram and visual evoked potential generation in a mathematical model of coupled cortical columns. Biol Cybern 73, 357–366.

Jefferys, J.G.R., Menendez de la Prida, L., Wendling, F., Bragin, A., Avoli, M., Timofeev, I., Lopes da Silva, F.H., 2012. Mechanisms of physiological and epileptic HFO generation. Prog. Neurobiol. 98, 250–64. doi:10.1016/j.pneurobio.2012.02.005

Jirsa, V.K., Stacey, W.C., Quilichini, P.P., Ivanov, A.I., Bernard, C., 2014. On the

nature of seizure dynamics. Brain 137, 2210–30. doi:10.1093/brain/awu133

Knight, B.W., 2000. Dynamics of encoding in neuron populations: some general mathematical features. Neural Comput. 12, 473–518.

Kovacic, G., Tao, L., Rangan, A. V, Cai, D., 2009. Fokker-Planck description of conductance-based integrate-and-fire neuronal networks. Phys Rev E Stat Nonlin Soft Matter Phys 80, 21904.

Lasztóczi, B., Klausberger, T., 2014. Layer-specific GABAergic control of distinct gamma oscillations in the CA1 hippocampus. Neuron 81, 1126–39. doi:10.1016/j.neuron.2014.01.021

Lemieux, L., Daunizeau, J., Walker, M.C., 2011. Concepts of connectivity and human epileptic activity. Front Syst Neurosci 5, 12. doi:10.3389/fnsys.2011.00012

Lomakina, E.I., Paliwal, S., Diaconescu, A.O., Brodersen, K.H., Aponte, E.A., Buhmann, J.M., Stephan, K.E., 2015. Inversion of hierarchical Bayesian models using Gaussian processes. Neuroimage 118, 133–45. doi:10.1016/j.neuroimage.2015.05.084

Lopes da Silva, F.H., Blanes, W., Kalitzin, S.N., Parra, J., Suffczynski, P., Velis, D.N., 2003. Dynamical diseases of brain systems: different routes to epileptic seizures. IEEE Trans. Biomed. Eng. 50, 540–8. doi:10.1109/TBME.2003.810703

López-Cuevas, A., Castillo-Toledo, B., Medina-Ceja, L., Ventura-Mejía, C., 2015. State and parameter estimation of a neural mass model from electrophysiological signals during the status epilepticus. Neuroimage 113, 374–386. doi:10.1016/j.neuroimage.2015.02.059

Marpeau, F., Barua, A., Josić, K., 2009. A finite volume method for stochastic integrate-and-fire models. J. Comput. Neurosci. 26, 445–57. doi:10.1007/s10827-008-0121-7

Mattia, M., Del Giudice, P., 2004. Finite-size dynamics of inhibitory and excitatory interacting spiking neurons. Phys. Rev. E 70, 52903. doi:10.1103/PhysRevE.70.052903

Mattia, M., Giudice, P. Del, 2002. Population dynamics of interacting spiking neurons. Phys Rev E Stat Nonlin Soft Matter Phys 66, 1–19. doi:10.1103/PhysRevE.66.051917

Molaee-Ardekani, B., Benquet, P., Bartolomei, F., Wendling, F., 2010. Computational modeling of high-frequency oscillations at the onset of neocortical partial seizures: from “altered structure” to “dysfunction”. Neuroimage 52, 1109–22. doi:10.1016/j.neuroimage.2009.12.049

Moler, C., Van Loan, C., 2003. Nineteen Dubious Ways to Compute the Exponential of a Matrix, Twenty-Five Years Later. SIAM Rev. 45, 3–49. doi:10.1137/S00361445024180

Moran, R.J., Kiebel, S.J., Stephan, K.E., Reilly, R.B., Daunizeau, J., Friston, K.J., 2007. A neural mass model of spectral responses in electrophysiology. Neuroimage 37, 706–20. doi:10.1016/j.neuroimage.2007.05.032

Moran, R.J., Stephan, K.E., Dolan, R.J., Friston, K.J., 2011. Consistent spectral predictors for dynamic causal models of steady-state responses. Neuroimage 55, 1694–708. doi:10.1016/j.neuroimage.2011.01.012

Moran, R.J., Stephan, K.E., Seidenbecher, T., Pape, H.-C.C., Dolan, R.J., Friston, K.J., 2009. Dynamic causal models of steady-state responses. Neuroimage 44, 796–811. doi:10.1016/j.neuroimage.2008.09.048

Nevado-Holgado, A.J., Mallet, N., Magill, P.J., Bogacz, R., 2014. Effective connectivity of the subthalamic nucleus-globus pallidus network during Parkinsonian oscillations. J. Physiol. 592, 1429–1455. doi:10.1113/jphysiol.2013.259721

Nevado-Holgado, A.J., Marten, F., Richardson, M.P., Terry, J.R., 2012. Characterising the dynamics of EEG waveforms as the path through parameter space of a neural mass model: application to epilepsy seizure evolution. Neuroimage 59, 2374–92. doi:10.1016/j.neuroimage.2011.08.111

Oren, I., Mann, E.O., Paulsen, O., Hájos, N., 2006. Synaptic currents in anatomically identified CA3 neurons during hippocampal gamma oscillations in vitro. J. Neurosci. 26, 9923–9934. doi:10.1523/JNEUROSCI.1580-06.2006

Papadopoulou, M., Leite, M., van Mierlo, P., Vonck, K., Lemieux, L., Friston, K., Marinazzo, D., 2015. Tracking slow modulations in synaptic gain using dynamic causal modelling: validation in epilepsy. Neuroimage 107, 117–26. doi:10.1016/j.neuroimage.2014.12.007

Park, S.-C., Lee, S.K., Che, H., Chung, C.K., 2012. Ictal high-gamma oscillation (60-99

Hz) in intracranial electroencephalography and postoperative seizure outcome in neocortical epilepsy. Clin. Neurophysiol. 123, 1100–10. doi:10.1016/j.clinph.2012.01.008

Penny, W.D., Litvak, V., Fuentemilla, L., Duzel, E., Friston, K., 2009. Dynamic Causal Models for phase coupling. J. Neurosci. Methods 183, 19–30. doi:10.1016/j.jneumeth.2009.06.029

Pillow, J.W., Paninski, L., Simoncelli, E.P., 2004. Maximum Likelihood Estimation of a Stochastic Integrate-and-Fire Neural Model * 16.

Pope, D.A., 1963. An exponential method of numerical integration of ordinary differential equations. Commun. ACM 6, 491–493. doi:10.1145/366707.367592

Risken, H., 1989. The Fokker-Planck Equation, Springer Series in Synergetics. Springer Berlin Heidelberg, Berlin, Heidelberg. doi:10.1007/978-3-642-61544-3

Rodrigues, S., Chizhov, A. V, Marten, F., Terry, J.R., 2010. Mappings between a macroscopic neural-mass model and a reduced conductance-based model. Biol. Cybern. 102, 361–71. doi:10.1007/s00422-010-0372-z

Sengupta, B., Friston, K.J., Penny, W.D., 2016. Gradient-based MCMC samplers for dynamic causal modelling. Neuroimage 125, 1107–18. doi:10.1016/j.neuroimage.2015.07.043

Sengupta, B., Friston, K.J., Penny, W.D., 2015. Gradient-free MCMC methods for dynamic causal modelling. Neuroimage 112, 375–81. doi:10.1016/j.neuroimage.2015.03.008

Shorvon, S., Guerrini, R., Cook, M., Lhatoo, S., 2012. Oxford Textbook of Epilepsy and Epileptic Seizures. Oxford University Press. doi:10.1093/med/9780199659043.001.0001

Spencer, S.S., 2002. Neural networks in human epilepsy: evidence of and implications for treatment. Epilepsia 43, 219–27.

Spiegler, A., Kiebel, S.J., Atay, F.M., Knosche, T.R., Knösche, T.R., 2010. Bifurcation analysis of neural mass models: Impact of extrinsic inputs and dendritic time constants. Neuroimage 52, 1041–58. doi:10.1016/j.neuroimage.2009.12.081

Sprott, J.C., 2007. A simple chaotic delay differential equation. Phys. Lett. Sect. A Gen. At. Solid State Phys. 366, 397–402. doi:10.1016/j.physleta.2007.01.083

Stefan, H., Lopes da Silva, F.H., 2013. Epileptic neuronal networks: methods of identification and clinical relevance. Front. Neurol. 4, 8. doi:10.3389/fneur.2013.00008

Stephan, K.E., Penny, W.D., Moran, R.J., den Ouden, H.E.M., Daunizeau, J., Friston, K.J., 2010. Ten simple rules for dynamic causal modeling. Neuroimage 49, 3099–109. doi:10.1016/j.neuroimage.2009.11.015

Suffczynski, P., Crone, N.E., Franaszczuk, P.J., 2014. Afferent inputs to cortical fast-spiking interneurons organize pyramidal cell network oscillations at high-gamma frequencies (60 – 200 Hz) 3001–3011. doi:10.1152/jn.00844.2013

Suffczynski, P., Lopes da Silva, F.H., Parra, J., Velis, D.N., Bouwman, B.M., van Rijn, C.M., van Hese, P., Boon, P., Khosravani, H., Derchansky, M., Carlen, P., Kalitzin, S., 2006. Dynamics of epileptic phenomena determined from statistics of ictal transitions. IEEE Trans. Biomed. Eng. 53, 524–32. doi:10.1109/TBME.2005.869800

Tiesinga, P.H.E., Fellous, J.M., José, J. V., Sejnowski, T.J., 2001. Computational model of carbachol-induced delta, theta, and gamma oscillations in the hippocampus. Hippocampus 11, 251–274. doi:10.1002/hipo.1041

Touboul, J., Wendling, F., Chauvel, P., Faugeras, O., 2011. Neural mass activity, bifurcations, and epilepsy. Neural Comput. 23, 3232–86. doi:10.1162/NECO_a_00206

Tripathy, S.J., Burton, S.D., Geramita, M., Gerkin, R.C., Urban, N.N., 2015. Brain-wide analysis of electrophysiological diversity yields novel categorization of mammalian neuron types. J. Neurophysiol. 113, jn.00237.2015. doi:10.1152/jn.00237.2015

Ullah, G., Schiff, S.J., 2010. Assimilating seizure dynamics. PLoS Comput. Biol. 6, e1000776. doi:10.1371/journal.pcbi.1000776

Wang, Y., Goodfellow, M., Taylor, P.N., Baier, G., 2012. Phase space approach for modeling of epileptic dynamics. Phys. Rev. E 85, 61918. doi:10.1103/PhysRevE.85.061918

Wendling, F., Bartolomei, F., Mina, F., Huneau, C., Benquet, P., 2012. Interictal spikes, fast ripples and seizures in partial epilepsies--combining multi-level computational models with experimental data. Eur. J. Neurosci. 36, 2164–77. doi:10.1111/j.1460-

9568.2012.08039.x

Wendling, F., Hernandez, A., Bellanger, J.-J., Chauvel, P., Bartolomei, F., 2005. Interictal to ictal transition in human temporal lobe epilepsy: insights from a computational model of intracerebral EEG. J. Clin. Neurophysiol. 22, 343–56.

WHO, n.d. WHO website [WWW Document]. URL http://www.who.int/mediacentre/factsheets/fs999/en/

Wilson, H.R., Cowan, J.D., 1972. Excitatory and inhibitory interactions in localized populations of model neurons. Biophys. J. 12, 1–24. doi:10.1016/S0006-3495(72)86068-5

8 APPENDICES

APPENDIX A

A nonlinear system of coupled ordinary differential equations with N delayed dependencies, τ_i, may be written in the form:

$$\dot{\boldsymbol{X}}(\boldsymbol{t}) = \boldsymbol{f}(\boldsymbol{X}(\boldsymbol{t}-\boldsymbol{\tau_0}), \boldsymbol{X}(\boldsymbol{t}-\boldsymbol{\tau_1}), \dots, \boldsymbol{X}(\boldsymbol{t}-\boldsymbol{\tau_N}))$$

Near a stationary point, X_0, if f is of class C^1, such a system may be linearised to:

$$\Delta\dot{\boldsymbol{X}}(\boldsymbol{t}) = \sum_{\boldsymbol{i=0}}^{\boldsymbol{N}} \boldsymbol{J_i} \cdot \Delta\boldsymbol{X}(\boldsymbol{t}-\boldsymbol{\tau_i}) + \boldsymbol{O}(\Delta\boldsymbol{X^2}) \qquad \textbf{(A1)}$$

With:

$\Delta X(t) = X(t) - X^0$, and

$$J_i = \left.\frac{\partial f(X(t-\tau_0), X(t-\tau_1), \dots, X(t-\tau_N))}{\partial\, X(t-\tau_i)}\right|_{X_0}$$

Taking the Laplace transform of (A1) and adding small perturbations ΔU to the system:

$$s \cdot \Delta X(s) = \sum_{i=0}^{N} e^{-s\cdot\tau_i} \cdot J_i \cdot \Delta X(s) + \Delta U(s)$$

Rearranging to isolate $\Delta X(s)$:

$$\Delta X(s) = \left(s \cdot I - \sum_{i=0}^{N} e^{-s\cdot\tau_i} \cdot J_i\right)^{-1} \cdot \Delta U(s)$$

If the imaginary axis falls within the region of convergence of the Laplace transform (i.e. the system is stable), and if we complement the system with a linear (or locally linearised) observation function $\Delta Y(t) = B \cdot \Delta X(t)$, its spectral response is given by:

$$\Delta Y(j\omega) = B \cdot \left(j\omega \cdot I - \sum_{i=0}^{N} e^{-j\omega\cdot\tau_i} \cdot J_i\right)^{-1} \cdot \Delta U(j\omega)$$

APPENDIX B

In this appendix we display the results from the **Figure 2.2** and

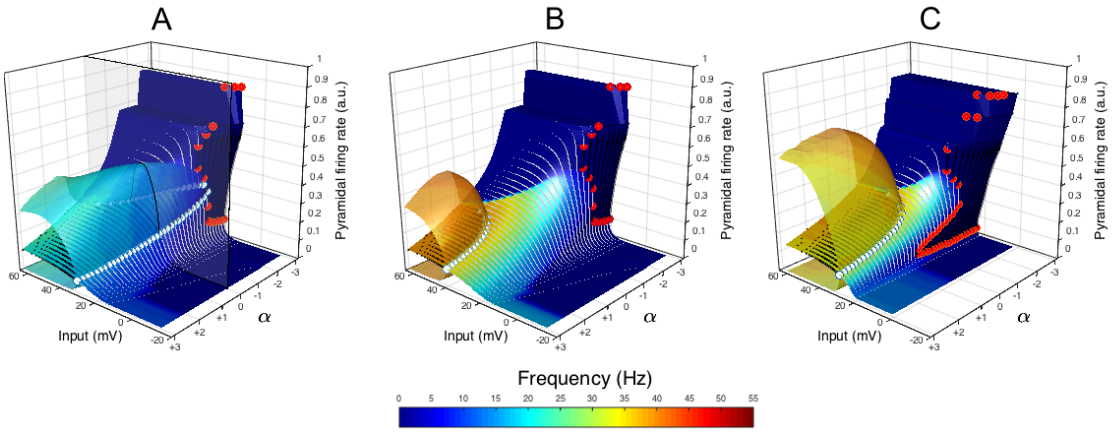

Figure 2.3, panels C, but with extended ranges with regards to the exploration of connection strengths. The exponential parameter α was explored from -15 to +15, while within numerically stable solutions.

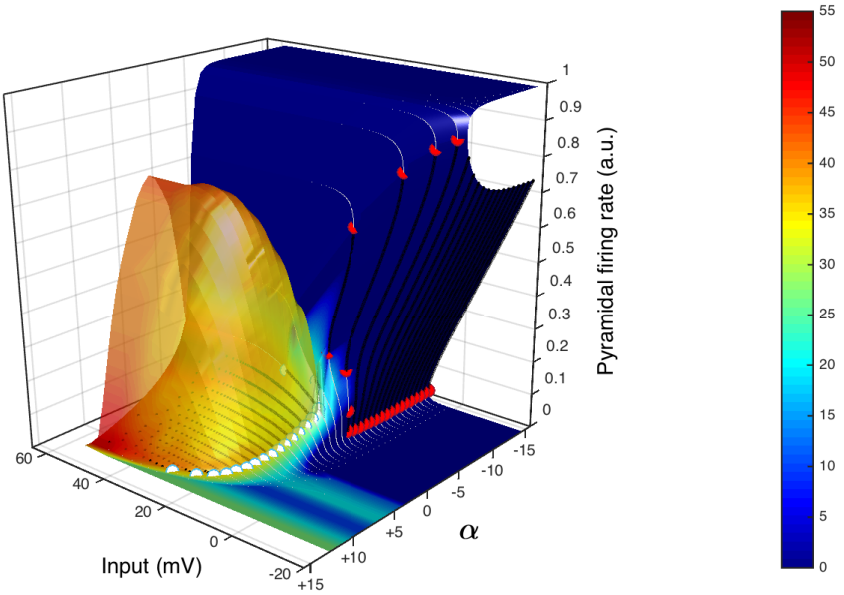

Figure 8.1 - Bifurcation diagram for the conductance based NMM, as in **Figure 2.2**, (C) Fast synaptic constants + high sigmoid activation function slope, but with extended ranges for the parameter α. The solid surfaces indicate pyramidal firing rates at the fixed points, and transparent surfaces indicate maxima and minima of limit cycles. Black dotted lines indicate unstable fixed points and grey dots indicate stable ones. White circles indicate the occurrence of Hopf bifurcations, and red circles indicate limit-point bifurcations. The surfaces are colour-coded for the peak frequency of the spectral response of the system.

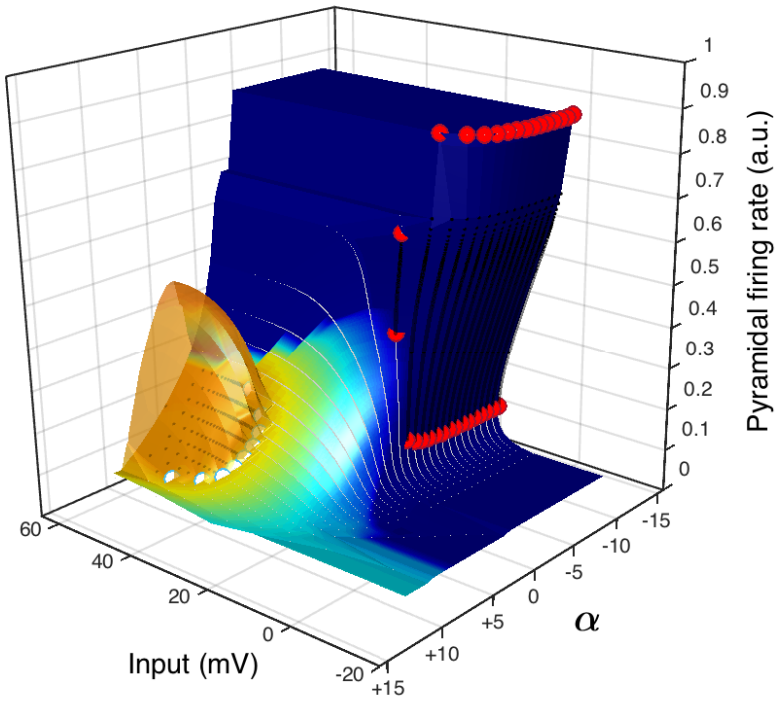

Figure 8.2 - Bifurcation diagram for the kernel based NMM, as in

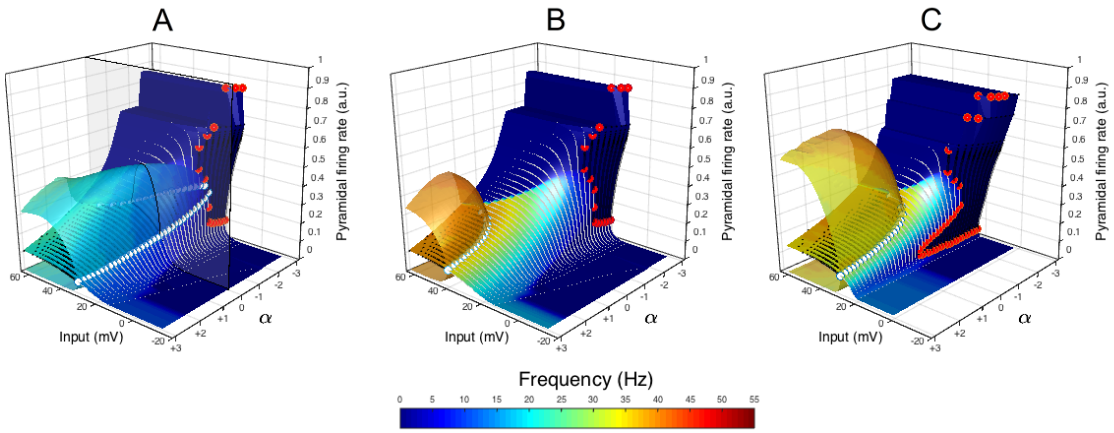

Figure 2.3, (C) Fast synaptic constants + high sigmoid activation function slope, but with extended ranges for the parameter α. The solid surfaces indicate pyramidal firing rates at the fixed points, and transparent surfaces indicate maxima and minima of limit cycles. Black dotted lines indicate unstable fixed points and grey dots indicate stable ones. White circles indicate the occurrence of Hopf bifurcations, and red circles indicate limit-point bifurcations. The surfaces are colour-coded for the peak frequency of the spectral response of the system.